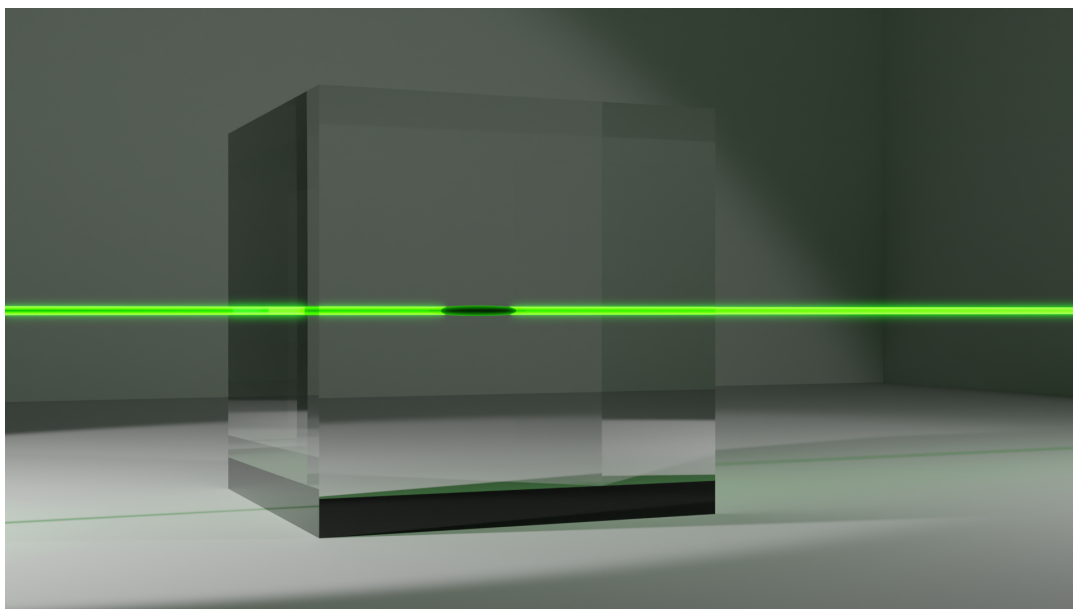UNIVERSITÄT
PADERBORN

Optical and Electrochemical Properties of KTP-Type Crystals

Eine der Naturwissenschaftlichen Fakultät
der Universität Paderborn vorgelegte

DISSERTATION

zur Erlangung des akademischen Grades

DOCTOR RERUM NATURALIUM (DR. RER. NAT.)

von

ADRIANA BOCCHINI

Tag der Abgabe: 17. Mai 2023
Tag der Disputation: 12. Juli 2023

Promotionskommision

Vorsitzende: PROF. DR. CHRISTINE SILBERHORN
Integrated Quantum Optics
Department Physik − Universität Paderborn

Erstgutachter: PROF. DR. WOLF GERO SCHMIDT
Theoretical Material Physics
Department Physik − Universität Paderborn

Zweigutachter: PROF. DR. SIMONE SANNA
Solid State Spectroscopy
Institut für Theoretische Physik − Justus-Liebig-Universität Gießen

Vertreter des Mittelbaus: DR. MATTHIAS REICHELT
Computational Optoelectronics and Photonics
Department Physik − Universität Paderborn

Erklärung

Hiermit erkläre ich, Adriana Bocchini geboren am 03.09.1995 in Warburg, dass ich die vorliegende Dissertation ohne fremde Hilfe und ohne Benutzung anderer als der angegebenen Quellen angefertigt habe und, dass diese in gleicher oder ähnlicher Form noch keiner anderen Prüfungsbehörde vorgelegt habe. Alle Ausführungen, die wörtlich oder sinngemäß übernommen worden sind, sind als solche gekennzeichnet.

_____
Ort, Datum

_____
Unterschrift

Abstract

POTASSIUM titanyl phosphate (KTP) and related materials are largely applied in (nonlinear) optics and could also advance in electrochemical applications, e. g., as electrodes for alkali-ion batteries. Unfortunately, its characteristic photochromic damage, so-called gray tracks, strongly limits the application of KTP in optical devices, but may also affect its electrochemical performance. However, it is still unclear, which microscopic mechanisms really cause gray tracks to form, and why they do not affect the whole KTP-type family to the same extent.

In this thesis, we will use density functional theory (DFT) to investigate (i) the suitability of potassium titanyl arsenate (KTA) for potassium-ion batteries, (ii) the absorption signatures of oxygen vacancies, causing those Ti^{3+} centers to form, which are commonly discussed to facilitate gray track formation, and (iii) the influence of different chemical environments on the properties of these Ti^{3+} centers.

KTA electrodes are expected to give rise to high average working voltages and to be characterized by modest volume deformations as well as low activation energies, being thus a promising cathode and anode material.

Modified hybrid functionals are used for the computation of optical absorption spectra. We find the vacancies absorption to be similar to the one of gray tracks and strongly dependent on the light polarization as well as their charge state.

Finally, our data suggest that the current gray-tracking model, especially regarding the position of the Ti^{3+} center relative to the oxygen vacancy, must be revised. Moreover, gray tracks could be the result of a two-step process involving both the formation of an oxygen vacancy and a displacement of potassium ions in the cell.

Zusammenfassung

K ALIUMTITANYLPHOSPHAT (KTP) und verwandte Kristalle sind in der (nichtlinearen) Optik weit verbreitet und scheinen auch in der Elektrochemie, z.B. in Alkali-Ionen-Batterien, vielversprechend zu sein. Der Einsatz von KTP in optischen Anwendungen ist jedoch durch die Ausbildung sog. *Gray Tracks* eingeschränkt, die zudem auch die elektrochemische Performance beeinträchtigen könnten. Es ist bisher unklar, welche genauen mikroskopischen Mechanismen zur Ausbildung von *Gray Tracks* führen und warum die gesamte KTP-Familie nicht im gleichen Maße betroffen ist.

In dieser Arbeit untersuchen wir mittels Dichtefunktionaltheorie (DFT) (i) die Eignung von Kaliumtitanylarsenat (KTA) für Kalium-Ionen-Batterien, (ii) die Absorptionsspektren von Sauerstoffvakanzen, welche jene Ti^{3+}-Zentren induzieren, die im Verdacht stehen, die Bildung der *Gray Tracks* zu begünstigen, und (iii) den Einfluss verschiedener chemischer Umgebungen auf die Eigenschaften dieser Ti^{3+}-Zentren.

Es zeigt sich, dass KTA-Elektroden potenziell hohe mittlere Arbeitsspannungen, geringe Volumenänderungen und niedrige Aktivierungsenergien aufweisen und als Kathode sowie als Anode geeignet sein könnten.

Mittels modifizierter Hybridfunktionale berechnete Absorptionsspektren zeigen, dass die Absorption von Sauerstoffvakanzen jener der *Gray Tracks* ähnelt und zudem von der Lichtpolarisation und deren Ladungszustand abhängig ist.

Es ergibt sich zudem, dass das aktuelle *Gray-Track*-Modell zu revidieren ist, besonders was die Position der Ti^{3+}-Zentren relativ zur Vakanz angeht. Zudem könnten *Gray Tracks* das Ergebnis eines zweistufigen Prozesses sein, der sowohl die Bildung einer Sauerstoffvakanz als auch die Verschiebung von Kaliumionen umfasst.

Contents

1

Introduction: Perfect Imperfections

THE presence of defects in a crystal is commonly considered a limiting factor and there is a rigorous quest for strategies to reduce them. In fact, they can lead to a series of undesirable effects for applications: From a reduced efficiency of solar cells[1–3], to leakage currents[4,5], to promoting the failure of lasers[6,7]. Surprisingly, already modest defect concentrations (common concentrations are 100 or less ppm) can have a strong impact on the material.[8]

But, on the other hand, the effects arising from modifications to the crystal lattice can also be exploited for applications or to customize the characteristics of a material, e. g., its dielectric or conduction properties. In this case, however, one would refer to these impurities as doping rather than defects. For example, doped crystals are commonly applied in electronics[9], but can also be utilized for the construction of (tunable) solid-state lasers[10], to induce superconductivity[11], for the realization of waveguides[12], or to realize room-temperature qubits for quantum computing[13]. Another field, in which the intentional creation of vacancies and interstitials plays a major role is electrochemistry, for example within lithium-ion batteries. In fact, the charge transfer from one electrode to the other is accompanied by the (de)intercalation of ions[14,15].

In both cases, it is therefore indispensable to gain a thorough understanding about the formation mechanisms and the influence of impurities (dopants) on the host material. Applying this knowledge, crystals of superior quality and with tailored properties for applications can be grown.

In this context, an interesting material to illustrate the impairing and enhancing effects of defects is potassium titanyl phosphate ($KTiOPO_4$, KTP). First synthesized in 1890[16], KTP features an exceptional combination of properties, which enables its application in plenty of devices: The crystal is already well-established in the optical field[17–27] and the crystal (together with other isomorphs) has recently also turned out to be a promising material for electrochemical applications, especially in the context of alkali-ion batteries, e. g., sodium (Na), potassium (K), or rubidium (Rb), as substitutes for technologies based on lithium (Li)[28–40].

Unfortunately, KTP crystals suffer from characteristic photochromic damage, the so-called gray tracking, which negatively affects the crystals' properties.[41–54] Different processes, for example high-intensity laser light[41–44], electric fields[45–47] or X rays[48], can lead to their formation. Gray tracks are characterized by a dark coloration and are thus an evident drawback for optical devices, e. g., because they show a high absorption of the fundamental and second-harmonic radiation in second-harmonic generation (SHG) applications[42–44, 46].

The formation of gray tracks is discussed to be related to the reduction of Ti atoms (i. e., the formation of Ti^{3+} centers) as a result of the charge-compensation process of potassium (K) vacancies by a variety of point defects.[44, 47, 49–54] Among these, centers attributed to oxygen vacancies are unique in being thermally stable[54].

In order to enhance the resistivity of KTP against the formation of gray tracks, treatments leading to an overall improved stoichiometry with respect to the K content[55] or a small rubidium (Rb) doping[56] were found to be beneficial. The effects of both approaches are similar: The former directly reduces the overall K-vacancy concentration. The latter reduces the ionic conductivity in the crystal and, therefore, the formation of K vacancies. As a consequence, the formation of charge-compensating O vacancies and related Ti^{3+} centers is hindered.

However, the mechanisms leading to the formation of gray tracks could involve more complicated processes. In fact, K ions themselves have also been discussed in the context of gray tracking: Mürk *et al.*[48] indicated Ti^{3+} centers caused by K interstitials to be responsible for the gray track formation. Moreover, Mu and Ding[57] resolved an "invisible damage" and attributed its cause to the drift of K ions in the cell.

The high ionic conductivity, caused by the peculiar channel structure in KTP, on the other hand, is really advantageous in the context of electrochemistry. In fact, to guarantee an efficient (de)charging of a battery, ions should be allowed to freely migrate through the electrodes. Nevertheless, since gray tracks are related to trapped charge carriers, this phenomenon might also impair the electrochemical performance of KTP crystals.

This motivates the present study conducted in the framework of density functional theory (DFT), in which we aim at:

Investigating the suitability of potassium titanyl arsenate ($KTiOAsO_4$, KTA) for electrochemical applications: More precisely, we will test the suitability of KTA crystals (less affected by gray tracks[58]) for electrodes in K-ion batteries. Both the cathode and the anode material will be simulated. Thereby, we will concentrate on the calculation of average voltages arising from the (de)intercalation of K atom in the crystal, volume deformations, and ion (vacancy) diffusion mechanisms;

Calculating the absorption properties of charged O vacancies in KTP: Since O vacancies (and related Ti^{3+} centers) seem to be directly connected to the gray-track phenomenon, it is important to characterize their absorption properties to better understand their role in gray tracking. Therefore, modified hybrid functionals are used to achieve (i) a reliable description of defect-related mid-gap levels and (ii) realistic absorption properties. This enables a quantitative comparison of the absorption signatures of these vacancies with those of gray tracks;

Investigating the influence of the chemical environment on the O-vacancy-related Ti^{3+} centers: Since real KTP crystals can show rather high K-vacancy concentrations[59] and a Rb

doping[56] is beneficial to prevent the formation of gray tracks, it is important to investigate, how the properties of Ti^{3+} centers are influenced by these chemical environments relevant for applications. New strategies to increase the resistance of KTP against gray tracking could be developed on the footing of this investigation.

Structure of the thesis: The thesis is structured as follows. First, we will introduce the KTP-type family and give a general introduction to density functional theory in Chap. 2 and Chap. 3, respectively.

Then, we will concentrate on the theoretical investigation of electrochemical properties. Therefore, in Chap. 4, we will illustrate, how the electrochemical properties of a material can be determined in the framework of DFT. Then, in Chap. 5, the discussed methodologies will be applied to test the performance of KTA electrodes.

After this, we will focus on gray tracking in KTP. To this end, in Chap. 6, we will elaborate on the computation of optical properties on different levels of theory. The optical properties of charged oxygen vacancies will then be discussed in Chap. 7. Consequently, in Chap. 8, the systematic investigation of different defect combinations will lead us to reconsider the current gray-tracking model and formulate a revised hypothesis on the gray track formation.

Finally, concluding remarks will be provided in Chap. 9.

2

Potassium Titanyl Phosphate: An All-In-One Device

Iɴ this thesis, we will investigate a variety of properties of two constituents of the potassium titanyl phosphate ($KTiOPO_4$, KTP) crystal family. More precisely, we will compute the electrochemical properties of potassium titanyl arsenate ($KTiOAsO_4$, KTA) for potassium-ion batteries. In addition, we will discuss the impact of charged oxygen vacancies (and related Ti^{3+} centers) on the optical absorption properties of KTP. Moreover, we will investigate the influence of different chemical environments on the properties of these oxygen-vacancy-related Ti^{3+} centers.

In this chapter, the KTP-type crystal family shall be introduced. First, in Sec. 2.1, we will characterize the crystallographic properties of KTP-type crystals and common non-stoichiometries of KTP, which are relevant for this work. Then, in Sec. 2.2, an insight into its different application fields shall be given. Finally, in Sec. 2.3 the impairing phenomenon of gray tracking will be discussed.

2.1 Crystallographic Properties

The name of the KTP-type family derives from its most prominent member: Potassium titanyl phosphate ($KTiOPO_4$). Crystals belonging to this family are isomorphic, which means they are all characterized by the same crystal structure. Thus, we can concentrate on the properties of KTP and eventually point out, how they differ from other members of interest, i. e., potassium titanyl arsenate ($KTiOAsO_4$, KTA) and rubidium titanyl phosphate ($RbTiOPO_4$, RTP).

To the best of our knowledge, the first documented synthesis of KTP was performed in 1890[16], while the first comprehensive investigations of the crystallographic properties of this family were carried out in the first half the 1970s by R. Masse and J. G. Grenier[60] and later by Tordjman *et al.*[61]. It was found that, at room temperature, KTP assumes an orthorhombic crystal lattice with the ferroelectric[1] (non-centrosymmetric) space group *Pna*2$_1$. For temperatures

---

[1]The ferroelectricity of a material is characterized by a spontaneous electric polarization, which is caused by a polar axis. In KTP this is represented by the *c* axis.

above the Curie temperature[2] a transition to the paraelectric (centrosymmetric) space group *Pnan* occurs. Thereby, the point groups *mm*2 and *mmm* are assumed, respectively.[55, 60, 61, 63]

The general constitution formula of the KTP-type family reads

$$M\text{TiO}X\text{O}_4, \tag{2.1}$$
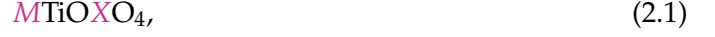
where *M* denotes, e. g., potassium (K), rubidium (Rb), sodium (Na), thallium (Tl), caesium (Cs), or ammonium (NH_4), and *X* either phosphorus (P) or arsenic (As).[17] In addition, also crystals with vanadium (V) occupying the Ti sites and fluorine (F) occupying special oxygen sites[3] have recently been synthesized.[28–40] These, however, are most relevant for electrochemical rather than optical applications.

Table 2.1: Experimentally determined lattice parameters of KTP, KTA and RTP.

	KTP[61]	KTA[64]	RTP[65]
a [Å]	12.814	13.130	12.952
b [Å]	6.404	6.581	6.493
c [Å]	10.616	10.781	10.555

The different occupation of analogous lattice sites influences to different degrees the lattice constants of the various KTP-type crystals. Notably, the group-V elements (occupying the *X* sites) have a larger impact on the dimensions of the unit cell than the alkali ions (located on the *M* sites).[55] This can be clearly seen by comparing the experimentally determined lattices constants of KTP, KTA and RTP compiled in Tab. 2.1: While the lattice constants of KTP and RTP are very close, the difference between those of KTP and KTA are more pronounced.

The KTP-type unit cell is composed of 64 atoms. These, however, can be reduced to a system of two nonequivalent $M\text{TiO}X\text{O}_4$ macromolecules (i. e., 16 nonequivalent lattice sites), which are connected by the four symmetry operations of the space group $Pna2_1$.[61] A schematic illustration[4] of the unit cell of an exemplary member of the $M\text{TiO}X\text{O}_4$ crystal family is depicted in Fig. 2.1.

The crystal structure can be described as a superposition of two different frameworks: The first corresponds to a system of distorted TiO_6 octahedra and $X\text{O}_4$ tetrahedra liked into chains, the second to a positively charged sub-lattice composed of M^+ ions, see Fig. 2.1. More precisely, along the [011] and the [0$\bar{1}$1] crystal directions, helical TiO_6 chains can be identified. Along the [100] and the [010] directions, on the other hand, alternated chains of TiO_6 and $X\text{O}_4$ cross the crystal. All the polyhedra are linked via mutual O atoms.[61] Therefore, the O atoms can be further subdivided into two groups according to their coordination. The first group corresponds to the oxygen sites O(1)-O(8), which are coordinated to one *X* and one Ti atom. The second group[5] includes the sites O(9) and O(10), which are coordinated to Ti exclusively. In the following we will refer to these two oxygen types as $\text{O}_{\text{Ti}-X}$ and $\text{O}_{\text{Ti}-\text{Ti}}$, respectively.

---

[2]The Curie temperature (T_C) of KTP is not clearly defined and assumes values between 883 and 960 °C. The Curie temperature, in fact, assumes different values based on the K concentration: A more pronounced K deficiency leads to lower values for T_C.[62]

[3]More precisely, only the O atoms coordinated to two Ti (or V) atoms can be replaced with F.

[4]All the crystal geometries as well as wave functions, and charge densities depicted in this thesis are visualized using the open-access program Visualization for Electronic and STructural Analysis (VESTA)[66].

[5]As mentioned before, the atoms at the sites O(9) and O(10) can be substituted with F atoms.
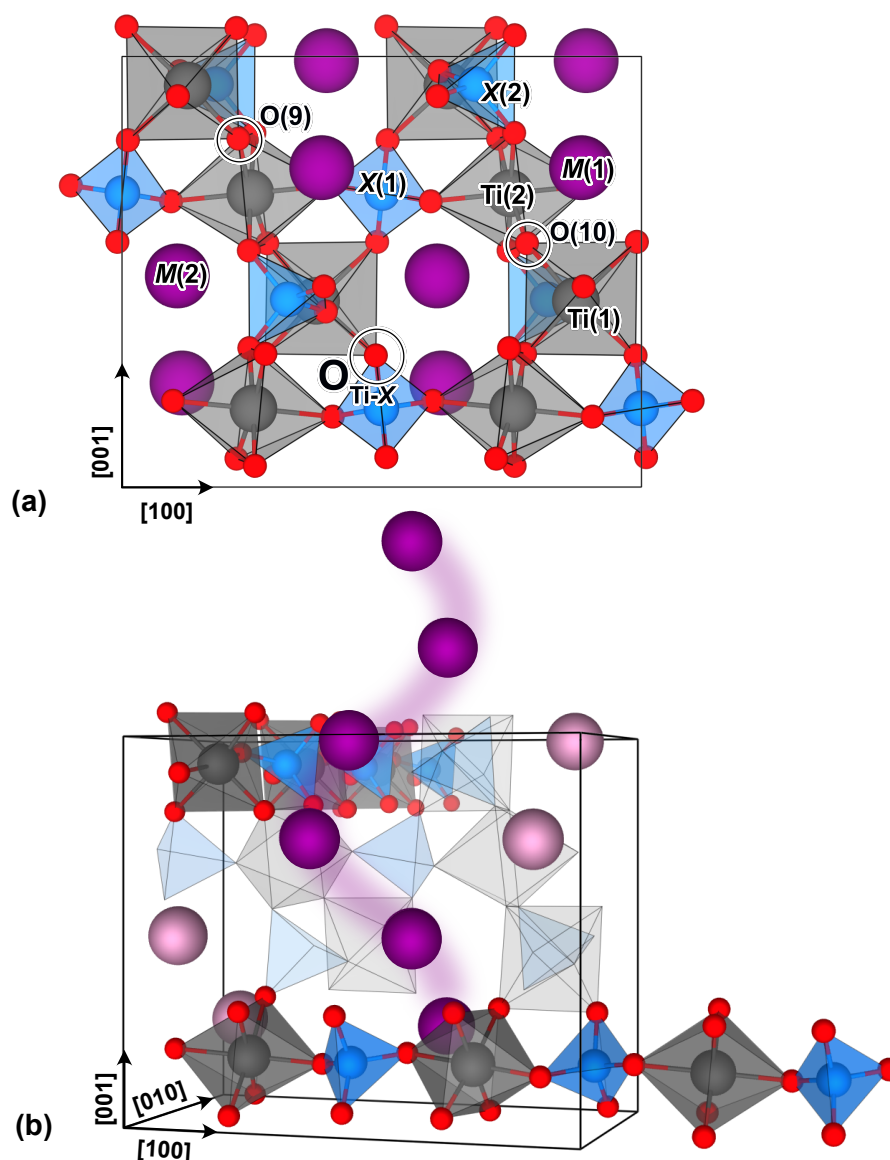
Figure 2.1: (a) View along the [010] direction of an exemplary KTP-type crystal. The position of nonequivalent Ti, X and M lattice sites as well as one O_{Ti-X} and both O_{Ti-Ti} atoms (O(9), O(10)) is indicated.
(b) Schematic representation of the TiO_6-XO_4 chains along the directions [100] and [010], as well as the M-ion migration channels along the [001] direction.

Every TiO_6 octahedron features two O_{Ti-Ti} atoms. The two Ti sites present in the lattice differ with respect the angle these O atoms form with the central Ti atom: about $90°$ in the case of Ti(1), about $180°$ in the case of Ti(2). The $X(1)$ site is assumed by X atoms within chains parallel to the [100] direction, the $X(2)$ site by those in chains parallel to [010].[61]

The M atoms form a charged sub-lattice with $M(1)$ and $M(2)$ coordinated to eight and nine O atoms, respectively. Thereby, the cage attributable to the site $M(2)$ is by about $25\,\%$ larger than that of $M(1)$[67].

The mobility of M(1) along [100] is hindered by the polyhedra chains along [010]. Despite the presence of large channels along [010], no significant diffusion along this direction can be

measured. The $M(2)$ ions, on the other hand, can diffuse almost freely along [001] via vacancy hopping mechanisms.[24,55,68,69]

Regarding their synthesis, KTP crystals are exclusively grown from solutions since the material decomposes thermally before melting. Thereby, the most common methods are hydrothermal processes and the growth from self-fluxes. The former method usually leads to crystals of higher quality, while the latter can be applied for the fabrication of larger crystals.[55]. One commonly applied solvent for the synthesis of KTP is the so-called K6 (i. e., $K_6P_4O_{13}$) following, for example, the reaction[70,71]

$$3KH_2PO_4 + 2K_2HPO_4 + TiO_2 \longrightarrow KTiOPO_4 + K_6P_4O_13 + 4H_2O \qquad (2.2)$$

Compared to hydrothermally grown crystals, flux-grown KTP shows poorer stoichiometries especially regarding the K content. Comparatively high K-vacancy concentrations up to 500-800 part per million atomic (ppma) have already been measured.[59]

In Sec. 2.1.1, we will discuss common non-stoichiometries of KTP, focusing on those relevant for this work.

2.1.1 Non-Stoichiometric KTP

Due to the large number of lattice sites in the cell, a plethora of point defects, both intrinsic and extrinsic in nature, are possible. These include, for example, vacancies, substitutional atoms or interstitials. More precisely, vacancies correspond to unoccupied lattice sites $A(i)$, substitutional atoms are sites of an element A occupied by an element B, and interstitials are atoms, which do not occupy any lattice site. In addition, different point defects might group into a defect complex. In the following, these will be denoted as V_A^q, B_A^q, and A_i^q, respectively, with q indicating the charge state of the defect itself.

Among all the possible defects, the most relevant for this thesis are K and O vacancies (i. e., V_K and V_O), Rb substitutionals for K (i. e., Rb_K), as well as K interstitials (i. e., K_i), see Fig. 2.2. In addition, we note that also a variety of extrinsic point defects (e. g., silicon (Si), iron (Fe), or antimony (Sb) impurities) have also been observed[59].

As already mentioned, KTP crystals are always deficient in K and rather high K-vacancy concentrations (up to $800\,ppm$[59]) are possible. Normally, K vacancies are found in the charge state -1[72]. The creation of one neutral K atom from the KTP lattice, in fact, would induce a hole at the valence band maximum (VBM). Since this is rather unstable, at least in the thermodynamic equilibrium, K vacancies are energetically more stable in the charge state -1.

K vacancy are spontaneously charge compensated by, e. g., oxygen vacancies at the sites O_{Ti-Ti}[49,52,54] or bivalent cations (for example Pb^{2+}) substituting for K^+[73], by trapped holes stabilized at the O_{Ti-Ti} sites[74].

The peculiar TiO_6-PO_4 chain network in KTP give rise to large channels along the crystallographic axes a and b. Notably, the diffusion along the [100] and the [010] directions is rather unfavorable. Nevertheless, the K^+ ions can diffuse relatively freely along the [001] direction via vacancy hopping mechanisms.[24,55,68,69] At low temperatures and in the absence of any external voltage, the K-ion migration in KTP is relatively modest and inhomogeneities formed during the crystal growth are not spontaneously equilibrated. Thus, large KTP crystals can show an inhomogeneous V_K distribution along the growth direction: As the crystal grows, an enrichment of K cations in the solution can be measured, i. e., the K to P ratio increases. As a
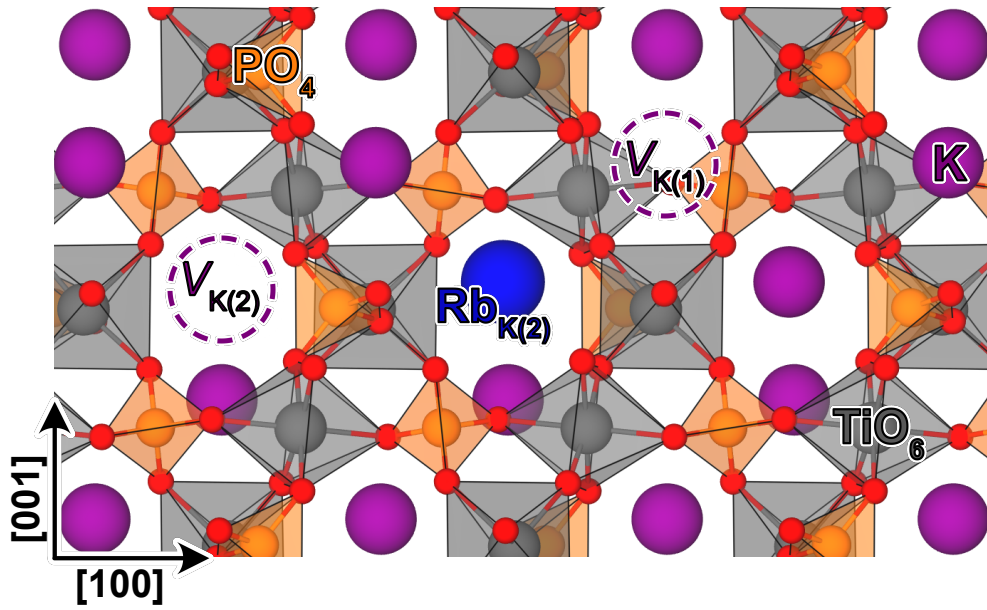
Figure 2.2: Schematic representation of non-stoichiometries in KTP crystals relevant for this work, i. e., two nonequivalent K vacancies ($V_{K(1)}$ and $V_{K(2)}$) and a Rb substitutional atom at the site K(2) ($Rb_{K(2)}$).

consequence, also the K content in the crystal changes, becoming more and more stoichiometric.[62]

This situation has an immediate consequence also on the properties of the crystal itself, for example the Curie temperature[62] or the refractive index[75], which are influenced by the K content.

On the other hand, the related O-vacancy diffusion is relatively high and causes an internal electric field[72].

A rapid ion (de)intercalation might be very beneficial for electrochemical applications, making these crystals perfect candidates for alkali-ion based electrodes[28–40]. However, this property is a serious drawback during operations requiring the application of slowly varying electric fields, e. g., periodic poling[27].

Some strategies to reduce the ion migration along the crystal are, e. g., the reduction of the temperature during poling[76] or a potassium-nitrate treatment[45]. The latter thereby enhances the crystal stoichiometry and reduces the hopping probability. Another approach is a small Rb doping (less than 1%)[56], i. e., $Rb_xK_{1-x}TiOPO_4$ (RKTP). Compared to K, Rb features a larger ionic radius and is thus more likely to occupy the larger lattice site K(2)[77], see Fig. 2.2. In addition, its migration through the crystal is less favorable, effectively blocking the channels relevant for the K-ion migration[45].

A further effect of the Rb (or Cs) doping is an increase of the refractive index of the material, which enables the modeling of waveguides.[26,78]

The reduction of the ionic conductivity was also found to enhance the resistivity of KTP against gray tracking (see for example Ref. 45). A more detailed description of this phenomenon can be found in Sec. 2.3.

2.2 Well-Established in Optics, Promising in Electrochemistry

The spatial orientation of atoms whithin the KTP-type structure is crucial for the favorable combination of dielectric, electro-optic, nonlinear optical, and electro-chemical properties. In the following, we will shortly outline the properties of KTP and introduce some of its application fields.

In the second half of the 1970s, Zumsteg and co-workers published the first investigation on the optical properties of KTP, discovering its exceptional nonlinear properties[79]. From then on, the crystals' quality and, consequently, their properties have been improved and new isomorphs have been synthesized. Nowadays, KTP crystals are most established in many (non-linear) optical devices: They are commonly utilized as frequency doublers in Nd:YAG lasers, converting near-infrared light ($\lambda = 1064\,\mathrm{nm}$, $E_{\mathrm{ph}} = 1.17\,\mathrm{eV}$) into green light ($\lambda = 532\,\mathrm{nm}$, $E_{\mathrm{ph}} = 2.33\,\mathrm{eV}$)[22]. In addition, they are also suitable to be applied in optical parametric oscillators (OPOs)[23], or as an electro-optic amplitude modulator[24,25]. Additionally, upon a Rb- or Cs-doping, they can be used to construct waveguide structures.[26,27]

The suitability for nonlinear optical applications is not only given by its high nonlinear coefficient, caused by the $KO_{8,9}$ units[80] together with the distorted TiO_6 octahedra[79], but also by its transmission properties. In fact, with an optical band gap of $E_{\mathrm{gap}} = 3.2 - 3.8\,\mathrm{eV}$[81–84], KTP shows a broad transparency band covering the whole visible and near-infrared spectrum, more precisely the wavelength range 350-4500 nm[79] (i. e., 0.28-3.54 eV). Moreover, it does also feature a great thermal stability as well as a high threshold against optical damage.[85]

Finally, the internal polarization of KTP crystals is advantageous to further enhance the efficiency of the frequency conversion: To take benefit from so-called quasi-phase matching[6], the nonlinear coefficient has to be modulated along the propagation direction of the laser beam. For this, the orientation of the internal polarization has to be periodically reversed with a period corresponding to the so-called coherence length. This is achieved by periodic poling, i. e., the application of an external field antiparallel to the spontaneous polarization.[78] The reversion of the polarization is thereby caused by (i) a repositioning of the alkali ions in the material along the direction of the external field[86], and (ii) by a change in the bond lengths within the TiO_6 octahedra, more precisely, by interchanging the lengths of long and short Ti-O bonds[87].

Unfortunately, the intrinsic ionic conductivity of KTP hampers the poling process, since it renders the monitoring of the process and thus the reproducibility difficult.[27,45,78] For this reason, many strategies have been developed to reduce the ionic current within the crystals, e. g., via Rb doping[56] or potassium-nitrate treatment[45].

Nevertheless, what is a drawback in optical devices can be advantageous for electrochemical applications, more precisely for the modeling of new electrode materials. In fact, a fast ion (de)intercalation is indispensable to guarantee an efficient fast charging of batteries[7]. The suitability of KTP-type crystals as anode and cathode materials for alkali-ion batteries has recently been shown by numerous experimental and theoretical studies.[28–40]

The application as an electrode requires the intentional creation of point defects: During

---

[6]Quasi-phase matching is a technique which is applied to prevent the dephasing of a laser beam by periodically poling the material so that the nonlinear coefficient changes its sign. This method, in fact, prevents destructive interferences between the second harmonic field and the driving field, and thus a reduction of the power of the second harmonic signal.[78]

[7]For a detailed description of the setup and the theoretical investigation of alkali-ion batteries, the Reader is referred to Chap. 4.

the charging of the battery, alkali-ion vacancies are created within the cathode material. The ions are then transported to the anode, where the formation of interstitials can be observed. These mechanisms will be referred to as ion deintercalation and ion intercalation, respectively, throughout this work. Simultaneously, the valence electrons are transported from one electrode to the other via an external circuit causing the oxidation or the reduction of suitable atoms in the cathode and anode, respectively.[14, 15]

In the case of KTP-type crystals, the oxidation takes place at the O_{Ti-Ti} atoms in $MTiOXO_4$ compounds[28], while the replacement of all O_{Ti-Ti} with F shifts the oxidation to the Ti sites (changing their oxidation number from $+3$ to $+4$)[33].
The reduction in the anode material, on the other hand, takes place at the Ti atoms[29].

In the case of KTP, the crystal lattice is characterized by a modest volume deformation both upon ion deintercalation[28] and intercalation[29]. This is crucial to guarantee a robust long-term operation, since it helps to prevent the fracture of the electrodes during (de)charging. In addition, the X-ion diffusion channels along [001] allow for efficient charging mechanisms, since they guarantee a fast ion diffusion through the crystal. However, the barriers, which have to be overcome, strongly depend both on the nature of the X and the M atoms: Notably, the diffusion barriers of the M^+ ions where found to be higher for smaller ionic radii (i. e., Li^+ or Na^+ ions) compared to $K^{+[29]}$.

In short, the application field of KTP crystals has recently been further enlarged. However, the above mentioned gray-tracking phenomenon could be detrimental also for battery applications, since it could indirectly lower the electronic flux in the material. The reasons shall now be explained in Sec. 2.3.

2.3 Gray Tracking in KTP Crystals

Gray tracks are the characteristic photochromic damage of KTP crystals. The formation of gray tracks can be observed after a number of processes, e. g., the application of strong electric fields[45–47], the reduction in H_2 atmospheres at high temperatures[88] or the irradiation with high-intensity laser light[41–44] or X rays[48]. Notably, in order to cause gray tracks by laser irradiation, 532-nm photons were found to be sufficient and necessary for the gray track formation.[43, 44]

During the gray track formation, two different stages can be identified: The first corresponds to the initial stage and is characterized by an increase of the absorption of the fundamental radiation at 1064 nm. In the second stage, also the absorption of the second harmonic (i. e., 532 nm) strongly increases.[46]

After their appearance, the crystals' properties are strongly affected and a series of negative effects can be measured: First of all, the formation of color centers does impair the optical transmission properties of the crystal due to a broad absorption band, which covers the whole visible spectrum, and shows maxima for wavelengths in the ranges of 380-440 nm and 500-600 nm.[89] In addition, the anisotropy of the linear optical properties is increased.[41] Moreover, the operation on damaged crystals can lead to their catastrophic failure.[43, 47, 50, 90] Thereby, the catastrophic damage is characterized by microcracks upon the formation of plasma, leading to the fracture of crystals.[91, 92]

Before catastrophic failure, gray tracking can be cured and the transmission can be restored by annealing at high temperatures. The chemical composition of the atmosphere and the an-

nealing time strongly influence the success of the annealing process. For example, Terashima *et al.*[93] found that annealing at 800 °C in air shifted the absorption onset towards shorter wave lengths and enhanced the overall transmission of undoped KTP crystals. Thereby, higher O contents in the annealing atmosphere corresponded to higher transmittances. The authors attributed the beneficial effects of the thermal and oxygen treatments to a facilitated lattice re-ordering and to a reduction of O vacancies, respectively. Loiacono *et al.*[43], on the contrary, measured an increased absorption after dry-oxygen annealing. In addition, they reported that wet-oxygen annealing could restore the transmission properties of KTP due to charge-stabilizing effects of OH$^-$ groups. Padberg *et al.*[45] found that annealing at 300°C for 12 h in an oxygen-enriched atmosphere leads to a complete curing of gray tracks and related absorptions, while their probes only partially recovered after annealing at 200°C for 80 h (see Fig. 2.3). Finally, Zhang *et al.*[88] observed a darkening of KTP crystals thermally treated in hydrogen atmospheres.

Mu and Ding[57] observed a second type of damage beside the visible damage. This damage appeared after the irradiation with a cw-pump argon laser at 514.5 nm polarized parallel to the [001] direction, and remains invisible (i. e., the typical dark traces are missing) even for higher beam powers. Nevertheless, a laser power higher than 4.5 W leads to the fracture of all samples. The origin of the invisible damage was thereby tentatively attributed to the drift of K$^+$ ions. The characteristic dark traces parallel to the *c* axis (and orange dots), on the other hand, appeared only for laser light perpendicular to [001].[57]

Other studies[41–43], however, found that the gray-track related absorption is the highest for second-harmonic radiation (i. e., 532 nm) polarized parallel to [001].

Despite numerous publications on gray tracking, there is still an ongoing research to clarify the mechanisms leading to gray track formation. The common hypothesis is that their appearance is strictly related to the reduction of Ti atoms as the result of charge compensation of special point defects.[47,49,50,53,54,88,90] The stabilization of the electrons leads to the transition from Ti^{4+} to Ti^{3+}. These reduced Ti atoms are usually referred to as Ti^{3+} centers.

Processes which cause gray tracks to form, in fact, can lead to the creation of free charges via, e. g., the creation of electron-hole pairs. If these electron-hole pairs do not recombine soon after their formation, they can be stabilized by intrinsic (or extrinsic) point defects. Within the KTP framework, holes are stabilized by O$_{Ti-Ti}$ near a K vacancy[74] (i. e., the same effect as the oxidation in a cathode) or Fe^{+2} substituting for Ti atoms[57]. Electrons can be stabilized by Ti atoms near O vacancies at the sites O$_{Ti-Ti}$[54] or by Pb^{2+} ions substituting for K^{+}[73].

In analogy to the Ti^{3+}-related absorption band in TiO$_2$-doped phosphate glasses between 400 nm and 700 nm[94], the reduction of Ti atoms has already been suggested by Loiacono *et al.*[43] as the origin of the broad absorption band after the irradiation with a Nd:YAG laser.

This hypothesis has been further enforced by the experimental detection of different Ti^{3+} centers via electron paramagnetic resonance spectroscopy (EPR)[47,49,54] and electron nuclear double resonance spectroscopy (ENDOR)[49,54].

According to Setzler *et al.*[54], four different Ti^{3+} centers, attributed to four different defects, can be identified in the KTP lattice. Interestingly, the growth method of the crystal determines the nature of the centers: Two centers can be found exclusively in hydrothermally grown KTP and are attributed to trapped H atoms by one O$_{Ti-Ti}$ present in the cell. One of them was attributed to a Ti(1) site, the other one to a Ti(2) site. The remaining two are restricted to flux-grown KTP and are caused either by a self-trapped electron at a Ti(1) site or by a positively
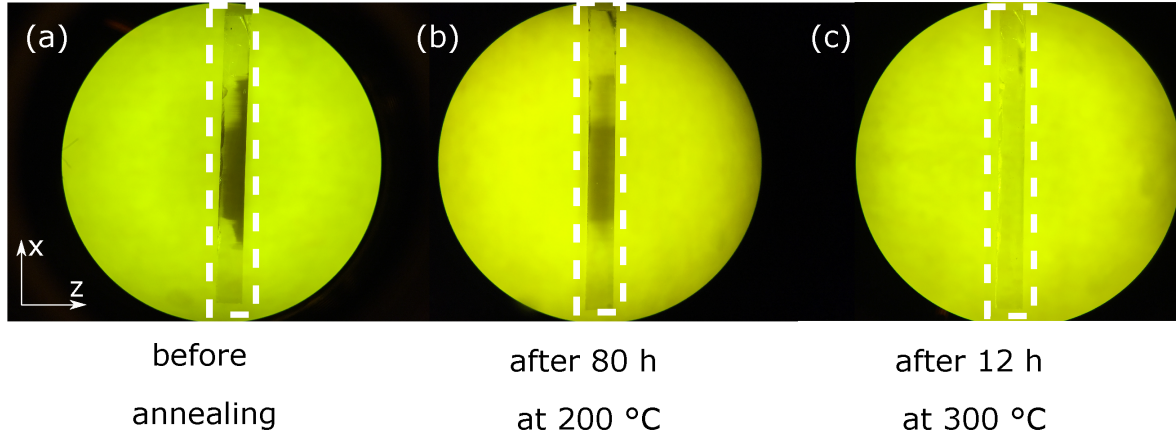
Figure 2.3: Gray-tracked KTP samples during different annealing stages. As indicated in (a), gray tracks form dark needles which grow into the crystal along the z axis. Image taken from Ref. 45.

charged O_{Ti-Ti} vacancy, which causes the reduction of a Ti(2) atom. Interestingly, only the O-vacancy-related center is stable at room temperature. The remaining centers decay for temperatures higher 140 K. Thus, we note that the formation of gray tracks might also indirectly hamper the (de)charging mechanisms of KTP electrodes by indirectly reducing the electron flux.

The defect models proposed by Setzler and co-workers[54] have been confirmed theoretically and partially revised in a later work[95].

To increase the resistivity of crystals against gray tracking, a number of strategies which reduce the number of K vacancies in the crystals were found to be effective. The first strategy consists of treatments to eliminate existing vacancies, for example potassium-nitrate treatments[45]. The second is a small Rb doping, which shows a larger activation energy for the ion migration along the c axis and thus blocks the migration channels for the K ions, leading to overall less K vacancies.[56]

Since the robustness of KTP crystals can be enhanced by increasing its K content (and therefore reducing the number of compensating O vacancies), it is reasonable to attribute a major role in the gray-tracking mechanisms to O vacancies. Nevertheless, the EPR-active charge state $+1$ is not the only energetically stable charge state of the vacancy. In fact, its formation energy[95] reveals that also the EPR-silent charge state $+2$ and $S = 1$ spin-configuration of the neutral vacancy are stable, and could also be relevant for gray tracking.

Nevertheless, the O-vacancy related Ti^{3+} center has recently also been detected within RTP crystals[96]. So, the presence of Ti^{3+} centers alone can not provide a complete explanation of the gray-tracking phenomenon, since a Rb doping was found to be beneficial to prevent its formation. This last aspect will be investigated further in Chap. 8.

3

A Brief Introduction to a Very Functional Theory

THE interconnected application of theoretical and experimental techniques is indispensable to deepen our knowledge about the fundamental laws which transform physical entities into something that we call universe. In fact, on the one hand, the value of a theory can only be quantified, if it is verified (or rather falsified) by an appropriate experimental setup. On the other hand, accompanying theoretical studies are crucial for the achievement of a thorough understanding of the underlying mechanisms. This holds, for example, during the investigation of the effects caused by specific point defects (or dopants) on the properties of a material.

In a very simplistic picture, a solid can be described as a many-body quantum-mechanical system composed of atomic nuclei surrounded by an electron cloud. The system is thereby stabilized by attractive forces. The state of the system is described by the corresponding many-body wave function Ψ, which depends both on all M nuclei and all N the electrons of the system. If we indicate their coordinates with r_i and R_J, respectively, the many-body wave function reads $\Psi\left(r_1, \ldots, r_N, R_1, \ldots, R_M; t\right)$ with t indicating the time. For the description of many ground-state properties of the system, however, the time-dependency can be neglected, leading to the stationary wave function $\Psi\left(r_1, \ldots, r_N, R_1, \ldots, R_M\right)$.

At least in principle, the system can be thus completely described by the solution of the corresponding time-independent Schrödinger equation

$$\hat{H}\,\Psi_n = E_n\Psi_n. \tag{3.1}$$

Here, $\hat{H}$ indicates the many-body Hamiltonian of the electrons and the nuclei of the system and E_n corresponds to the energy eigenvalues of the quantum state Ψ_n. The Hamiltonian thereby includes all the energy contributions to the total energy of the system. More precisely, if the kinetic energy contributions are indicated by $\hat{T}$, those which derive from the electrostatic interactions between charged components are denoted by $\hat{V}$ and the external energy contributions (e. g., external potentials caused by the presence of electric or magnetic fields) are summed up as $\hat{V}_{\text{ext.}}$, the Hamiltonian reads

$$\hat{H} = \hat{T} + \hat{V} + \hat{V}_{\text{ext.}}. \tag{3.2}$$

As mentioned above, a solid might be reduced to a system of negatively charged electrons and positively charged nuclei. If $m_{\text{el.}}$ and M_J are the respective masses, the corresponding kinetic energy contributions are expressed by the operators

$$\hat{T}_{\text{el.}} = -\sum_{i=1}^{N} \frac{\hbar}{2m_{\text{el.}}} \nabla_{r_i}^2 \quad \text{and} \quad \hat{T}_{\text{nuc.}} = -\sum_{J=1}^{M} \frac{\hbar}{2M_J} \nabla_{R_J}^2. \tag{3.3}$$

In addition, the electrostatic interactions correspond to the attractive (repulsive) Coulomb forces between electrons and nuclei. Since the charge of one electron corresponds to the elementary charge (i. e., e_0), and that of a nucleus depends on its atomic number (i. e., $Z_J e_0$), the operators take the forms

$$\hat{V}_{\text{el.}-\text{el.}} = \frac{1}{2} \sum_{i=1}^{N} \sum_{\substack{j=1, \\ j \neq i}}^{N} \frac{e_0^2}{4\pi\varepsilon_0} \frac{1}{|r_i - r_j|}, \tag{3.4}$$

$$\hat{V}_{\text{el.}-\text{nuc.}} = \frac{1}{2} \sum_{i=1}^{N} \sum_{J=1}^{M} \frac{e_0^2}{4\pi\varepsilon_0} \frac{Z_J}{|r_i - R_J|}, \tag{3.5}$$

$$\text{and} \quad \hat{V}_{\text{nuc.}-\text{nuc.}} = \frac{1}{2} \sum_{I=1}^{M} \sum_{\substack{J=1, \\ J \neq I}}^{M} \frac{e_0^2}{4\pi\varepsilon_0} \frac{Z_I Z_J}{|R_I - R_J|}, \tag{3.6}$$

with ε_0 as the vacuum permittivity. The form of the operator $\hat{V}_{\text{ext.}} = \sum_i v_{\text{ext.}}(r_i)$, with $v_{\text{ext.}}$ indicating the external potential, depends on the specific problem.[97]

At this point, the Reader will certainly agree that the exact, analytical solution the Schrödinger equation is only feasible for a few, simple model systems. So, to achieve a thorough insight into the properties of a realistic many-body system, numerical treatments are required. Two different approaches are possible:[97]

(i) Pure *ab initio* calculations[1], which do not require any empirical parameter;

(ii) The modeling of an *ad hoc* Hamiltonian, which enables the calculation of a few properties of interest at a reduced computational cost. However, the introduction of empirical parameters is required here to properly describe the system.

In both cases, the computational effort must often be additionally reduced by the introduction of approximations[2].

One of the most successful *ab initio* techniques is the so-called density functional theory (DFT), based on the works of Hohenberg and Kohn[102] and Kohn and Sham[103]. Within DFT, the ground state of a system can be determined at an affordable computational cost, since it replaces the determination of the ground-state wave function via the direct solution of the respective Schrödinger equation, by the determination of the ground-state electron density $n_0(r)$ of the system.

---

[1]*Ab initio* or "from first principles" calculations provide the solution of the Schrödinger equation under the prerequisite that the only parameters which have to be provided correspond to physical constants.

[2]Two common approximations are the Born-Oppenheimer[98] and the Hartree-Fock approximation[99–101]. Within the former the motion of the nuclei is neglected, within the latter the many-body wave function is calculated as the Slater determinant of single-particle wave functions.

Following the discussion of Ref. 97, the fundamental concepts of DFT shall now be introduced, starting from the formulation of the Hohenberg-Kohn theorems and the Kohn-Sham equations in Sec. 3.1. In Sec. 3.2, we will describe how the interaction of electrons can be approximated via the so-called exchange and correlation potential. Finally in Sec. 3.3, the origin of a major drawback of the theory, i.e., the underestimation of the band-gap width, will be discussed.

For the sake of simplicity, only the non-relativistic case will be considered. Furthermore, it is assumed that only interactions of the valence electrons can contribute to changes of the total energy of the system. In addition, the ground state is supposed to be energetically non-degenerate and the temperature is fixed to $0\,\mathrm{K}$. In addition, CGS units will be used.

3.1 The Hohenberg-Kohn Theorems and the Kohn-Sham Equations

The fundamental idea behind DFT relies on two theorems formulated and proven by Hohenberg and Kohn in 1964[102]. Thanks to these theorems, it was shown that the determination of the ground-state wave function of a many-body system with N electrons is equivalent to the calculation of its ground-state electron density $n_0(\boldsymbol{r})$, rendering the solution of the corresponding Schrödinger equation 3.1 obsolet. As one of the main consequences, these theorems reduce the degrees of freedom from $3N$ to 3 and thus the computational costs.

According to Hohenberg and Kohn, there is a unique mapping between the external potential v_{ext}, the ground-state $|\Psi_0\rangle$ and its electron density, more precisely,

$$v_{\mathrm{ext}} \Longleftrightarrow |\Psi_0\rangle \Longleftrightarrow n_0(\boldsymbol{r}) = \left\langle \Psi_0 \left| \sum_{i=1}^{N} \delta(\boldsymbol{r} - \boldsymbol{r}_i) \right| \Psi_0 \right\rangle . \tag{3.7}$$

This has a series of consequences:

 (i) The system is in its ground state when the electron density is in its ground state, i.e., $|\Psi_0\rangle = |\Psi[n_0(\boldsymbol{r})]\rangle$;

 (ii) Not only the external potential determines the ground-state electron density of a system, but also the ground-state electron density does determine the external potential (at least up to an additive constant);

(iii) Since the external potential solely depends on $n(\boldsymbol{r})$ and the external potential is the only external contribution to the total energy of the system, also the energy $E[n]$ of the many-body system is a unique functional of the electron density. In addition, every property (observable) of the system is a functional of the electron density.

This leads to the formulation of the first Hohenberg-Kohn theorem[102]:

Theorem 3.1. *The ground-state energy E_0 of a system is a unique functional of the ground-state electronic density n_0.*

The first theorem ensures that the computation of the electron density, for which the ground-state energy is assumed, is equivalent to the solution of the Schrödinger equation of the system. The second theorem by Hohenberg and Kohn, on the other hand, provides the scheme, which allows for the determination of the ground-electron density. It reads[102]:

Theorem 3.2. *The ground-state electron density n_0 corresponds to the absolute minimum E_0 of the total energy $E[n]$ of the system under consideration.*

Therefore, the ground state of a system can be identified by applying the Ritz variational principle[104] on the energy functional $E[n]$, which assumes its minimum for n_0.

Although the procedure seems to be straight forward, the computation of the ground-state energy is not trivial at all. In fact, the energy of the system includes, beside the (easily calculable) contributions of the external potential $v_{ext.}$, all the internal energy contributions, caused by the motion and the interaction of electrons and nuclei of the system as well as quantum-mechanical effects. In their paper, Hohenberg and Kohn[102] already suggested to split the known from the unknown contributions, by introducing the fundamental functional $F[n(\boldsymbol{r})]$ which includes all the internal energy contributions. This leads to the expression

$$E[n] = \int v_{ext.}(\boldsymbol{r}) n(\boldsymbol{r}) \, d\boldsymbol{r} + F[n] \tag{3.8}$$

for the energy of a system within an external potential $v_{ext.}$.

Later, in 1965, Kohn together with his post-doctoral fellow Sham[103] refined this concept, shaping $F[n]$ and presenting a self-consistent scheme which allows for the computation of a system's ground-state energy: The so-called Kohn-Sham equations.

Following the suggestion by Kohn and Sham[103], the total energy of a system of interacting particles can be expressed as follows

$$\begin{aligned} E[n] &= \frac{1}{2} \int \int \frac{n(\boldsymbol{r}) n(\boldsymbol{r}')}{|\boldsymbol{r} - \boldsymbol{r}'|} \, d\boldsymbol{r} \, d\boldsymbol{r}' \quad &+ \int v_{ext.}(\boldsymbol{r}) n(\boldsymbol{r}) \, d\boldsymbol{r} \quad &+ T_s[n(\boldsymbol{r})] \quad &+ E_{XC}[n(\boldsymbol{r})] \\ &= E_H[n] \quad &+ E_{ext.}[n] \quad &+ T_s[n] \quad &+ E_{XC}[n]. \end{aligned} \tag{3.9}$$

Here, E_H is the Hartree energy, which corresponds to the mean-field Coulomb interaction of a particle with all the electrons in the system, $E_{ext.}$ is the influence of any external potential, and T_s is the kinetic energy of N non-interacting particles. The term E_{XC}, on the other hand, is the so-called exchange and correlation energy. It includes all the many-body effects which arise from interaction between particles. Unfortunately, there is no universally valid expression for E_{XC}. Nevertheless, some approximations have been derived to account for the exchange and correlation effects. Two common approaches will be presented in Sec. 3.2.

Coming back to the formulation of the Kohn-Sham equations, the expression in Eq. 3.9 has to be minimized following the Hohenberg-Kohn variational principle[102]. For this, a probe electron density $\tilde{n}(\boldsymbol{r})$ is inserted in the expression of the energy functional, and it is varied until the minimum energy E_0 is identified, i.e.,

$$E[\tilde{n}] = E_H[\tilde{n}] + E_{ext.}[\tilde{n}] + T_s[\tilde{n}] + E_{XC}[\tilde{n}] \geq E_0. \tag{3.10}$$

Obviously, the ground-state electron density must fulfill the condition $E[n_0] = E_0$.

Under the condition that the number of electrons of the system does not change under the variation of $\tilde{n}(\boldsymbol{r})$, i.e., $\int \tilde{n}(\boldsymbol{r}) \, d\boldsymbol{r} = N$, the Euler-Lagrange equation

$$\delta E[\tilde{n}(\boldsymbol{r})] = \int \delta\tilde{n}(\boldsymbol{r}) \left\{ v_{eff.}(\boldsymbol{r}) + \frac{\delta}{\delta\tilde{n}(\boldsymbol{r})} T_s[\tilde{n}(\boldsymbol{r})] \bigg|_{\tilde{n}(\boldsymbol{r})=n(\boldsymbol{r})} - \epsilon \right\} d\boldsymbol{r} = 0 \tag{3.11}$$

can be formulated. Here, ϵ is the Lagrange multiplier which guarantees the conservation of the number of particles, and $v_{\text{eff.}}$ is an effective potential in which the electrons are inserted. More precisely, $v_{\text{eff.}}$ does account for every energy contribution except for that of the kinetic energy T_{s} of the electrons of the system, i. e.,

$$v_{\text{eff.}}(\boldsymbol{r}) = v_{\text{ext.}}(\boldsymbol{r}) + v_{\text{H}}(\boldsymbol{r}) + v_{\text{XC}}(\boldsymbol{r}), \tag{3.12}$$

where the Hartree and the XC potentials are defined as

$$v_H = \int \frac{n(\boldsymbol{r'})}{|\,\boldsymbol{r} - \boldsymbol{r'}\,|}\, \mathrm{d}\boldsymbol{r'} \quad \text{and} \quad v_{\text{XC}} = \frac{\delta}{\delta\tilde{n}(\boldsymbol{r})} E_{\text{XC}}[\tilde{n}(\boldsymbol{r})]\Big|_{\tilde{n}(\boldsymbol{r})=n(\boldsymbol{r})}. \tag{3.13}$$

Note that by this, the solution of the many-body problem from which we started has been reduced to a Lagrange equation of non-interacting particles within an effective potential.

So, if $|\varphi_i\rangle$ indicates the single-particle wave functions of the components of the system, the electron density $n(\boldsymbol{r})$ of the system itself can be determined by solving the single-particle Schrödinger-like equations

$$\left(-\frac{1}{2}\nabla^2 + v_{\text{eff.}} - \epsilon_i\right)|\varphi_i\rangle = 0 \tag{3.14}$$

with

$$n(\boldsymbol{r}) = \sum_{i=1}^{N} |\varphi_i(\boldsymbol{r})|^2 \tag{3.15}$$

and

$$v_{\text{eff.}}(\boldsymbol{r}) = v_{\text{ext.}}(\boldsymbol{r}) + \int \frac{n(\boldsymbol{r'})}{|\,\boldsymbol{r} - \boldsymbol{r'}\,|}\, \mathrm{d}\boldsymbol{r'} + v_{\text{XC}}(\boldsymbol{r}). \tag{3.16}$$

Equations 3.14-3.16 are the so-called Kohn-Sham equations.[103]

At this point some conclusions can be drawn: First of all, the Kohn-Sham eigenfunctions $|\varphi_i\rangle$ are deprived from any physical meaning. So, they can not be directly used to determine the ground-state wave function Ψ_0 of the system under consideration, as it is, e. g., performed within the Hartree-Fock approximation via their Slater determinant. Nevertheless, they allow for the calculation of the ground-state electron density via Eq. 3.15, which then determines Ψ_0. In addition, since the expression for $v_{\text{eff.}}$ depends itself on the electron density $n(\boldsymbol{r})$ which has to be determined, the problem has to be solved self-consistently. Finally, since the Coulomb potential is singular in the vicinity of the nuclei, the Kohn-Sham potentials are usually substituted with smoother potentials (the so-called pseudopotentials). However, because of the form of the wave functions near the nuclei not having a strong impact on the physical and chemical properties of one material, the errors deriving from this approximation are often negligible.[97]

3.2 Exchange and Correlation Energy within DFT

The power of DFT calculations, beside comparatively low computational costs, is that no approximation nor empiric parameter has to be included to determine the properties of a system.

Unfortunately, this holds only theoretically: The internal contributions to the total energy of an ensemble of atoms is not equal to the sum of all the energies of every single particle. In fact, additional energy terms arising from the interaction of these particles as well as quantum-

mechanical effects have to be accounted for. Within the framework of DFT, all the unknown energy contributions are commonly summarized in the so-called exchange and correlation (XC) energy E_{XC}.

Two most common approximations for E_{XC} are thereby the local density approximation (LDA) and the generalized gradient approximation (GGA). Both will be briefly described in the following.

The Local Density Approximation   The LDA is the approach proposed by Kohn and Sham[103]. Within this formalism it is assumed that the electron density of the system can be approximated by the electron density $n = n(r)$ of a homogeneous electron gas. Although it is not yet possible to define an explicit expression for E_{XC}, it can be calculated using the exchange-correlation energy per electron $\epsilon_{XC} = \epsilon_X + \epsilon_C$ as

$$E_{XC} = \int \epsilon_{XC}[n(r)]n(r)\,dr, \tag{3.17}$$

unter the constraint of a quasi-stationary electron density $n(r)$.[103]

Thereby, the exchange energy per electron can be directly derived from Hartree-Fock theory as[105]

$$\epsilon_X^{LDA} = -\frac{3}{4\pi}\left(\frac{3}{\pi^2}n(r)\right)^{\frac{1}{3}}. \tag{3.18}$$

The calculation of the correlation energy per electron, on the other hand, is non-trivial and can be achieved by, e. g., Monte Carlo simulations as done by Ceperley and Alder[106]. Their results have then later been parametrized by Perdew and Zunger[107] leading to the following expression for the correlation energy per electron

$$\epsilon_C^{LDA} = \frac{\gamma}{1 + \beta_1\sqrt{r_s} + \beta_2 r_s} \tag{3.19}$$

with $r_s = \sqrt[3]{\frac{3}{4\pi n}}$ indicating the Wigner-sphere radius, $\gamma = -0.14230$, $\beta_1 = 1.05290$ and $\beta_2 = 0.3334$. Note that this expression refers to the spin-unpolarized case, but the scheme of Perdew and Zunger is also applicable to spin-polarized systems, yieldingthe local spin-density approximation (LSDA).

At this point it has to be pointed out that the correlation contributions to the energy of a system are usually smaller compared to the exchange contributions. In addition, the LDA often profits from error cancellation due to an underestimation of E_X and an overestimation of E_C. For this reason, although its accuracy is higher if the system can be approximated as a homogeneous electron gas (for example a metal), the LDA scheme can provide fruitful results also for systems featuring inhomogeneities in the electron density. Nevertheless, one major drawback of the LDA is that it is not capable to describe negative atomic ions.[97]

One direct improvement of the LDA is the inclusion of local fluctuations of the electron density via its gradient as within the generalized gradient approximation.

The Generalized Gradient Approximation   Although it has already been successfully applied to many systems, the LDA scheme based on a uniform electron distribution does not

account for natural fluctuations of the electron density of real systems, for example due to ionic and covalent bonds between atoms. In addition, the LDA does not account for the so-called exchange-correlation hole $n_{XC}(r, r')$. This corresponds to the area around each electron in which, due to the Pauli principle and the electron-electron repulsion, the probability to find another electron is zero. Illustratively, each electron at the position r induces a hole in the average density $n(r')$. Thereby the normalization

$$\int n_{XC}(r, r') \, dr' = -1 \tag{3.20}$$

holds, which corresponds to the total screening of the electron at the position r.[108]

To properly account for these effects, local fluctuations of the electron density have to be considered. This is achieved within the framework of the generalized gradient approximation (GGA) via the gradient of the electron density $\nabla n(r)$ so that the value of the XC functional can be written as[109]

$$E_{XC}^{GGA}[n] = \int f[n(r), |\nabla n(r)|] \, dr. \tag{3.21}$$

Compared to the LDA, the GGA provides a better approximation of the exchange and the correlation, leading to a better description of total energies.[97] Some largely applied parametrizations of the GGA are the one by Perdew and Wang (PW91)[110], the one by Perdew, Burke and Ernzerhof (PBE)[109], or its extension by Perdew *et al.* for solid-state systems (PBEsol)[111,112], which provides a more accurate prediction of lattice constants. Details can be found in the corresponding references.

Unfortunately, both the LDA and the GGA suffer from a major problem: An inaccurate description of electronic self-energy effects. This has two major consequences: The first is the prediction of the so-called fundamental band gap width E_g of insulators and semiconductors, which is always underestimated. The second is the insufficiently accurate description of ground states characterized by strongly localized electrons.[113]

Some strategies to overcome these problems will be discussed in Secs. 3.3-3.6.

3.3 Overcoming the Band-Gap Problem

Unlike a metal, a semiconductor (or an insulator) does not allow for electronic conductivity at zero-temperature. This characteristic is caused by the presence of a rather large fundamental band gap E_g. In semiconductors, the band gap corresponds to the energy gap which divides the highest occupied state (HOMO), i. e., the valence band maximum (VBM), from the lowest unoccupied state (LUMO), located at the bottom of the conduction band (CBM). It can, however, be shown (see for example Ref. 97) that band gaps predicted via standard DFT calculations always underestimate the corresponding experimental band-gap widths.

The band-gap width is defined as the difference between the electron affinity and the first ionization energy (i. e., the energy needed to add and remove one electron to (from) the neutral system, respectively). If E_0^N indicates the ground-state energy of a system with N electrons, the magnitude of E_g can be quantified as follows[97,114,115]

$$E_g = \left[E_0^{N+1} - E_0^N \right] - \left[E_0^N - E_0^{N-1} \right]. \tag{3.22}$$

This is the so-called ΔSCF method. For non-interacting particles, the energy differences can be replaced with the orbital energies of the Kohn-Sham eigenstates as $E_0^{N+1} - E_0^N = \epsilon_{N+1}$ and $E_0^N - E_0^{N-1} = \epsilon_N$. The so-calculated band-gap width would correspond to the difference[97,114,115]

$$\Delta_s = \epsilon_{N+1} - \epsilon_N. \tag{3.23}$$

Unfortunately, Δ_s does not correspond to the real band gap when interacting particles are considered. The reason for this systematic underestimation of fundamental band-gap widths is the so-called self-interaction[3] error Δ_{XC}. More precisely, the total energy of a system in dependance of the number of electrons can be described as straight-line segments (see Fig. 3.3), whose slopes change for integer occupation numbers. For this reason, the functional derivatives for integer electron numbers will be discontinuous in these points. The origin of the band gap of the system is caused by exactly this discontinuities. In the DFT framework, only the kinetic and the exchange-correlation contributions to the total energy can be discontinuous. It can be shown that Δ_s describes the discontinuity in the kinetic energy, those attributable to the exchange and correlation effects (i. e., Δ_{XC}), on the other hand, are not exactly known. The difference between the real band gap and Δ_s thus corresponds precisely to Δ_{XC}. So, to determine the real band gap of a system this self-interaction error has to be accounted for, leading to[97,114,115]

$$E_g = \epsilon_{N+1} - \epsilon_N + \Delta_{XC}. \tag{3.24}$$

An immediate effect of the underestimation of the fundamental band gap arises during the computation of optical properties. In fact, within the DFT framework, optical spectra usually suffer from a severe red-shift compared to corresponding experimental measurements.

In 1981 Perdew and Zunger[107] proposed the so-called self-interaction correction (SIC) method, which allows for directly correcting the self-interaction error by enforcing that each particle can interact with other particles, exclusively. This, however, holds the disadvantage of being computationally very demanding.

Beside the SIC method, three most established approaches, which provide a better cancellation of electronic self-interaction are the *GW* approximation, the inclusion of the Hubbard correction (DFT+*U*), and the application of hybrid functionals.

3.4 The Quasiparticle Picture and the *GW* Approximation

Band gaps of semiconductors and isolators can be experimentally determined by a combination of direct and inverse photoemission spectroscopy. Thereby, the sample is irradiated with a photon with the energy $\hbar\omega$ or an electron with the kinetic energy E_{kin}, respectively. Consequently, an electron with the kinetic energy E_{kin} or a photon with the energy $\hbar\omega$ will be emitted, while the number of electrons in the system changes. If the Coulomb interaction is neglected, these experiments allow for the calculation of the binding energy of the electron via $\epsilon_i = E_{kin} - \hbar\omega$. Generally speaking, however, the binding energy of the electron corresponds to the energy difference of the system in its N-particle ground state and the $(N-1)$-particle (or $(N+1)$-particle) excited state, i. e., respectively, $\epsilon_i = E_0^N - E_i^{N-1}$ or $\epsilon_i = E_i^{N+1} - E_0^N$.[116]

---

[3]The self-interaction problem is an intrinsic problem of the DFT framework. In fact, since Kohn-Sham DFT utilizes the full electron density, the repulsion of an electron with its own charge density is included. This unphysical interaction is commonly referred to as self interaction.
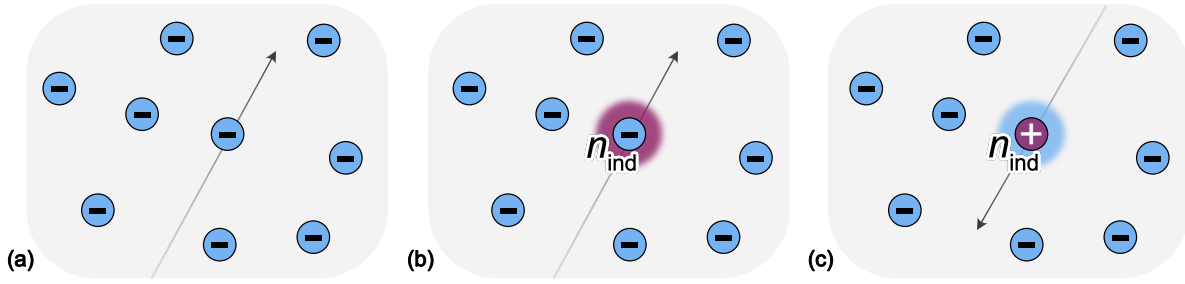
Figure 3.1: Schematic propagation of a (a) bare electron, (b) a quasi-electron and a (c) quasi-hole in an N-electron system.

To theoretically describe this kind of processes involving a non-constant number of particles, many-body perturbation theory based on the Green's function $G(\boldsymbol{r}, t; \boldsymbol{r}', t')$ can be utilized.

Before discussing this formalisms, however, it is important to note that when an electron is inserted in an N-electron system, it can not be longer treated as a bare particle. In fact, the interactions between this electron and the N electrons already in the system has to be considered. Due to the Pauli principle and repulsive Coulomb forces, in fact, the electron will be surrounded by a positively charged cloud, which screens the electron: The XC hole. In analogy, the extraction of one electron will cause a positively charged hole surrounded by a negatively charged screening cloud (also see Fig. 3.1). The combination of this electron (hole) with the surrounding charge cloud is commonly referred to as quasiparticle. A direct consequence of the unavoidable screening is that the quasiparticle will show a smaller effective charge compared to the bare electron and thus a smaller (screened) Coulomb interaction $W(\boldsymbol{r}, \boldsymbol{r}'; \omega)$ compared to the bare Coulomb potential $v(\boldsymbol{r}, \boldsymbol{r}')$. Thereby, the relation[116]

$$W(\boldsymbol{r}, \boldsymbol{r}', \omega) = \int \varepsilon^{-1}(\boldsymbol{r}, \boldsymbol{r}''; \omega) v(\boldsymbol{r}'', \boldsymbol{r}') \, \mathrm{d}^3 r''$$

$$= v(\boldsymbol{r}, \boldsymbol{r}') + \int n_{\mathrm{ind}}(\boldsymbol{r}, \boldsymbol{r}''; \omega) v(\boldsymbol{r}'', \boldsymbol{r}') \, \mathrm{d}^3 r'' \tag{3.25}$$

holds, with ε^{-1} as the inverse of the dielectric function[4] and n_{ind} the screening cloud.

Coming back to the description of excited states which will follow Refs. 116 and 117 , the Green's function describes the probability amplitude for the propagation of a quasiparticle in spacetime from its creation at $(\boldsymbol{r}, t)$ to $(\boldsymbol{r}', t')$. Thereby the conditions $t' > t$ and $t' < t$ hold for an electron and hole, respectively, to guarantee causality. The Green's function reads[117]

$$G(\boldsymbol{r}, t; \boldsymbol{r}', t') = -i \left\langle N \left| \hat{T} \left[\hat{\psi}(\boldsymbol{r}', t') \hat{\psi}^\dagger(\boldsymbol{r}, t) \right] \right| N \right\rangle, \tag{3.26}$$

with $|N\rangle$ indicating the ground state in the Heisenberg picture[5], $\hat{\psi}^{(\dagger)}(\boldsymbol{r}, t)$ is the annihilation (creation) operator and $\hat{T}$ the Wick[118] time-ordering operator[6].

As the electronic ground-state density $n(\boldsymbol{r})$, $G(\boldsymbol{r}, t; \boldsymbol{r}', t')$ allows for the calculation of ground-

---

[4]The computation of optical properties within the DFT framework will be addressed in Chap. 6.

[5]Within the Heisenberg picture, state vectors are time-independent and the time dependency is included in the operators.

[6]$\hat{T}$ orders all the operators in descending time order (from left to right). In the case of fermionic operators, each operator swapping will introduce a factor of -1.

state properties of the system under consideration. In addition, it holds the advantage to also include all the excitation energies of the $(N \pm 1)$-electron system. This is clearly visible from the Lehmann representation of the Green's function in the frequency domain[116]

$$G(\boldsymbol{r}, \boldsymbol{r}'; \omega) = \sum_i \frac{\psi_i^{N+1}(\boldsymbol{r})\psi_i^{N+1*}(\boldsymbol{r})}{\hbar\omega - \epsilon_i^{N+1} + i\eta} + \sum_i \frac{\psi_i^{N-1}(\boldsymbol{r})\psi_i^{N-1*}(\boldsymbol{r})}{\hbar\omega - \epsilon_i^{N-1} - i\eta}, \quad (\eta \to 0^+). \tag{3.27}$$

In the quasiparticle picture, the $\psi_i^{N\pm1}$ and $\epsilon_i^{N\pm1}$ in Eq. 3.27 are the quasiparticle wave functions and quasiparticle energies, respectively. So, the latter directly correspond to the excitation energies of the $(N+1)$-electron and $(N-1)$-electron system as measured via photoemission spectroscopy. In the case of non-interacting electrons, on the other hand, the $\epsilon_i^{N\pm1}$ correspond to the single-particle energies and the $\psi_i^{N\pm1}$ to the (un)occupied single-particle wave functions.

In the following, we will use a short-hand notation, which expresses coordinates in space-time using natural numbers. More precisely, $i \in N_0$ will be used to indicate the space-time-coordinates $(\boldsymbol{r}_i; t_i)$, or rather i^+ for $(\boldsymbol{r}_i, t_i + \eta)$ $(\eta > 0)$. Consequently, the following expressions hold: $\delta(i-j) \equiv \delta(\boldsymbol{r}_i, -\boldsymbol{r}_j)\delta(t_i - t_j)$, $v(ij) \equiv v(\boldsymbol{r}_i, \boldsymbol{r}_j)\delta(t_i - t_j)$, and $\int \mathrm{d}i \equiv \int \mathrm{d}^3\boldsymbol{r}_i \int_{-\infty}^{\infty} \mathrm{d}t_i$.

Using this notation, the equation of motion for the propagation of the quasiparticle reads[116,117]

$$\left[i\frac{\partial}{\partial t_1} - \hat{H}_0(\boldsymbol{r}_1)\right] G(1, 2) - \int \Sigma(1, 3)G(3, 2)\,\mathrm{d}3 = \delta(1 - 2), \tag{3.28}$$

with $\hat{H}_0 = -\frac{1}{2}\nabla^2 + v_\mathrm{H} + v_\mathrm{ext.}$ as the Hamiltonian of the mean field and the self-energy operator Σ accounting for all the exchange and correlation effects. Thereby, Σ allows for the calculation of the energy difference between a bare particle and the corresponding quasiparticle[117].

Eq. 3.28 can be reformulated in order to explicitly include the Green's function $G_0(\boldsymbol{r}, \boldsymbol{r}'; \omega)$ of the mean-field system, i. e., the system without self-energy effects, into the Dyson-like equation[116]

$$G(1, 2) = G_0(1, 2) + \iint G_0(1, 3)\Sigma(3, 4)G(4, 2)\,\mathrm{d}3\,\mathrm{d}4. \tag{3.29}$$

Note that by inserting Eq. 3.27 in the Dyson equation Eq. 3.29, one can derive the quasiparticle equation[116]

$$\hat{H}_0(\boldsymbol{r})\psi_i(\boldsymbol{r}) + \int \Sigma\left(\boldsymbol{r}, \boldsymbol{r}'; \frac{\epsilon_i}{\hbar}\right)\psi_i(\boldsymbol{r})\,\mathrm{d}\boldsymbol{r}' = \epsilon_i\psi_i(\boldsymbol{r}) \tag{3.30}$$

with $\psi_i(\boldsymbol{r})$ indicating again the quasiparticle wave functions, and ϵ_i the quasiparticle energies.

In 1965, Hedin[119] derived a set of five integro-differential equations, whose self-consistent solution provides the exact solution of the Green's function[7]: The so-called Hedin's[119] or Hedin-Lundqvist[120] equations. Usually, the utilized self-consistent scheme is schematized via the pentagon in Fig. 3.2.

In the following, we will shortly discuss the main aspects of this formalism, a more detailed description can be found, e. g., in Refs. 116, 117, 119, 121, 122.

The Hedin's equations can be formulated by adopting the Dyson's formulation of Eq. 3.28 with G_0 as the Green's function of the mean field. This leads to the following integro-differential equations[116,117,119]

---

[7]For the proof, Hedin calculated the system's response to a time-dependent test potential, which was set to 0 at the end.[119]
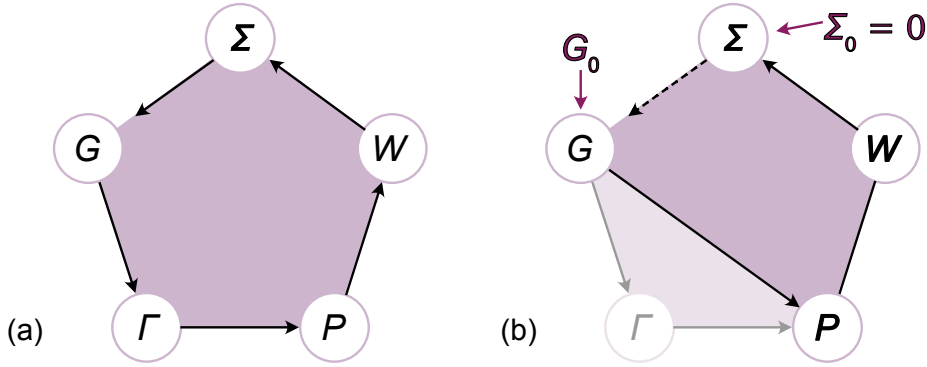
Figure 3.2: Self-consistent solution of Hedin's equations before (a) and after (b) the *GW* approximation using the Green's function G_0 of the mean field as the starting point. Although the scheme can be self-consistently iterated, usually one stops after the zeroth or the first iteration, so that the *GW* should actually be referred to as $G_0 W_0$ approximation. The first iteration of the scheme is required for the solution of the Bethe-Salpeter equation, also see Sec. 6.1.2.

$$G(1, 2) = G_0(1, 2) + \iint G_0(1, 3)\Sigma(3, 4)G(4, 2)\, \mathrm{d}3\, \mathrm{d}4, \tag{3.31}$$

$$\Gamma(1, 2; 3) = \delta(12)\delta(13) + \iiiint \frac{\delta\Sigma(1, 2)}{\delta G(4, 5)}G(4, 6)G(7, 5)\Gamma(6, 7; 3)\, \mathrm{d}4\, \mathrm{d}5\, \mathrm{d}6\, \mathrm{d}7, \tag{3.32}$$

$$P(1, 2) = -i \iint G(2, 3)\Gamma(3, 4; 1)G(4, 2)\, \mathrm{d}3\, \mathrm{d}4, \tag{3.33}$$

$$W(1, 2) = v(1, 2) + \iint v(1, 3)P(3, 4)W(4, 2)\, \mathrm{d}3\, \mathrm{d}4, \tag{3.34}$$

$$\Sigma(1, 2) = i \iint G(1, 4)W(1^+, 3)\Gamma(4, 2; 3)\, \mathrm{d}3\, \mathrm{d}4. \tag{3.35}$$

Here, W denotes the screened Coulomb potential, P the polarizability, Σ the self-energy and Γ is the three-point vertex function. In addition, v refers again to the bare Coulomb potential, i. e., the electrostatic interaction between a bare electron and the system.

Unfortunately, a direct solution of Hedin's equations is impossible without a number of approximations. The approach proposed by Hedin[119], is to set $G = G_0$ and to completely neglect exchange and correlation effects, i. e., by setting $\Sigma \equiv 0$, for the zeroth iteration. This approximation is usually referred to as random-phase approximation (RPA)[117]. As a consequence, Σ is approximated as the product of the Green's function (G) with the screened Coulomb interaction (W). For this reason, this approximation was later called *GW* approximation.

With these simplifications, Hedin's equations assume the form[116,117]

$$G(1, 2) = G_0(1, 2) + \iint G_0(1, 3)\Sigma(3, 4)G(4, 2)\, \mathrm{d}3\, \mathrm{d}4, \tag{3.36}$$

$$\Gamma(1, 2; 3) = \delta(1 - 2)\delta(1 - 3), \tag{3.37}$$

$$P(1, 2) = -i\hbar G_0(1, 2)G_0(2, 1), \tag{3.38}$$

$$W(1, 2) = v(1, 2) + \iint v(1, 3)P(3, 4)W(4, 2)\, \mathrm{d}3\, \mathrm{d}4, \tag{3.39}$$

$$\Sigma(1, 2) = i\hbar G_0(1, 2)W(1^+, 2). \tag{3.40}$$

In order to reduce computational costs, usually only the first iteration is actually carried out (G_0W_0). This, however, still guarantees a reliable description of band-gap widths of many systems, especially when combined with hybrid functionals[123].

3.5 Describing Strongly Localized Shells: The Hubbard Correction

In Sec. 3.4, we discussed how the inclusion of self-energy effects can improve the prediction of band gaps. However, beside this problem, the self-interaction problem can have more serious consequences during the description of systems featuring strongly localized states, i.e., elements of the d and f blocks. In fact, since every electron does partially repel itself, wave functions can be over-delocalized. This lead to delocalized valence electrons, promoting the erroneous prediction of stable metallic ground states.[124] As a consequence, computations can result in unreliable magnetic ground states, for example in the case of Mott insulators[125], or systems featuring strongly localized defect states[124].

The so-called DFT+U[8], first introduced by Anisimov and co-workers[126–128], is based on the Hubbard model[129–134] and represents a convenient approach to overcome the delocalization of states. Within this picture, the total energy can be calculated by correcting the approximate energy E_{DFT} as computed using (semi)local functionals with the term E_{Hub} derived from the Hubbard Hamiltonian for the modeling of localized states as[124,135]

$$E_{\text{DFT}+U}[n(\boldsymbol{r})] = E_{\text{DFT}}[n(\boldsymbol{r})] + E_{\text{Hub}}\left[\left\{n_{mm'}^{I\sigma}\right\}\right] - E_{\text{dc}}\left[\left\{n^{I\sigma}\right\}\right]. \qquad (3.41)$$

Here, $n_m^{I\sigma}$ represents the atomic-orbital occupations of the atom at the site I on which the correction shall be applied, with σ as the spin and m the magnetic quantum number. The third term E_{dc} in Eq. 3.41 is the so-called double-counting (dc) energy required to cancel out the parts of the interactions accounted for both by E_{DFT} and E_{Hub}. The double-counting energy thereby depends on the total, spin-projected occupation of the correlated manifold $n^{I\sigma} = \sum_m n_m^{I\sigma}$.[124,135]

The form of E_{dc} is not exactly known and many different definitions can be found in literature. In its original formulation[126], the energy terms were defined as follows

$$E_{\text{LDA}+U} = E_{\text{LDA}} + \frac{U}{2}\sum_{\substack{m,m',\\ \sigma}}\left(n_m^{I\sigma} - n_0\right)\left(n_{m'}^{I-\sigma} - n_0\right) + \frac{U-J}{2}\sum_{\substack{m,m',\\ \sigma\\ (m\neq m')}}\left(n_m^{I\sigma} - n_0\right)\left(n_{m'}^{I\sigma} - n_0\right),$$

with n_0 indicating the average occupancy. In the case of, e.g., a d orbital, this corresponds to $n_0 = n_d/10$.[126] The parameters U and J, on the other hand, correspond to the Hubbard parameter (i.e., the screened Coulomb repulsion) and the Hund's-exchange parameter (i.e., the Stoner parameter), respectively.[126,135]

To understand why the Hubbard correction overcomes the artificial delocalization of states, it is helpful to refer to the potential of the system. In the so-called fully localized limit, the

---

[8]In its original formulation, the Hubbard correction was applied on LDA functionals so that it was later referred to as LDA+U. However, since it can also be applied to other functionals, we will adopt the more general nomenclature DFT+U, where "DFT" shall be substituted with a suitable functional.
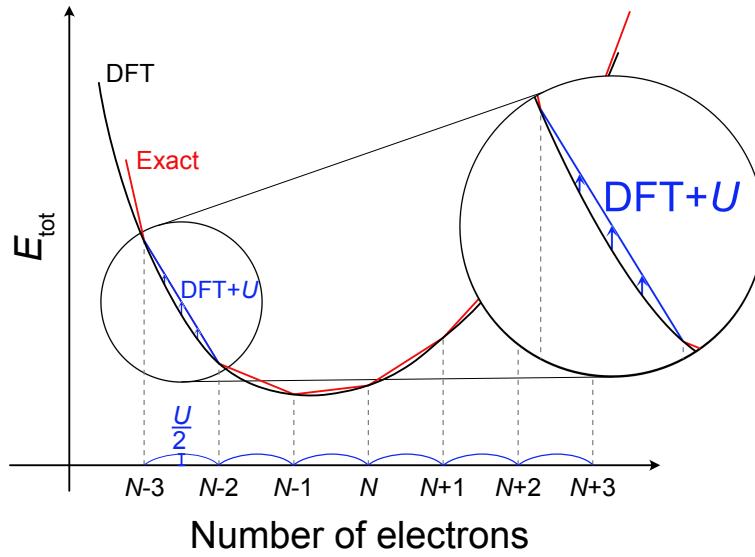
Figure 3.3: Schematic representation of the total energy E_{tot} of a system in dependence of the number of electrons. The red curve indicates the exact (real) piecewise linear energy profile. The black curve, on the other hand, represents the continuous energy profile as predicted by (semi-)local DFT functionals. The blue curves corresponds to the difference of the latter two, and illustrates the magnitude the required Hubbard correction for a single-electron system.

potential caused by the Hubbard correction can be calculated as[124,127,128]

$$\Delta V = \sum_{I, m} U^I \left(\frac{1}{2} - n_m^{I\sigma} \right) \left| \varphi_m^I \right\rangle \left\langle \varphi_m^I \right|. \tag{3.42}$$

This term thus becomes repulsive, if the occupation of the orbitals is lower $1/2$, and attractive, if the occupation is higher $1/2$. This clearly promotes the localization of states by preventing a fractional occupation of localized orbitals.

In 2005, Cococcioni and de Gironcoli[135] presented a simplified scheme to include the DFT+U formalism. Their version features an effective U parameter, does not depend on the basis set and allows for the self-consistent determination of the U parameters, too. Since we will use their scheme to include the Hubbard correction in our calculations (see Chaps. 5, 7 and 8), this methodology shall now be described in more detail. The discussion thereby follows Ref. 135.

First of all, the form of the occupation matrices $n_{mm'}^{I\sigma}$, allowing for a physically accurate description of the system under consideration, has to be defined. There is a number of interchangeable choices for $n_{mm'}^{I\sigma}$, but they can all be summarized with the general form

$$n_{mm'}^{I\sigma} = \sum_{k,\nu} f_{k\nu}^{\sigma} \left\langle \psi_{k\nu}^{\sigma} \right| P_{mm'}^{I} \left| \psi_{k\nu}^{\sigma} \right\rangle. \tag{3.43}$$

Here, $\psi_{k\nu}^{\sigma}$ indicates the electronic wave function of the state $(k\nu)$ and $f_{k\nu}^{\sigma}$ the corresponding occupation number. The operators $P_{mm'}^{I}$, on the other hand, correspond to generalized projectors on the localized-electron manifold. The projection operators fulfill the following properties:

$$\sum_{m'} P^I_{mm'} P^I_{m'm''} = P^I_{mm''}$$

$$P^I_{mm'} = (P^I_{m'm})^\dagger$$

$$P^I_{mm'} P^I_{m''m'''} = 0 \quad \text{for} \quad m' \neq m''.$$

The projector of the entire manifold of localized states of the atom at the site I is given by $P^I = \sum_m P^I_{mm}$. Thus, the total localized-states occupation for the atom I is given as

$$n_I = \sum_\sigma \sum_{\mathbf{k},\nu} f^\sigma_{\mathbf{k}\nu} \langle \psi^\sigma_{\mathbf{k}\nu} | P^I | \psi^\sigma_{\mathbf{k}\nu} \rangle = \sum_{\sigma,m} n^{I\sigma}_{mm}. \tag{3.44}$$

Note that projectors on different sites are not assumed to be orthogonal. In their work, Cococcioni and de Gironcoli used the definition

$$P^I_{mm'} = \left| \varphi^I_m \right\rangle \left\langle \varphi^I_{m'} \right| \tag{3.45}$$

which corresponds to a projection of localized states on pseudo-wave-functions, with the valence atomic orbital φ^I_m of the atom I with angular momentum $|lm\rangle$.

The simplification by Cococcioni and de Gironcoli consists in neglecting higher, multipolar terms in the Coulomb interaction and the proper description of magnetic interactions, thereby considering mainly the effects which can be attributed to the on-site Coulomb repulsion. Consequently to the neglection of these multipolar terms, the term J can be set to zero, or rather the Hubbard parameter can be redefined by introducing an effective $U_{\text{eff}} = U - J$ to account for the effects of multipolar terms. With this simplification, the energy correction reads[135]

$$E_U \left[\left\{ n^{I\sigma}_{mm'} \right\} \right] = E_{\text{Hub}} \left[\left\{ n^I_{mm'} \right\} \right] - E_{\text{dc}} \left[\left\{ n^I \right\} \right]$$

$$= \frac{U_{\text{eff}}}{2} \sum_I \sum_{m,\sigma} \left\{ n^{I\sigma}_{mm} - \sum_{m'} n^{I\sigma}_{mm'} n^{I\sigma}_{m'm} \right\}$$

$$= \frac{U_{\text{eff}}}{2} \sum_{I,\sigma} \text{Tr} \left[\mathbf{n}^{I\sigma}(1 - \mathbf{n}^{I\sigma}) \right]$$

$$= \frac{U}{2} \sum_{I,\sigma} \sum_i \lambda^{I\sigma}_i (1 - \lambda^{I\sigma}_i). \tag{3.46}$$

In the last step, U_{eff} was set to U and the representation diagonalizing the occupation matrices of localized orbitals (i.e., $\mathbf{n}^{I\sigma} \mathbf{v}^{I\sigma}_i = \lambda^{I\sigma}_i \mathbf{v}^{I\sigma}_i$, with $0 \leq \lambda^{I\sigma}_i \leq 1$) was chosen. In addition, the following definition has been applied for the double-counting term[135]

$$E_{\text{dc}} = \sum_I \frac{U}{2} n^I \left(n^I - 1 \right) - \sum_I \frac{J}{2} \left[n^{I\sigma} \left(n^{I\sigma} - 1 \right) + n^{I-\sigma} \left(n^{I-\sigma} - 1 \right) \right]. \tag{3.47}$$

Eq. 3.46 clearly shows that the Hubbard correction does not correct the energies of completely empty or filled orbitals (e.g., $\lambda = 0$ or $\lambda = 1$, respectively). This behavior is crucial to illustrate the effects during the description of localized states of the Hubbard correction. In fact, the total energy of an open atomic system in contact with a reservoir of electrons is represented

by a piecewise linear curve, whose vertices correspond to the energies assumed for an integer occupation, also see Fig. 3.3. The exact multiparticle framework does reproduce this behavior, but under the application of LDA or GGA functionals, unphysical energy values for fractional occupations are predicted. These are caused by nonlinear energy contributions induced by the self-interaction of partially occupied Kohn-Sham orbitals. Nevertheless, the differences of total energies assumed for an integer occupation calculated within LDA and GGA are pretty accurate so that the exact shape of the energy curve can be restored by an energy correction added only on states with fractional occupation as the one in Eq. 3.46 does.

3.5.1 Self-consistent calculation of the Hubbard U

For a single electron-system, the magnitude for the U can be directly derived from the difference between the real and the DFT total energy, also see Fig. 3.3. For more complex systems, the determination of U is more complicated. Sometimes, the U parameter is simply tuned to reproduce, e. g., experimental or GW band-gap widths[136–138] or intercalation potentials[33]. However, since the U parameter does not only depend on the chemical environment of the atoms on which the correction is applied, but also on the chosen functionals, an accurate determination of its value is crucial for the achievement of meaningful results. Nevertheless, Cococcioni and de Gironcoli[135] also present a method for the self-consistent determination of the U energy correction for the system under consideration. We will follow their discussion to briefly elaborate on this method.

For the calculation the U parameter, the total energy of the system with interacting particles in dependence of the localized-level occupation $\{q_I\}$ has to be determined as

$$E[\{q_I\}] = \min_{n(\mathbf{r}),\alpha_I} \left\{ E[n(\mathbf{r})] + \sum_I \alpha_I(n_I - q_I) \right\} \tag{3.48}$$

with n_I as defined in Eq. 3.44 and α_I as the Lagrange multipliers. Then, an analogous calculation has to be performed to determine the total energy of the corresponding non-interacting Kohn-Sham problem:

$$E^{\mathrm{KS}}[\{q_I\}] = \min_{n(\mathbf{r}),\alpha_I} \left\{ E^{\mathrm{KS}}[n(\mathbf{r})] + \sum_I \alpha_I^{\mathrm{KS}}(n_I - q_I) \right\}. \tag{3.49}$$

The value of U then follows from the difference in curvatures of both energy functions as

$$U = \frac{\partial^2 E[\{q_I\}]}{\partial q_I^2} - \frac{\partial^2 E^{KS}[\{q_I\}]}{\partial q_I^2}. \tag{3.50}$$

In fact, the curvature of the first energy $E[\{q_I\}]$ alone does not correspond to the Hubbard U, since it is not purely caused by the energy needed to localize an electron in a specific site: Some contributions can be attributed to re-hybridization, arising from the band structure of the non-interacting system. Thereby Janak's theorem[139] can be used to calculate the curvatures as

$$\frac{\partial E[\{q_J\}]}{\partial q_I} = -\alpha_I, \quad \frac{\partial^2 E[\{q_J\}]}{\partial q_I^2} = -\frac{\partial \alpha_I}{\partial q_I}$$

$$\frac{\partial E^{\text{KS}}[\{q_J\}]}{\partial q_I} = -\alpha_I^{\text{KS}}, \quad \frac{\partial^2 E^{\text{KS}}[\{q_J\}]}{\partial q_I^2} = -\frac{\partial \alpha_I^{\text{KS}}}{\partial q_I}. \tag{3.51}$$

Although this procedure seems to be straight-forward, in real calculations one would rather prefer a representation, where the α_I are the independent variables. This is possible via a Legendre transform, leading to the expressions

$$E[\{\alpha_I\}] = \min_{n(\mathbf{r})} \left\{ E[n(\mathbf{r})] + \sum_I \alpha_I n_I \right\}$$

$$E^{\text{KS}}[\{\alpha_I\}] = \min_{n(\mathbf{r})} \left\{ E^{KS}[n(\mathbf{r})] + \sum_I \alpha_I^{\text{KS}} n_I \right\}. \tag{3.52}$$

Notably, the effect of the α_I is to shift the localized levels of the atom at the site I by adding a potential term $\Delta V = \sum_I \alpha_I P^I$ to the single particle potential.

Finally, using the relations in Eq. 3.51, the formula for the calculation of the Hubbard U reads

$$U = +\frac{\partial \alpha_I^{KS}}{\partial q_I} - \frac{\partial \alpha_I}{\partial q_I} = \left(\chi_0^{-1} - \chi^{-1} \right)_{II}, \tag{3.53}$$

where $\chi_{IJ}^{(0)}$ indicate the density response functions defined as

$$\chi_{IJ} = \frac{\partial^2 E}{\partial \alpha_I \partial \alpha_J} = \frac{\partial n_I}{\partial \alpha_J}$$

$$\chi_{IJ}^0 = \frac{\partial^2 E^{\text{KS}}}{\partial \alpha_I^{\text{KS}} \partial \alpha_J^{\text{KS}}} = \frac{\partial n_I}{\partial \alpha_J^{\text{KS}}}$$

To compute the magnitude of the $\chi_{IJ}^{(0)}$ numerically, a small positive and a small negative potential shift has to be added on each nonequivalent lattice site, on which the Hubbard correction shall be applied. Then, the variation of the occupations of all these sites has to be computed both by allowing for a self-consistent readjustment of the Kohn-Sham potential to screen this localized perturbation $\Delta V = \alpha_J P_J$ (J indicates the lattice site) and without the screening. The derivatives of the so-calculated occupations correspond to the matrices χ_{IJ} and χ_{IJ}^0.

3.6 Hybrid Functionals: Larger Band Gaps and Localized States

The idea behind hybrid functionals is to combine the exact treatment of the exchange contributions from Hartree-Fock theory (EXX) with (semi-)local DFT functionals to take advantage from error compensation and achieve realistic band gaps. In fact, in the framework of Hartree-Fock theory, excitation energies (and thus band-gap widths) are drastically overestimated, since the unscreened exchange does decay very slowly. On the other hand, DFT band gaps are always underestimated, so their combination is expected to yield intermediate and, therefore, more

realistic fundamental band gaps.[113]

Some early attemps tried to enhance the reliability of chemical properties calculated via local LSDA[9] functionals by combining the full exact exchange[10] E_X^{exact} with the LSDA correlation energy E_C^{LSDA}. The exchange-correlation functional thus reads[140]

$$E_{XC} = E_X^{exact} + E_C^{LSDA}. \tag{3.54}$$

This approach seems reasonable at first glance, since the exchange has certainly a greater impact than the correlation part of the XC. Unfortunately, it does not yield a satisfactory chemical accuracy. The origin of this problem is that the separate treatment of the exchange and the correlation effects via two different theories is deprived from the physical meaning of the exchange-correlation functional. More precisely, although Hartree-Fock theory provides a mathematically exact representation of the exchange, it does not account for the correlation component and the correlation from LSDA can not fully correct the missing interactions.[140]

Becke[140] showed that the limitation deriving from the combination of the EXX with the LDSA correlation can be overcome introducing the "half-and-half" theory. For this, he showed that E_{XC} can also be expressed in terms of the average potential of the fully non-interacting and the fully interacting system. The former corresponds to the exact exchange as calculated within the Kohn-Sham framework. The latter can be approximated with the LSDA exchange-correlation energy, leading to the expression[140]

$$E_{XC} \approx \frac{1}{2}E_X^{exact} + \frac{1}{2}E_{XC}^{LSDA}. \tag{3.55}$$

In the same paper, Becke suggested that Eq. 3.55 can be generalized as

$$E_{XC} \approx c_0 E_X^{exact} + c_1 E_{XC}^{LSDA}, \tag{3.56}$$

where the coefficients c_0 and c_1 can be derived by tailoring calculations to experimental data.

The model by Becke has since then been amplified and refined, and more and more hybrid functionals have been introduced. Examples of well established functionals are, e. g., the Heyd-Scuseria-Ernzerhof (HSE)[141, 142], the PBE0[143, 144] or the Becke-3-parameter-Lee-Yang-Parr (B3LYP)[145–147] functionals.

In this work, we will utilize the PBE0[143, 144] functional, which features the full PBE correlation, but replaces a fraction α[11] of its exchange with the EXX leading to

$$E_{XC}^{PBE0} = \alpha E_X^{exact} + (1 - \alpha)E_X^{PBE} + E_C^{PBE}. \tag{3.57}$$

By further tuning the fraction of EXX in Chap. 7, we aim at partially compensating for quasiparticle and excitonic effects, in order to overcome the band-gap problem and compute realistic absorption properties of defect geometries previously determined using the PBEsol+U formalism.

---

[9]Within the LSDA, the number of spin-up electrons can differ from that of spin-down electrons.

[10]Within the DFT framework, the term "exact exchange" is more appropriate compared to Hartree-Fock, because it corresponds to the exchange as calculated from the Slater determinant of the Kohn-Sham instead of the Hartree-Fock orbitals.[140]

[11]In its original formulation, the value $\alpha = 25\%$ (determined via perturbation theory) was suggested.[143] This shall be denoted as "standard PBE0" in the following chapters.

4

Alkali-Ion Batteries

$\mathbf{T}$HE development of renewable forms of energy is strictly connected with the quest for efficient energy storage. In this context, alkali-ion batteries, in particular, lithium-ion batteries (LIBs), are already well-established in electronic devices. They not only combine great energy densities with low self-discharge rates, but also feature good charging efficiencies with long lifetimes. This is, in fact, basically restricted only by the number of charging cycles.[148–150] Nevertheless, under special conditions and treatments, these batteries can be charged several thousands of times without any serious deterioration of their properties.[151,152]

However, current lithium-based technologies are not suitable for the large scale especially due to the low lithium (Li) in Earth's crust[153,154]. Moreover, new electrode materials could empower the development new technologies, for example of flexible devices[155].

Therefore, the suitability of new electrodes based on other largely available, inexpensive and non-toxic elements has to be investigated. Since all alkali metals show similar properties, sodium-ion (Na-ion, NIBs) and potassium-ion (K-ion, KIBs) based electrodes, but also multivalent ions such as Mg or Ca could be promising alternatives for LIBs.[152,154,156–162]

Unfortunately, due to larger ionic radii, the electrodes currently used for Li-ion technologies have to be substituted. For this reason, finding new electrode materials is unavoidable. Since the synthesis of new electrode materials can be rather expensive, the suitability of a material for electrochemical applications should be theoretically tested beforehand, using, e. g., DFT.

In this Chapter, we will first introduce alkali-ion batteries by describing their setup. Then, in Sec. 4.2, we aim at illustrating the theoretical prediction of electrochemical properties via DFT routines.

4.1 Setup

An alkali-ion battery is a device which allows for energy storage by reversible chemical processes, accompanied by ion (de)intercalation mechanisms[1]. In order to build an alkali-ion battery, five key elements are required: Two electrodes, an electrolyte, a separator and an external

---

[1]In electrochemistry, ion intercalation and ion deintercalation in/from a material refer to the ion in-diffusion and out-diffusion, respectively. The former thus corresponds to the creation of interstitials, the latter to the formation of vacancies.

circuit. A schematic representation of an alkali-ion battery is shown in Fig. 4.1. The electrodes are the host of the mobile ions. During the charging of the battery, an external voltage has to be applied to the system, in order to deintercalate ions out of the positive electrode, transport them within the electrolyte and through the separator to the negative electrode, where they are finally intercalated. During the discharge, the ions migrate spontaneously from the negative to the positive electrode due an internal potential difference. The separator is thereby required to prevent a short-circuit of the electrodes by allowing only the positively charged ions to transit from one electrode to the other. The electrons, on the other hand, are conducted from one electrode to the other through the external circuit.[14]

During the charging of the battery, the deintercalation of the alkali ions in conjunction with the extracted electrons causes the oxidation of one component in the cathode. In the anode, on the contrary, one component is reduced upon the intercalation process. The redox reactions during the discharge are reversed. As a consequence, the positive and the negative electrode should be referred to as cathode and anode, respectively, during charging. During the discharge, on the other hand, the nomenclature should be reversed. However, for the sake of simplicity, in the following, we will adopt the convention to denote the positive electrode with cathode and the negative with anode.

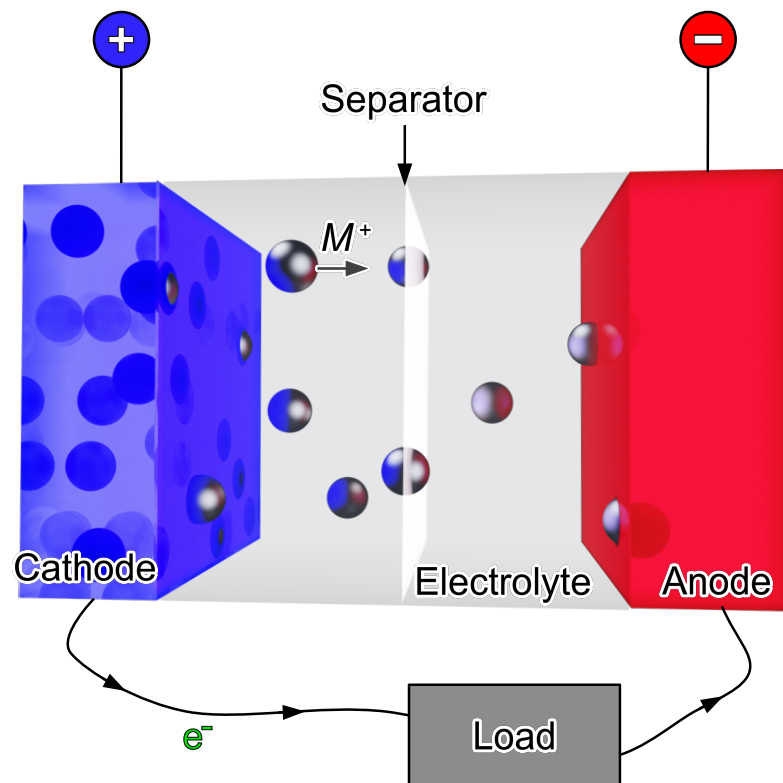To guarantee high average working voltages, materials with a high redox potential (e.g.,

Figure 4.1: Schematic representation of the charging process of an alkali-ion battery. An external voltage causes the deintercalation of the alkali ions out of the positive electrode (cathode). These are then transported trough the electrolyte and the separator to the negative electrode (anode), where the ions intercalate. The electrons, on the other hand, are conducted through an external circuit.

transition metal oxides[163]) are usually used as the cathode, while materials with a rather low potential (e. g., graphite[164] or alloys[165]) are adopted for the anode. The electrolyte, on the other hand, is usually composed of an organic solvent in which a salt (for example LiPF$_6$[166]) is dissolved. In addition to the liquid solutions, also specific superionic conductors can be used to build solid-state batteries.[167,168]

Together with high average voltages, batteries should also feature broad working temperature ranges, a robust long-term operation, be save and ideally not be costly during their production. In addition, also high gravimetric and volumetric energy densities are desirable.[14,15,152] Thereby, the gravimetric (volumetric) energy density is a measure for the number of electrons which can be stored per mass (volume).

4.2 Theoretical Investigation of Electrochemical Properties

When it comes to the design of new electrodes, it is often convenient to test their suitability by characterizing them theoretically. Many (electrochemical) properties can, in fact, be calculated within the DFT framework at a moderate computational cost. In the following, some techniques for the theoretical prediction of these properties shall be elaborated, thereby we will use M^+ to generally indicate the alkali cation, on which the alkali-ion battery is based. The discussion follows Ref. 15.

One property of an alkali-ion battery, which can be easily predicted, is the so-called open-circuit voltage (OCV). This quantity describes the ideal voltage of the entire battery in thermodynamic equilibrium. The thermodynamic equilibrium thereby corresponds to a minimum of the total Gibbs free energy, which depends implicitly on the temperature T, the pressure p, as well as on the number of atoms of other species.

If the electrode/electrolyte interfaces are relatively small, the contributions of the surfaces and interfaces can be neglected. So, the total Gibbs free energy may then be written as the sum of the Gibbs free energy in the anode (A), cathode (C) and electrolyte (E), yielding[15]

$$G^{\text{tot}}(N_{M^+}^A, N_{M^+}^C, N_{M^+}^E, N_{e^-}^A, N_{e^-}^C) = G^A(N_{M^+}^A, N_{e^-}^A) + G^C(N_{M^+}^C, N_{e^-}^C) + G^E(N_{M^+}^E). \quad (4.1)$$

In Eq. 4.1, the internal degrees of freedom are represented by the number of alkali ions in the battery's components (i. e., $N_{M^+}^A$, $N_{M^+}^C$, and $N_{M^+}^E$ in the anode, cathode, and electrolyte, respectively), and that of the valence electrons in anode and cathode (i. e., $N_{e^-}^A$, and $N_{e^-}^C$, respectively). Note that the electrolyte should not contain any electrons.

The change of the free energy of a system α after the intercalation of an ion M^+ is expressed by its electrochemical potential $\eta_{M^+}^\alpha$. It can be calculated via the partial derivative[15]

$$\eta_{M^+}^\alpha = \frac{\partial G^\alpha}{\partial N_{M^+}^\alpha}, \quad (4.2)$$

where G^α indicates the Gibbs free energy of the component α of a battery. The electrochemical potential of an electron $\eta_{e^-}^\alpha$ can be calculated in a similar way.

Under the condition $dN_M^\alpha = dN_{M^+}^\alpha = dN_{e^-}^\alpha$ (which means that the number of neutral atoms is equal to the number of ions and electrons), the electrochemical potentials of ions and

electrons can be used to calculate the chemical potential μ_M^α of the neutral atom M as[15]

$$\mu_M^\alpha = \frac{\partial G^\alpha}{\partial N_M^\alpha} = \frac{\partial G^\alpha}{\partial N_{M^+}^\alpha}\frac{\partial N_{M^+}^\alpha}{\partial N_M^\alpha} + \frac{\partial G^\alpha}{\partial N_{e^-}^\alpha}\frac{\partial N_{e^-}^\alpha}{\partial N_M^\alpha} = \eta_{M^+}^\alpha + \eta_{e^-}^\alpha, \tag{4.3}$$

which describes the free-energy change after the intercalation of one neutral atom M.

For the equilibrium state, the free energy of the battery has to be minimized with respect to the redistribution of the M^+ ions in the components of the battery. This redistribution of ions, however, should not affect the overall number of ions N_{M^+} in the battery. Therefore, N_{M^+} can be considered as constant, i. e., $N_{M^+} = N_{M^+}^A + N_{M^+}^C + N_{M^+}^E$, and the independent variables are reduced to two, e. g., $N_{M^+}^C$ and $N_{M^+}^E$.

With this, it can be shown that the electrochemical potential of the alkali ion M^+ is the same in every component of the battery, i. e., $\eta_{M^+}^A = \eta_{M^+}^C = \eta_{M^+}^E$. Therefore, the partial derivatives of the total free energy with respect to $N_{M^+}^C$ and $N_{M^+}^E$ must equal zero, yielding[15]

$$\left(\frac{\partial G}{\partial N_{M^+}^C}\right)_{N_{M^+}^E} = \left(\frac{\partial G^C}{\partial N_{M^+}^C} + \frac{\partial G^A}{\partial N_{M^+}^C} + \frac{\partial G^E}{\partial N_{M^+}^C}\right)_{N_{M^+}^E}$$

$$= \frac{\partial G^C}{\partial N_{M^+}^C} + \frac{\partial G^A}{\partial N_{M^+}^A}\left(\frac{\partial N_{M^+}^A}{\partial N_{M^+}^C}\right) = \eta_{M^+}^C - \eta_{M^+}^A = 0 \tag{4.4}$$

and

$$\left(\frac{\partial G}{\partial N_{M^+}^E}\right)_{N_{M^+}^C} = \left(\frac{\partial G^C}{\partial N_{M^+}^E} + \frac{\partial G^A}{\partial N_{M^+}^E} + \frac{\partial G^E}{\partial N_{M^+}^E}\right)_{N_{M^+}^E}$$

$$= \frac{\partial G^E}{\partial N_{M^+}^E} + \frac{\partial G^A}{\partial N_{M^+}^A}\left(\frac{\partial N_{M^+}^A}{\partial N_{M^+}^E}\right) = \eta_{M^+}^E - \eta_{M^+}^A = 0. \tag{4.5}$$

The relations derived in Eqs. 4.3 and 4.4 bring us to the formulation of the Nernst equation, which can be applied to calculate the voltage V of a battery via its intrinsic thermodynamic parameters. In a more general formulation also accounting for multivalent ions M^z ($z > +1$), the Nernst equation reads[15]

$$V = -\frac{\eta_{e^-}^C - \eta_{e^-}^A}{ze_0} = -\frac{\mu_M^C - \mu_M^A}{ze_0}, \tag{4.6}$$

with e_0 as the elementar charge. Note that, since z indicates the oxidation number of the ion, it also corresponds to the fraction of transferred charge per (de)intercalated ion.

Instead of calculating V, however, usually the voltage is averaged over a full charge/discharge cycle. For this, Eq. 4.6 has to be integrated between the fully (de)intercalated electrode and the pristine electrode material.[169]

The average voltage $\overline{V}$ of a cathode (anode) with respect to an anode (cathode) of the transferred element in its metallic phase[2] can be calculated using DFT routines, via[15,169–174]

$$\overline{V} = \pm\frac{\Delta G}{zF}, \tag{4.7}$$

where ΔG is the change of the Gibbs free energy caused by the alkali-ion (de)intercalation

---

[2]This quantity is also referred to as half-cell redox potential.

and $F = e_0 N_A = 96485.309\,\mathrm{C\,mol^{-1}}$ is the Faraday constant. Here, N_A denotes the Avogadro constant. The change in Gibbs free energy has to be related to the specific direction of the reactions. This is achieved by the positive and negative sign, which refer to the cathode and anode, respectively.

The change in Gibbs free energy corresponds to $\Delta G = \Delta E + p\Delta V - T\Delta S$, where ΔE is the change in internal energy, p the pressure, T the temperature and ΔS the change in entropy. Within the (standard) DFT framework, the temperature is fixed to $T = 0\,\mathrm{K}$, so the term $T\Delta S$ equals zero. In addition, if also volume effects are neglected, i. e., $p\Delta V = 0$, the change of the Gibbs free energy can be approximated by the change of the internal energy ΔE. Thus Eq. 4.7 reads[15,169–174]

$$\overline{V} \approx \pm\frac{\Delta E}{zF}, \tag{4.8}$$

where the quantity ΔE can be derived from the ground-state energies of the structures with different alkali-ion concentrations.

In the case of monovalent ions, the fraction of transferred charge z can be expressed as $z = xe_0$ with x as the concentration of (de)intercalated M per formula unit of the electrode material. With this, Eq. 4.8 reads

$$\overline{V} \approx \pm\frac{\Delta E}{zF} = \pm\frac{\Delta E}{xe_0F} = \pm\frac{E_{(\mathrm{de})\mathrm{in}}}{e_0F}. \tag{4.9}$$

where $\Delta E_{(\mathrm{de})\mathrm{in}}$ denotes the (de)intercalation energy of the alkali atoms. The (de)intercalation energy thereby describes how much energy is released or has to be applied to the system in order to (de)intercalate a neutral atom in (from) the host. It can be calculated as[28,175]

$$E_{\mathrm{dein}} = \frac{E - E_{\mathrm{host}} + x \cdot E_M}{x} \tag{4.10}$$

$$\text{and} \qquad E_{\mathrm{in}} = \frac{E - E_{\mathrm{host}} - x \cdot E_M}{x}, \tag{4.11}$$

with E_M as the chemical potential of the element M, while E_{host} and E denote the ground-state energy per formula unit of the stoichiometric host and of the material after the (de)intercalation of M, respectively.

Unfortunately, however, the self-interaction error, which is not corrected by (semi-)local exchange-correlation functionals (i. e., LDA and GGA), also affects the calculation of redox potentials. In fact, these functionals commonly underestimate redox potentials. To achieve a more accurate description, hybrid functionals or the Hubbard correction (see Secs. 3.6 and 3.5, respectively) can be applied for the calculation of intercalation voltages and anionic oxidation.[176–181]

In addition, when more defect concentrations x have been computed, it is helpful to construct the so-called convex hull, allowing for the determination of thermodynamically stable phases. Thereby, the formation energy E_f[182]

$$E_f = E - (1 - x) \cdot E_{\mathrm{host}} - x \cdot E_{\mathrm{host}-M} \tag{4.12}$$

is plotted against the concentration x.[3]

---

[3] Note that this formation energy refers to the formation energy of the vacancies in the cathode.
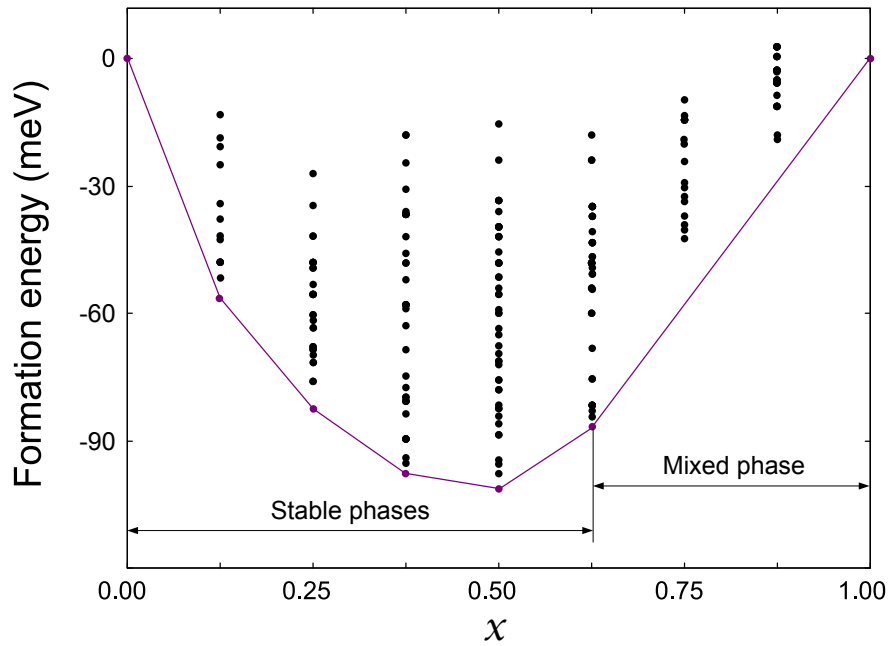
Figure 4.2: Convex-hull construction of an exemplary cathode material. The concentration x indicates the concentration of deintercalated alkali atoms per formula unit. Stable phases are predicted for $0.000 \leq x \leq 0.625$. For $0.625 < x < 1.000$ a mixed phase (composed of areas with $x = 0.625$ and $x = 1.000$) is expected.

Then, to build the convex hull, the lowest-energy ordered phases have to be connected via straight lines. Only the defect concentrations which intersect the convex hull are predicted to be stable. Otherwise, the phase is expected to be unstable with respect to a mixed phase consisting of the start and the end point of the underneath-lying line.[182] A schematic representation of an exemplary convex-hull construction is depicted in Fig. 4.2.

Apart from average voltages, DFT geometry optimization can also be used to quantify volume deformations upon alkali-ion (de)intercalation. Suitable electrode materials, in fact, should not suffer from strong volume expansion (shrinkage) upon ion (de)intercalation to avoid the battery from breaking.

Furthermore, the theoretical gravimetric capacity C[4], can be determined from the number of alkali ions (de)intercalated per formula unit and the total molar mass m_x of the host after the (de)intercalation[15,29]

$$C = \frac{xF}{m_x}. \tag{4.13}$$

Likewise, the volumetric capacity C_v corresponds to how much charge can be extracted or stored per unit volume. From this, the gravimetric (volumetric) energy density corresponds to $\rho_{(\mathrm{v})} = \overline{V}\, C_{(\mathrm{v})}$[15].

Finally, nudged-elastic band (NEB)[183] calculations can be performed to investigate the ion-migration (vacancy-migration) mechanisms in the cell. The NEB method allows for the calculation of energy barriers for the migration of an ion (or a vacancy) in a material. For the

---

[4]The gravimetric (volumetric) capacity expresses how much charge can be extracted or stored per unit weight (volume).

calculation, the minimum energy path has to be computed by minimizing the energy of the so-called intermediate images along the path connecting the starting and the final position of the ion (vacancy). Thereby, the spacing between neighboring images is kept constant. During the optimization, the norm of the force component perpendicular to the path is minimized until it is lower than a preset threshold. At the end, the energy barriers are calculated as the difference between the lowest and the highest energy values along each segment.

5

Electrochemical Properties of KTA

TECHNOLOGIES based on heavier alkali ions are expected to be promising substitutes for Li-ion batteries. However, due to the larger ionic radii, the investigation of new electrode materials is essential. The requirements for new electrodes are stringent: They should not only provide a high operation voltage, but also have to guarantee high capacities, a long-lasting and robust operation as well as efficient charging mechanisms.

In this context, a number of studies indicate KTP-type crystals as excellent cathode and anode materials for alkali-ion batteries.[28–39] These crystals, in fact, are characterized by a high ionic conductivity, which on the one hand hampers techniques requiring the application of external fields, e. g., periodic poling[27], but could be a benefit for battery applications, since it facilitates efficient (de)charging mechanisms.

In particular, KTP seems to be promising both for cathodes and anodes. Thereby, the deintercalation of K from the cathode material leads to the oxidation of Ti-Ti coordinated oxygen atoms[28]. In the anode material, on the other hand, the intercalation of alkali ions provokes the reduction of the Ti sites near the intercalation place[29].

As discussed in Chapter 2, reduced Ti atoms in the vicinity of oxygen vacancies are discussed to be instrumental for the characteristic gray tracking. These Ti^{3+} centers are not only thermally stable[54], but an electron is more prone to be trapped near an oxygen vacancy instead of far away from it[95]. Since the electronic flux could thus be hindered, this phenomenon may also indirectly impair the electrochemical performance of the material.

However, gray tracking does not affect the whole KTP family to the same extent[56,58]. It is therefore reasonable to study the suitability of further KTP isomorphs for battery applications[30–39]. KTA for example is more robust against gray tracking[58], and is applied in similar fields as KTP[26,27,85,184]. To ensure a sufficient high electrode conductivity caused by the large band gap[185], however, further material processing such as a electro-conducting carbon coating could be mandatory[29,186].

In this chapter, we will discuss the performance of KTA both as cathode and anode for potassium-ion batteries (KIBs) using density functional theory. The results have already been published and the discussion follows Ref. 187.

5.1 Computational Details

To investigate the electrochemical performance of KTA, we apply DFT as implemented in the open-source program Quantum ESPRESSO (QE)[188,189]. For the modeling of the electron-ion interaction, norm-conserving pseudopotentials, which treat the Ti $3d^2\,3s^2\,3p^6$, As $4s^2\,4p^3$, K $4s^1$, and O $2s^2\,2p^4$ states as valence states, are used. The remaining states are considered to be frozen in the core and to not participate in chemical bonding.

In addition, the electronic XC energy contributions are included using the generalized gradient approximation GGA via the PBEsol functional[111,112]. As mentioned in Chap. 4, the suitability of (semi-)local functionals for the prediction of electrochemical properties is to some extent limited, as these functionals typically underestimate redox voltages. A quantitatively better description of voltages can be achieved by the application of hybrid functionals[180]. Unfortunately, hybrid DFT is computationally very demanding. So, since plenty of complex structures have to be simulated in order to account for every defect geometry, its application would lead to non-affordable computational costs. In the literature, however, many studies indicate the Hubbard correction as a valid substitute for hybrid functionals, leading to realistic intercalation voltages and anionic oxidation[176–181] at a much lower computational cost as hybrid functionals. To include the Hubbard energy correction, we followed again the simplified version by Cococcioni and de Gironcoli[135], including an energy correction of $U = 5.8\,\mathrm{eV}$, which has been determined self-consistently (for details see Sec. 7.1). To evaluate the accuracy of the PBEsol+U methodology during the computation of the cathode material, we compare the voltages calculated using Eq. 4.9 for a KTA cell with one deintercalated potassium atom once under the application of the Hubbard correction and once under the application of hybrid PBE0[143,144]. Since the results agree within 0.3 V, we expect the Hubbard correction to lead to meaningful results. Beside a more reliable prediction of voltages, the Hubbard correction is also required to describe accurately the reduction of titanium atoms in the anode upon the intercalation of potassium atoms.

Atomic wave functions are expanded into plane waves up to an energy cutoff of 100 Ry. The Baldereschi point[190] is used for Brillouin-zone sampling. In addition, atomic positions and lattice parameters are optimized until fluctuations in energy and total forces are below $10^{-8}\,\mathrm{Ry}$ and $10^{-4}\,\mathrm{Ry/bohr}$, respectively.

This procedure yields values of $a = 13.412\,\text{Å}$, $b = 6.777\,\text{Å}$, and $c = 10.834\,\text{Å}$ for the lattice parameters of KTA, slightly overestimating the respective experimental values[64].

Finally, to study the potassium (de)intercalation mechanisms in KTA crystals, NEB[183] calculations are performed. The simulation is carried out until the norm of the force orthogonal to the migration path falls below 0.05 eV/Å. The remaining convergence criteria remain unchanged.

5.2 KTA Cathodes

5.2.1 Modeling of the Cathode Material

To simulate the charging of the battery, oxidizing defects have to be introduced in the cathode. In KTA, this can be achieved by the deintercalation of potassium atoms, which causes the oxidation of neighboring Ti-Ti coordinated oxygen atoms (O_{Ti-Ti}).

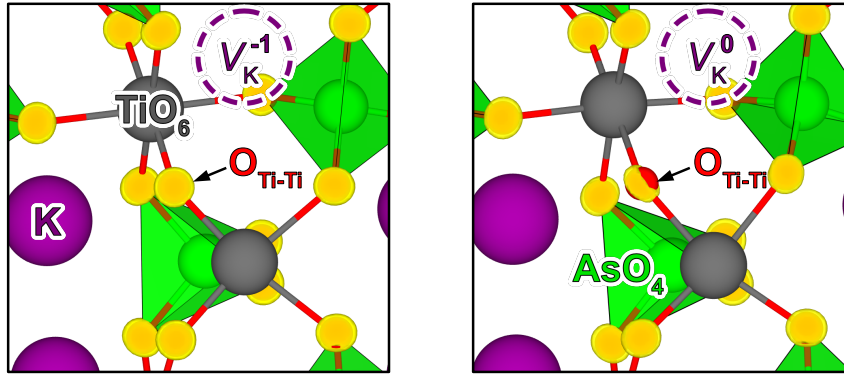**Figure 5.1:** (Adapted from Ref. 187) Schematic representation of the oxidation of one O_{Ti-Ti} atom near the K deintercalation site. The yellow isosurfaces indicate the electron charge density.

Using the KTA unit cell for the numerical simulation, up to eight potassium atoms can be deintercalated. This results in K-deficient $K_{1-x}TiOAsO_4$ with $x = 0.125\text{-}1.000$ as the concentration of deintercalated K per formula unit.

In the thermodynamic equilibrium, potassium vacancies are more likely to be found in the one-fold negatively charged state -1, since the deintercalation of a neutral potassium atom would generate a hole at the top of the valence band. As a matter of fact, a hole at the valence band maximum is rather unstable. So, the vacancy is energetically more favorable in the charge state -1. This means that per each removed K^+ ion, one valence electron remains in the cell. The retained electrons are thereby mainly stabilized by one O_{Ti-Ti} near the vacancy.

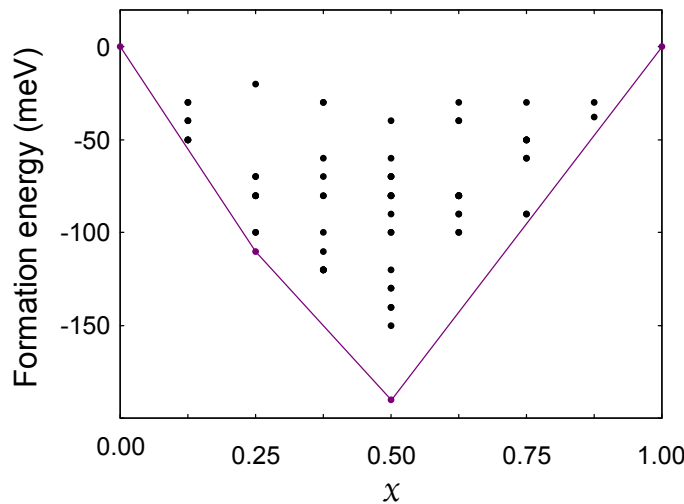For a correct charging of the KIB, beside the ion flux, however, also the electron has to transit

Figure 5.2: (Adapted from Ref. 187) Convex hull to determine, which vacancy concentrations x lead to stable phases. The concentrations $x = 0.000$, 0.250, 0.500, and 1.000 are expected to be stable with respect to the mono-phase. The phases with $x = 0.125$, 0.750, and 0.875 might be stabilized by entropy. A mixed phase is predicted at least for $0.25 < x < 0.50$ and $0.50 < x < 0.75$.

from one electrode. Thereby, the following reaction takes place

$$\mathrm{KTiOAsO_4} \longrightarrow \mathrm{K_{1-x}TiOAsO_4} + x\left(\mathrm{K^{+1}} + e^-\right). \tag{5.1}$$
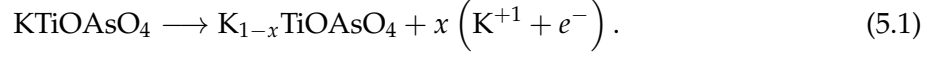
So, to achieve an accurate description of this oxidation, a two-step procedure is required. First, we optimize the energetically more stable charge state V_{K}^{-1}. Consequently, we also extract the excess electron from the cell and relax the structure again, obtaining the neutral V_{K}^{0}.

In addition, during the calculations, we set the total spin angular momentum to $S = \frac{n}{2}$, with $n = 1\text{-}8$ as the number of deintercalated potassium atoms. This is important to model quasi-non-interacting, isolated defects. As visible from the electron density depicted in Fig. 5.1, this method describes accurately the oxidation of the above mentioned oxygen atom.

To cover all possible defect configurations, in theory, the ground-state geometry of 256 vacancy combinations has to be determined. However, this number can be reduced if symmetry-equivalent configurations are grouped. To determine which defect concentrations are thermodynamically stable, we construct the convex hull as described in Sec. 4.2, by compiling the
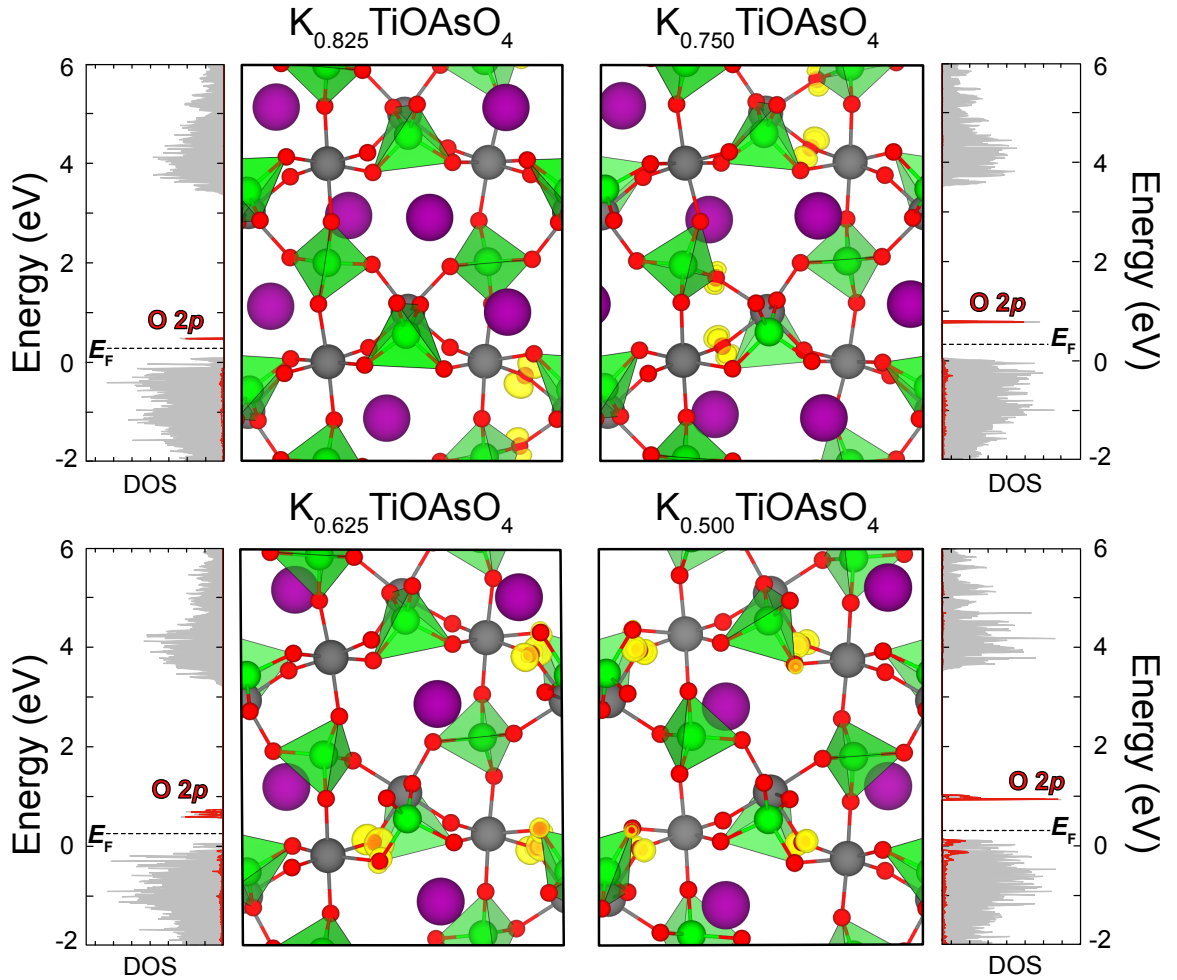

Figure 5.3: (Adapted from Ref. 187) Geometries of the most stable vacancy configurations in $\mathrm{K_{1-x}TiOAsO_4}$ with $0.125 \leq x \leq 0.500$. In addition, the electronic DOS as well as the electronic orbitals of mid-gap levels are shown. E_{F} indicates the Fermi level. For the concentrations $0.625 \leq x \leq 1.000$ see Fig. 5.4

formation energy E_f of each defect configuration calculated as

$$E_f = E_{\text{K}_{1-x}\text{TiOAsO}_4} - (1-x) \cdot E_{\text{KTiOAsO}_4} - x \cdot E_{\text{TiOAsO}_4} \tag{5.2}$$

against the concentration of deintercalated K per formula unit. In Eq. 5.2, $E_{\text{K}_{1-x}\text{TiOAsO}_4}$, E_{KTiOAsO_4} and E_{TiOAsO_4} refer to to the ground-state energy of one formula unit of $\text{K}_{1-x}\text{TiOAsO}_4$, KTiOAsO_4 and TiOAsO_4, respectively. The so-calculated values for E_f together with the corresponding convex hull (violet curve) are plotted in Fig. 5.2.

At zero temperature, only the vacancy concentrations $x = 0.00$, 0.25, 0.50, and 1.00 are predicted to lead to stable phases. Notably, the same vacancy concentrations have already been reported as stable phases also for KTP cathodes[28]. The defect structures of the remaining concentrations x are all located above the convex hull and, thus, predicted to be unstable with respect to a mixture of adjacent stable vacancy concentrations. However, at finite temperatures the phases with $x = 0.125$, 0.750, and 0.875 could be stabilized by entropy, since they are located less than 10 meV above the convex hull. For the defect concentrations $0.25 < x < 0.50$
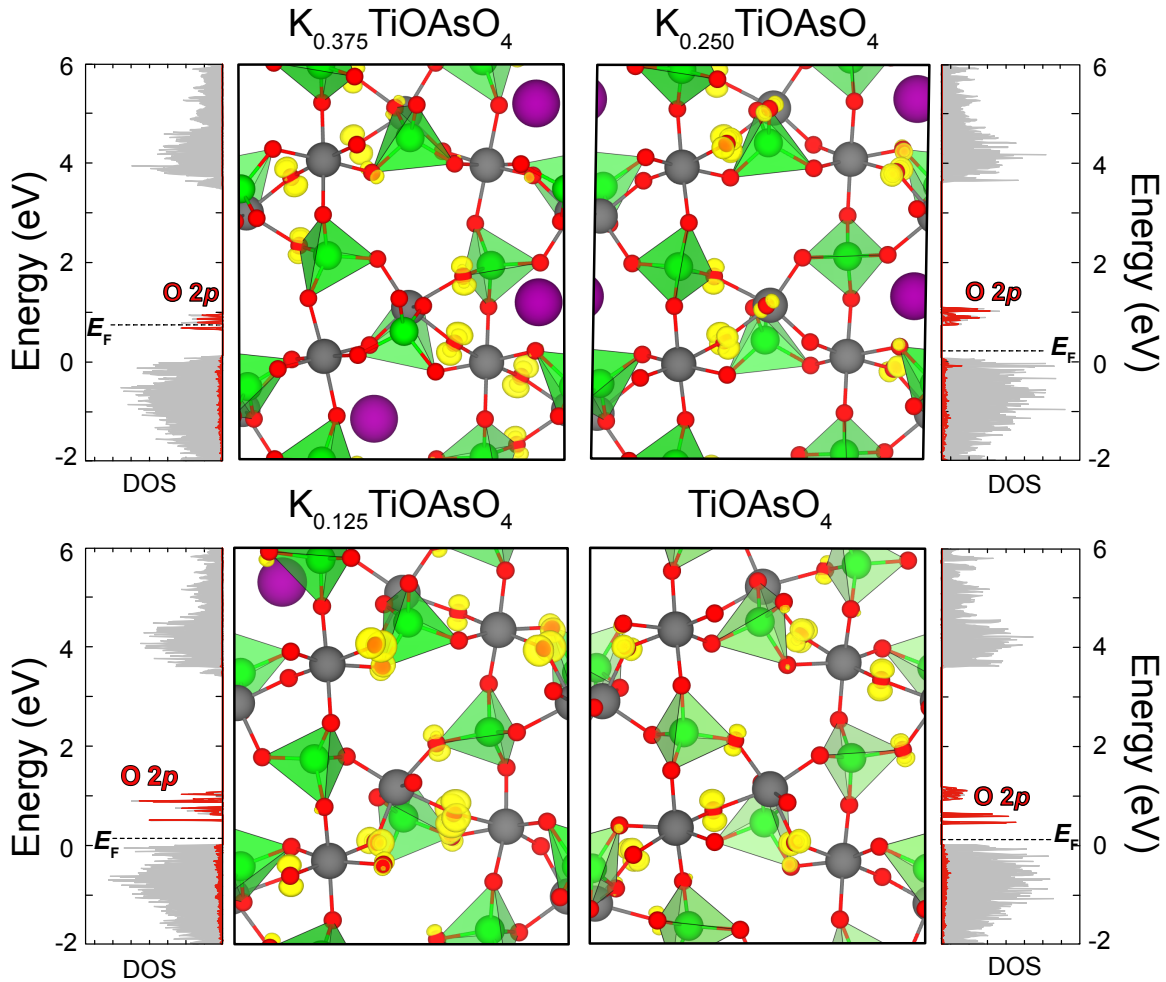

Figure 5.4: (Adapted from Ref. 187) Geometries of the most stable vacancy configurations in $\text{K}_{1-x}\text{TiOAsO}_4$ with $0.625 \leq x \leq 1.000$. In addition, the electronic DOS as well as the electronic orbitals of mid-gap levels are shown. E_F indicates the Fermi level. For the concentrations $0.125 \leq x \leq 0.500$ see Fig. 5.3
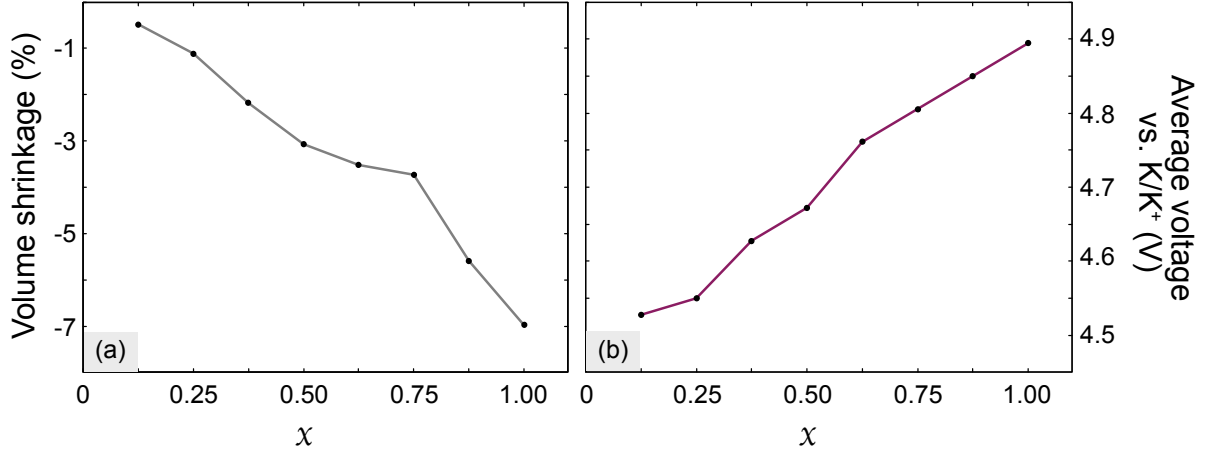
Figure 5.5: (Adapted from Ref. 187) (a) Volume reduction and (b) average voltages calculated for $K_{1-x}TiOAsO_4$ with $0.125 \leq x \leq 1.000$.

and $0.50 < x < 0.75$, on the other hand, the system is expected to undergo a phase separation.

The deintercalation of potassium from the KTA matrix does not have a strong influence on the overall appearance of the crystal structure, which is qualitatively preserved. In fact, as shown in Figs. 5.3 and 5.4, the most visible effect is a redistribution of the remaining K atoms in the cell. Note that only the energetically most favorable geometry for each vacancy concentration is depicted. The mesh of TiO_6 octahedra and AsO_4 tetrahedra, on the other hand, is only negligibly altered. Though, a slight deformation of the lattice angles is calculated and, as expected, the unit cell volume undergoes a rather small reduction. The highest shrinkage is predicted after the deintercalation of all the K atoms in the cell, i.e., $TiOAsO_4$, with a volume shrinkage of about 7% compared to stoichiometric KTA, see Fig. 5.5a. In KTP it was found that the deintercalation of all K atoms present in the cell results in a volume shrinkage of only 1.5%[28], so the KTP framework seems to be more robust compared to KTA. However, the volume shrinkage predicted here is slightly lower than that of another KTP isomorph, i.e., $KVPO_4F$, of about 7.8%[28]. So, the structural stability of KTA under the deintercalation of K should still be high enough to guarantee a stable long-term operation, especially for moderate x.

On the other hand, K vacancies affect the electronic density of states (DOS) of KTA crystals, see Figs. 5.3 and 5.4. The main impact of the deintercalation of K atoms is the formation of O $2p$ defect states within the band gap. For some vacancy configurations, these levels are completely empty, for others partially occupied. More precisely, the mid-gap states can be attributed to the two neighboring O_{Ti-Ti}. One of these corresponds to the oxidized O_{Ti-Ti} atom as shown in Fig. 5.1.

In order to deintercalate K atoms from the cell, energy has to be applied to the system. This corresponds to the charging of the battery. To quantify the amount of energy required for this procedure, we calculate the deintercalation energy E_{dein} for each simulated defect geometry x as described in Sec. 4.2, by adapting Eq. 4.10 to KTA. The so-obtained expression reads

$$E_{dein} = \frac{E_{K_{1-x}TiOAsO_4} - E_{KTiOAsO_4} + x \cdot E_K}{x}. \tag{5.3}$$

Here, $E_K = -0.82\,\text{Ry}$ is the chemical potential of metallic K[1].

According to Eq. 4.10, we obtain average deintercalation energies E_{dein} between 4.5 eV and 4.8 eV. These energies are of the same order of magnitude, but slightly larger than the corresponding values in KTP, which were found to vary between 4.2 eV and 4.6 eV[28].

Consequently, using Eq. 4.9, we calculate the resulting average voltage $\overline{V}$ for each concentration x. The so obtained $\overline{V}$ are compiled in Fig. 5.5b. As more K is deintercalated from the matrix, the average voltage increases. The same behavior holds also for KTP cathodes. However, the average voltages calculated here are slightly higher than the one in KTP, i. e., between 4.47 and 4.80 V vs. up to 4.59 V[28], respectively. An opposite trend is visible for the gravimetric capacity of the two materials. In fact, due to the higher molar mass of As compared to P, the gravimetric capacity of KTA can reach a maximum value of 132.17 mAhg^{-1}, while that of KTP[28] can reach up to 168.73 mAhg^{-1}, upon the deintercalation of all the K atoms from the cell. As a consequence, also the gravimetric energy density calculated for KTA is lower than that of KTP[28], i. e., 634.57 Wh/kg and 774.46 Wh/kg , respectively. Nevertheless, it is close to that of KVPO$_4$F (664.68 Wh/kg)[28] and in the same range of actual cathodes for Li-ion batteries (between about 500 and 1000 Wh/kg)[152].

5.2.2 Potassium-Vacancy Diffusion

Apart from outstanding electrochemical properties and stability, a good electrode material should also permit a fast vacancy (ion) diffusion to guarantee fast (de)charging mechanisms and to ease the ion (de)intercalation. To explore the migration mechanisms in KTA, we perform NEB calculations. In total, we consider six different pathways in the KTA unit cell, two are oriented along [100], the remaining four along [001], see Fig. 5.6. The activation energies of the vacancy migration along the [010] direction of the crystal were found to be rather unfavorable in the KTP family members[29,31,68] and, for this reason, these pathways are not considered here. Note that for the NEB calculations the start and end images have to feature the same lattice dimensions. However, the lattice constants of the defect cells do not match after volume relaxation. But considering that compared to the stoichiometric KTA unit cell, the change in volume is less that 0.5 %, it is reasonable to use defect geometries, which have only been relaxed with respect to the atomic positions while the lattice parameters are kept fixed at the values of stoichiometric KTA.

The so-calculated activation barriers are compiled in Fig. 5.6. Notably, the vacancy migration is locally facilitated when the vacancy is shifted from a K(1) to a K(2) site compared to the opposite direction. In addition, also the vacancy formation energy is more favorable if it is located at the site K(2). A possible explanation for this phenomenon can be found in the internal polarization of the crystal.

For each segment, the computed activation energies are found to be lower than 0.8 eV. Thereby, the most favorable pathway is characterized by activation energies lower than 370 meV, and corresponds to the anti-clockwise spiral pathway (e) along the c axis (i.e., K(2) $\longrightarrow$ K(5) $\longrightarrow$ K(6) $\longrightarrow$ K(1) $\longrightarrow$ K(2)), see Fig. 5.6. This reflects the experimental finding, that the ionic conductivity along the [001] direction is by far higher compared to those along [100] and [010][191].

---

[1]To calculate the chemical potential of elemental M, the energy of one M atom in the bulk material has to be determined. Here, we use the ground-state energy per atom of metallic K (bcc) to calculate the chemical potential K.
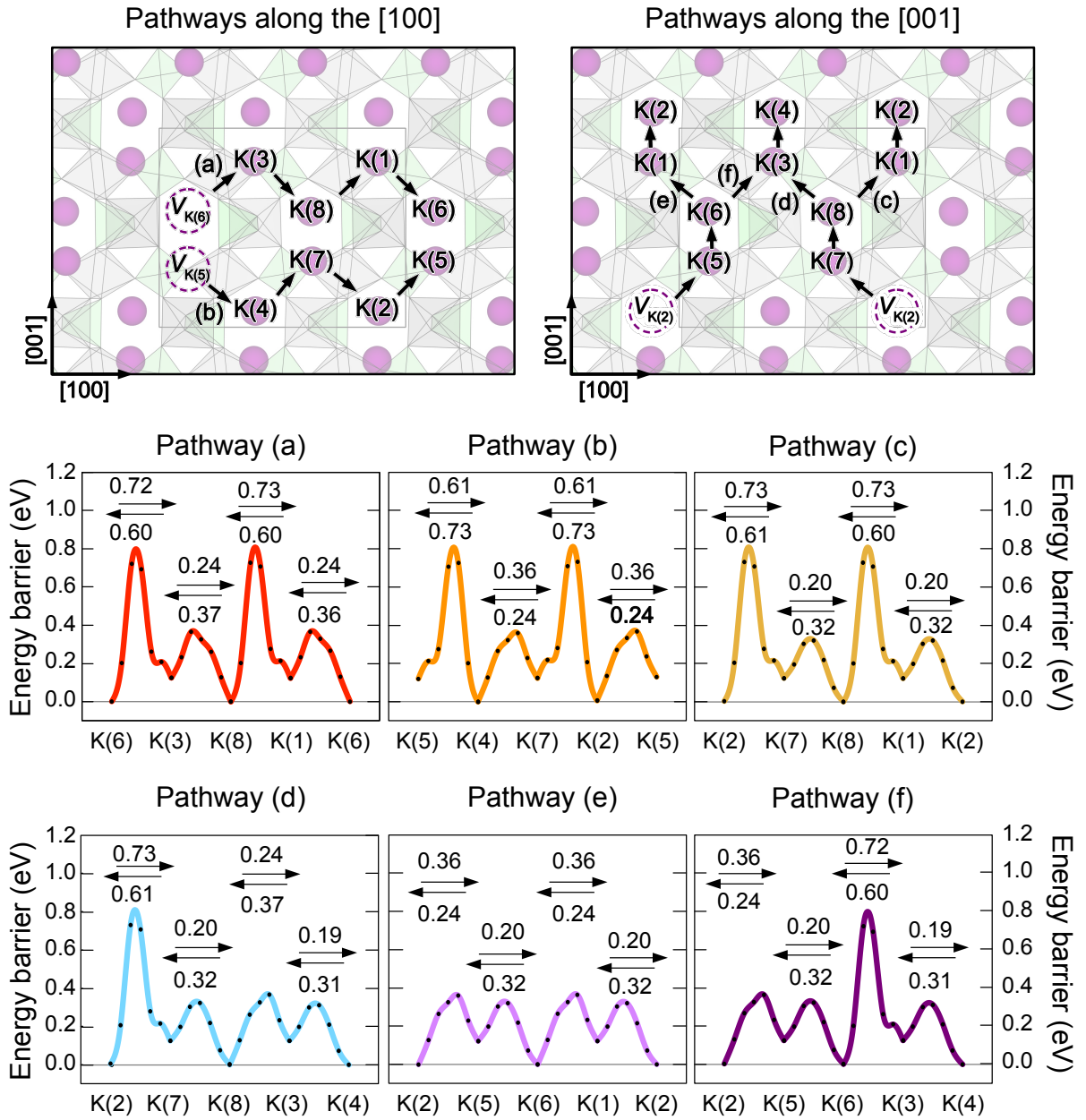
Figure 5.6: (Adapted from Ref. 187) K-vacancy migration along [100] (pathways (a) and (b)) and [001] (pathways (c)-(f)) as well as the corresponding activation energies.

Despite being slightly less favorable than the corresponding values in KTP[28] and those reported for the Rb migration in RbVPO$_4$F[31], the K deintercalation should still be fast enough for battery applications.

5.3 KTA Anodes

5.3.1 Models

Contrary to the modeling of the cathode material, to model a KTA anode additional potassium atoms have to be intercalated in the material. These provoke the reduction of neighboring titanium atoms. Upon the K intercalation the following reaction takes places

$$\text{KTiOAsO}_4 + x \left(\text{K}^{+1} + e^- \right) \longrightarrow \text{KTiOAsO}_4\text{K}_x. \tag{5.4}$$

Here, x is the concentration of intercalated K per formula unit. In analogy to the cathode material, the intercalation of neutral K atoms is simulated and the spin angular momentum is set to $S = \frac{n}{2}$, with n = 1-4 as the number of intercalated potassium atoms per unit cell.

Unlike in KTP anodes, where eight possible intercalation sites were found[29], in KTA the number of possible intercalation sites is reduced to four: The sites found in Ref. 29 are rather
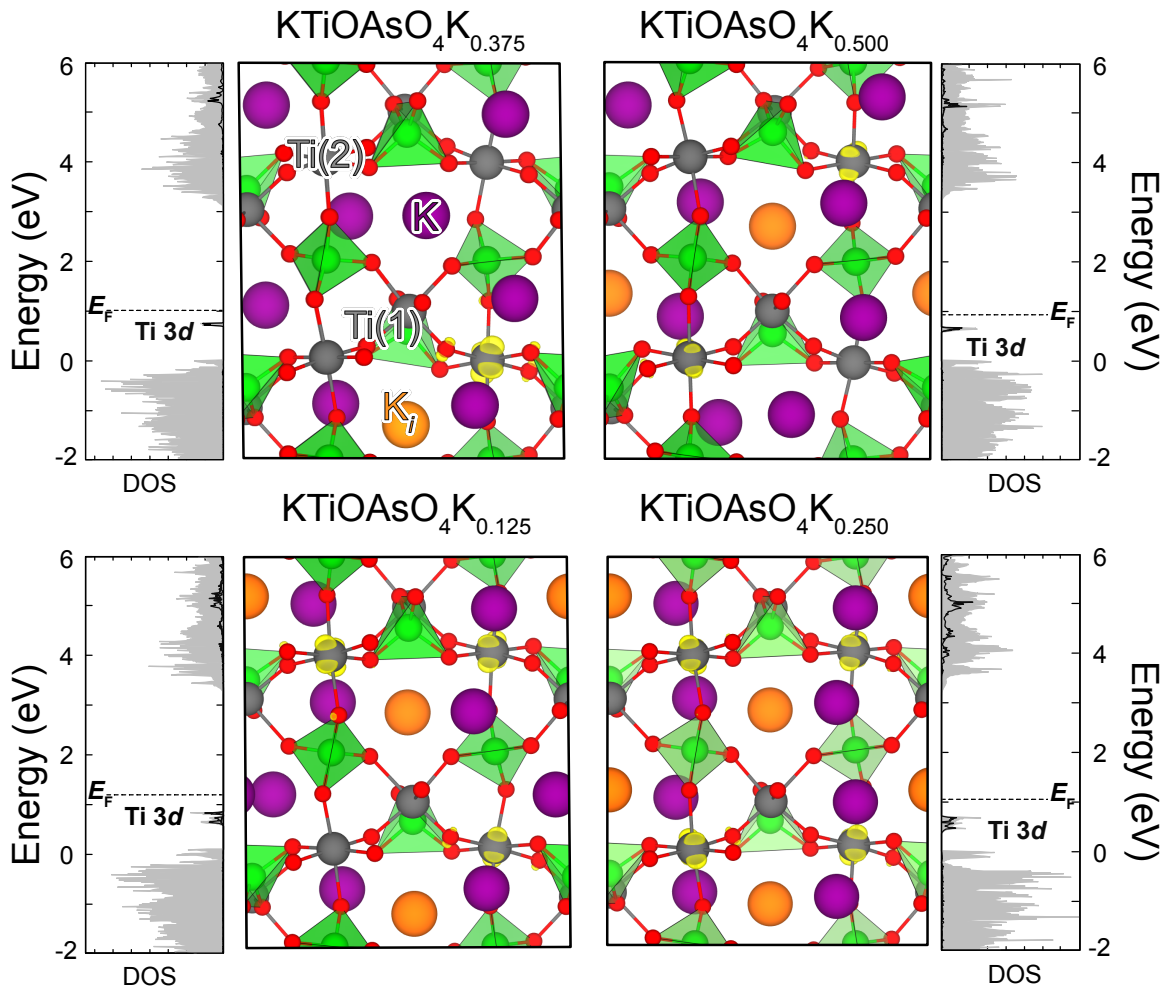

Figure 5.7: (Adapted from Ref. 187) Geometries of the most favorable KTiOAsO$_4$K$_x$ configurations with $0.125 \leq x \leq 0.500$. The K$_i$ sites are marked in orange. In addition, the electronic DOS as well as the electronic orbitals of mid-gap levels are shown.
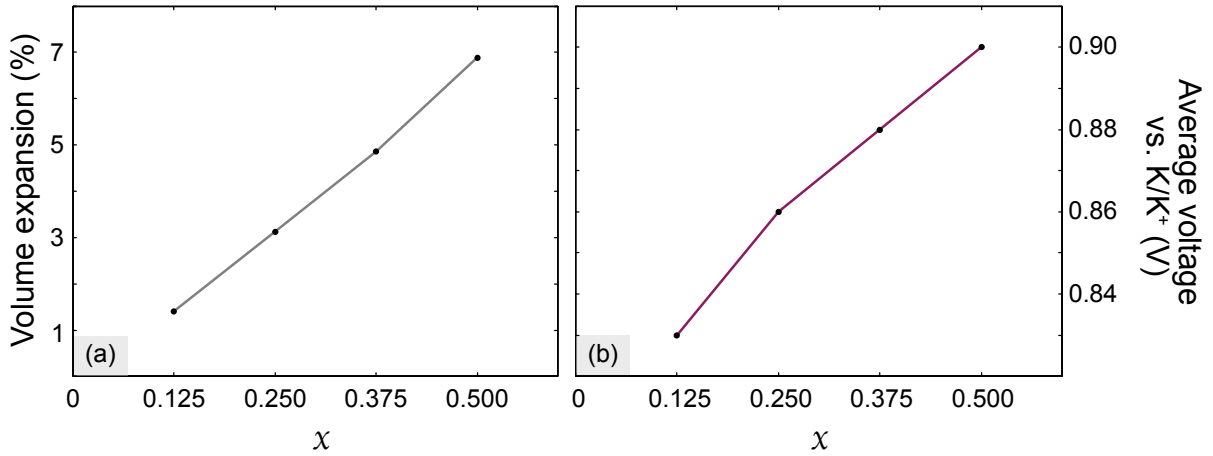
Figure 5.8: (Adapted from Ref. 187) (a) Volume expansion and (b) average voltages calculated for KTiOAsO$_4$K$_x$ with $0.125 \leq x \leq 0.500$.

unfavorable in KTA crystals probably due the larger volume of the AsO$_4$ units compared to the PO$_4$ tetrahedra. So, the intercalated potassium is more likely to position in larger cages parallel to the [010] direction instead of the [100] direction in KTA. More precisely, the intercalation sites in KTA correspond to the sites $M1$-$M4$ by Huang *et al.*[29], shifted by circa -25% of the lattice parameter b. Consequently, the concentration of intercalated potassium is in the range $x = 0.125$-0.5, summing up to 15 possible combinations for KTiOAsO$_4$K$_x$. All of these have been simulated and the lowest-energy configurations are depicted in Fig. 5.7.

The valence electron of every intercalated K atom reduces one of the neighboring Ti atoms transforming them from Ti^{4+} into Ti^{3+} centers. This is also visible from the plotted atomic orbitals in Fig. 5.7. Interestingly, only Ti(2) sites are reduced. The reduction of the titanium is accompanied by the formation of occupied Ti $3d$ mid-gap levels as visualized by the electronic DOS plotted in Fig. 5.7.

Simultaneously, the volume of the unit cell increases by up to 6.89% for $x = 0.5$, see Fig. 5.8a. This volume expansion is in the same order as the one in KTP[29] for the same concentration, and should not hinder a stable long-term operation.

Adapting Eq. 4.11 to KTA, the intercalation energy E_{in} (required for the calculation of the average voltage of the anode) can be calculated as

$$E_{\text{in}} = \frac{E_{\text{KTiOAsO}_4\text{K}_x} - E_{\text{KTiOAsO}_4} - x \cdot E_{\text{K}}}{x}, \tag{5.5}$$

with $E_{\text{KTiOAsO}_4\text{K}_x}$ corresponding to the energy of one formula unit of KTiOAsO$_4$K$_x$. Assuming values between $-0.8\,\text{eV}$ (when only one K is intercalated) and $-0.2\,\text{eV}$ (when all intercalation sites are occupied), the intercalation energy is always negative, indicating that the K atoms will spontaneously intercalate in the anode material.

According to Eq. 4.9, this leads to values between 0.83 and 0.90 V for the average voltage, with the voltage increasing as more K is intercalated in the cell, see Fig. 5.8b. Similar to the cathode material, KTA thus leads to slightly higher voltages compared to KTP[29] also in the case of the anode.

On more time, the higher molar mass of As compared to P results in lower gravimetric

capacities (between 13.58 and 51.26 mAhg^{-1}) and lower gravimetric energy densities (between 11.32 and 46.37 Whkg^{-1}) as the one obtained for KTP (between 16.52 and 61.61 mAhg^{-1}) for the same values of x[29].

5.3.2 Potassium-Ion Diffusion

To complete the discussion about the electrochemical performance of KTA anodes, we shall now discuss the K-ion intercalation mechanisms in the material. We thereby investigate the migration mechanisms of one single K interstitial (K$_i$) using again NEB routines.

Due to the peculiar positioning of the K intercalation sites, the K-ion migration along the [100] axis is hindered by the TiO$_6$-PO$_4$ chains parallel to [010]. Therefore, these pathways are rather unfavorable and will not be analyzed further.

Nevertheless, we will compute the migration along the [010] and the [001] directions. In the former case, the intercalated K ion would migrate from one intercalation site of one unit cell into its equivalent site of one adjacent cell. Therefore, a larger supercell, corresponding to the KTA unit cell doubled along [010], has to be modeled for the simulation. In the latter case, simulations are again performed within the KTA unit cell. As for the cathode material, four different ion migration pathways along the [001] axis can be identified, see Fig. 5.9.
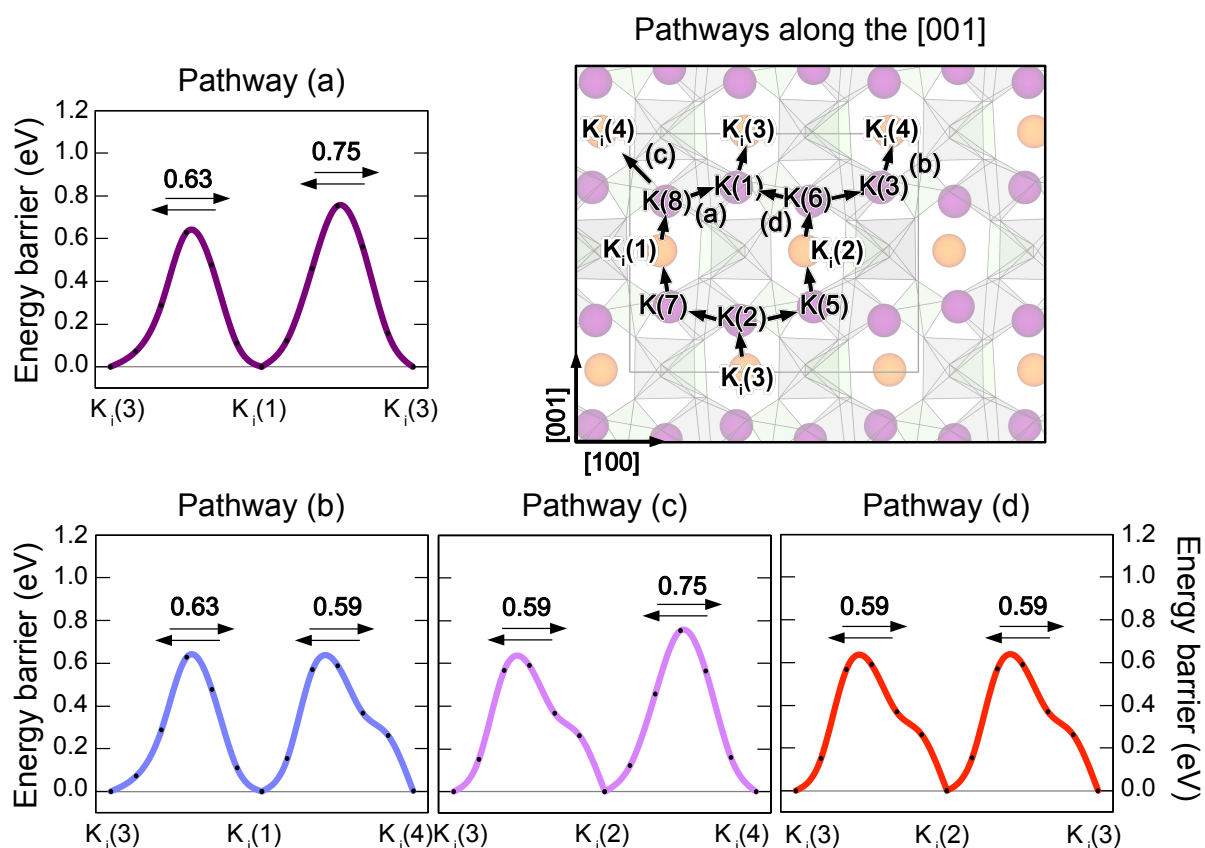

Figure 5.9: (Adapted from Ref. 187) K-ion migration along [001] as well as the corresponding activation energies. The ion migrates through the lattice assuming both intercalation sites K$_i$ and intrinsic lattice sites K(i).

Although the pathway features large channels, the migration along the [010] axis is characterized by an activation energy of 1.91 eV and, is therefore, quite improbable.

Along [001], on the other hand, the K_i migrates across the crystal occupying intercalation and intrinsic lattice sites. Different from the cathode material, the activation energy does not change locally in dependence of the direction in which the K_i moves. An attempt to explain this finding is that K^+ ions located at intrinsic and intercalation sites just interchange their positioning, so that none of the configurations is more favorable than the other. The energy barriers calculated for the ion migration do not differ significantly with respect to the chosen path. In addition, being all below 0.76 eV, they are lower than the one calculated for KTP crystals along the [100] axis[29]. To our knowledge, the migration mechanisms of K_i along the [001] axis of KTP have not been investigated, yet[2], so we are unaware of the barriers magnitude in this direction. Nevertheless, in analogy with the cathode material, we assume that they could be slightly more favorable than the one predicted here.

As found for the cathode, the most favorable migration pathway is the spiral pathway along the c axis, i.e., $K_i(3) \longrightarrow K(2) \longrightarrow K(5) \longrightarrow K_i(2) \longrightarrow K(6) \longrightarrow K(1) \longrightarrow K_i(3)$, corresponding to letter (d) in Fig. 5.9, which are characterized by barriers lower than 600 meV. So, both vacancies and ions would be more likely to follow this path during the migration across the crystal. This also reflects the experimental finding[191] that the diffusion coefficient along the c axis in KTA is higher compared to the remaining two.

5.4 Conclusion and Outlook

The electrochemical performance of KTA applied as a cathode and anode for K-ion batteries has been evaluated within the framework of DFT. We thereby focussed on the voltages arising upon K (de)intercalation, the volume deformation, and the diffusion barriers for the K-ion (K-vacancy) migration.

For the simulation of the cathode, we modeled K-deficient $K_{1-x}TiOAsO_4$ by deintercalating up to eight K atoms from the KTA unit cell. To simulate the anode, on the other hand, reducing defects were introduced by intercalating up to four K atoms in the cell.

Overall, the here calculated properties are promising. KTA is expected to reach high average working voltages of about 3.8 V, when it is simultaneously applied as cathode and anode. In addition, the material should guarantee a robust long term operation, since the K-(de)intercalation does not significantly affect the crystal lattice: The maximum volume shrinkage and expansion was calculated to be less than 7%.

Finally, the most favorable K-vacancy (K-ion) diffusion pathway corresponds to spiral K-channels along [001] and is characterized by activation energies lower than 370 meV (600 meV). KTA thus shows similar properties as other members of the KTP-type family.

Nevertheless, some considerations have to be made. First of all, KTA anodes do only allow for the intercalation of four K atoms compared to eight in KTP[29]. KTA cathodes, on the other hand, show higher average voltages compared to KTP[28]. So, we would suggest that KTA would show a better performance if applied as a cathode rather than an anode. In addition, due to the heavier group-V element, the gravimetric capacity is lower than the one in KTP[28, 29].

---

[2]Note that in Ref. 29 a different convention for the orientation for the crystal axes was used. More precisely, our a, b and c axes correspond to their a, $-c$ and b, respectively.

Finally, it has to be pointed out that KTA clearly holds the disadvantage of featuring a toxic element, i. e., arsenic (As).

Nevertheless, apart from the difference already pointed out, the material's performance is found to be close to the one of KTP. This means that our calculations show that the electrochemical performance of KTP-type crystals is not significantly altered by the nature of the XO_4 group. So, we suggest that the KTP framework might be also suitable to host different elements at the X sites, for example silicon (Si). Silicates, i. e., Li_2FeSiO_4, have already been tested as a cathode material. The material does show promising electrochemical properties, but is limited with respect to the ion mobility.[192] We expect that this problem could be solved by the high ionic conductivity of the KTP framework, which also allows for the migration of larger alkali ions. In addition, the lighter Ti atoms compared to Fe atoms would be beneficial in providing higher gravimetric capacities, and thus reduce the overall weight of the battery.

The replacement of As with Si should at least in theory be possible, since the average bond length[193] of the SiO bonds in Li_2FeSiO_4 is about 1.62 Å, which is very close to the average bond length of the AsO bonds in KTA (i. e., 1.68 Å[194]) and of the PO bonds in KTP (i. e., 1.54 Å[194]). Thereby, the (partial) replacement of O_{Ti-Ti} with fluorine (F) or higher concentrations of the alkali element could be required to compensate for the missing valence electron.

6

Optical Properties from First Principles

THE electronic properties of a solid-state system are encoded in its band structure. In the framework of quantum theory, the transition from one state to another can be accompanied by the absorption (excitation of an electron into a higher, unoccupied state) or the emission (relaxation of an electron into a lower, empty state) of a photon. The photon energy $\hbar\omega$ thereby corresponds to the difference between the energies E_1 and E_2 assumed by the electron as

$$\hbar\omega = E_2 - E_1. \tag{6.1}$$

The description of the light-matter interaction, however, can be carried out in a more classical picture. Under the influence of an electromagnetic wave, the electron and nuclei of the system start to oscillate with the frequency of the light field. Due to the oscillation, the fluctuating particles will in turn generate secondary waves, which can interfere with the original light field and other oscillating particles.[195]

In a crystal, all these microscopic fields can be averaged over each unit cell to generate a continuous function depending on the space coordinate $\boldsymbol{r}$. The average electric field causes an oscillating dipole moment, which leads to the electric polarization per unit cell $\boldsymbol{P}$[195]

$$\boldsymbol{P} = \frac{1}{V} \int \rho \, \Delta \boldsymbol{r} \, \mathrm{d}V, \tag{6.2}$$

with V as the unit-cell volume, ρ as the charge density and $\Delta\boldsymbol{r}$ indicating the amplitude of the oscillation, i. e., the charge displacement.

The combination of the electric field and the electric polarization leads to the electric displacement $\boldsymbol{D} = \boldsymbol{E} + 4\pi\boldsymbol{P}$. For moderate electric fields, the electric field is linear in the polarization, so the relation simplifies to[195]

$$D_i = \sum_{j=1}^{3} \varepsilon^{ij} E_{ij}, \tag{6.3}$$

where ε^{ij} corresponds to dielectric tensor.

In short, the dielectric tensor describes the response of the material to an incident electromagnetic field and should therefore depend both on its wave vector k and its frequency ω. Under the assumption that the spatial dispersion of the wave can be neglected, i.e., the case of large wavelengths compared to the unit cell dimensions, the dependency on the wave vector can be neglected, i.e., $\varepsilon^{ij}(k, \omega) \approx \varepsilon^{ij}(\omega)$.[195]

In the following, we will use ε to indicate one of the principal values of the dielectric tensor. To account for a phase difference between the electric field and the corresponding displacement, ε must assume complex values, i.e., $\varepsilon = \varepsilon_1 + i\varepsilon_2$. Thus, the expressions for both quantities read[195]

$$E(\omega) = E_0 e^{-i\omega t} + E_0^* e^{i\omega t} \tag{6.4}$$
$$D(\omega) = \varepsilon(\omega)E_0 e^{-i\omega t} + \varepsilon(-\omega)E_0^* e^{i\omega t} = \varepsilon(\omega)E_0 e^{-i\omega t} + \varepsilon^*(\omega)E_0^* e^{i\omega t} \tag{6.5}$$

In the last step, the relation $\varepsilon(-\omega) = \varepsilon^*(\omega)$ was assumed to guarantee a real value for $D(\omega)$.

To determine the losses per oscillation, the average dissipation rate $W = \dfrac{1}{4\pi}\left\langle E \cdot \dfrac{\partial D}{\partial t}\right\rangle$ has to be integrated over a oscillation period leading to[195]

$$W = \frac{\omega \varepsilon_2(\omega)}{4\pi}\langle E^2 \rangle. \tag{6.6}$$

Eq. 6.6 shows that the absorption properties of a medium are proportional to the imaginary part of the dielectric function. Therefore, losses can be attributed to non-zero values of ε_2.

Depending on the application, high absorption coefficients can be either desirable (e.g., in solar cells) or detrimental (e.g., in waveguides). Thus, the determination of the influence of dopants (or impurities) on a material's absorption properties is crucial for knowledge-driven solutions to enhance its response. In this chapter, we will introduce methodologies how to determine the dielectric function ε within DFT on different levels of theory. The discussion follows Ref. 117.

6.1 A Short Overview

For the calculation of the dielectric function ε within the DFT framework, a relation connecting the electronic density with the incident light field has to be derived. This can be achieved by the self-consistent solution of the Hedin's equations, which have already been introduced in Sec. 3.4.

From the Hedin's equations, a series of physical properties can be determined. One of these is the dielectric function of the system, which can be calculated as[117]

$$\varepsilon(1, 2) = \delta(1 - 2) - \int v(1 - 3)P(3, 2)\,\mathrm{d}3. \tag{6.7}$$

As mentioned before, for the solution of Hedin's equations, some approximations are required. Within the RPA (see Sec. 3.4), the expression for the polarizability reads

$$P(1, 2) \equiv P_0(1, 2) = -iG(1, 2)G(2, 1). \tag{6.8}$$

At this point, it should be noted that the polarizability functions P_0 and P in the framework of the Green's function formalism are used as synonyms for the independent-particle polarization χ^0 and the full polarizability χ. However, formally only the equality $\chi^0 = P_0$ holds. These two quantities describe, how the electronic density responds to a change in the total effective potential $v_{\text{eff.}}$ and in the external potential $v_{\text{ext.}}$, respectively, as[117]

$$\delta n(\mathbf{r}) = \int \chi^0(\mathbf{r}, \mathbf{r}')\delta v_{\text{eff.}}(\mathbf{r}')\, \mathrm{d}^3\mathbf{r}'$$
$$\delta n(\mathbf{r}) = \int \chi(\mathbf{r}, \mathbf{r}')\delta v_{\text{ext.}}(\mathbf{r}')\, \mathrm{d}^3\mathbf{r}'. \tag{6.9}$$

The dielectric function can be derived from the polarizability as

$$\varepsilon(1, 2) = \delta(1 - 2) - \int v(1 - 3)\chi(3, 2)\, \mathrm{d}3, \tag{6.10}$$

assuming the same shape as Eq. 6.7. Under the constraint that the perturbation is caused by a test particle, the RPA can again be applied leading to the following simplified expression for the dielectric function[117]

$$\varepsilon_{\text{RPA}} = \delta(1 - 2) - \int v(1 - 3)\chi^0(3, 2)\, \mathrm{d}3. \tag{6.11}$$

In the following two sections we will elaborate on the computation of ε within the DFT framework at different levels of theory.

6.1.1 The Independent-Particle Approximation

The above discussed dielectric function corresponds to the microscopic dielectric function. Its inverse is a measure for the screening of a system and is defined as the variation of the effective potential under a change in the external potential as

$$\varepsilon^{-1}(1, 2) \equiv \frac{\delta v_{\text{eff.}}(1)}{\delta v_{\text{ext.}}(2)}. \tag{6.12}$$

This expression can be transformed into momentum space via the Fourier transform over the Brillouin zone (BZ) as[117]

$$\varepsilon^{-1}(\mathbf{r}, \mathbf{r}'; \omega) = \frac{1}{2\pi^3} \int_{BZ} \sum_{\mathbf{G}, \mathbf{G}'} e^{i(\mathbf{q}+\mathbf{G})\cdot\mathbf{r}} \varepsilon^{-1}_{\mathbf{G}\mathbf{G}'}(\mathbf{q}, \omega)\, e^{-i(\mathbf{q}+\mathbf{G})\cdot\mathbf{r}'}\, \mathrm{d}\mathbf{q}. \tag{6.13}$$

In Eq. 6.13 $\mathbf{G}$ and $\mathbf{G}'$ are reciprocal lattice vectors and the wave vector $\mathbf{q}$ lies in the first BZ. Although all microscopic electric fields vary with the same frequency ω, due to a non-constant value for $\mathbf{q} + \mathbf{G}$ they undergo microscopic fluctuations. These microscopic fluctuations are thereby referred to as local-field effects.[117]

The inverse of the dielectric function ε^{-1} can be related to the macroscopic dielectric function, which describes the optical properties of a material via

$$\varepsilon_{\text{M}}(\omega) = \lim_{q \to 0} \frac{1}{\varepsilon^{-1}_{\mathbf{G}\mathbf{G}'}(\mathbf{q}, \omega)}\bigg|_{\mathbf{G}=\mathbf{G}'=0} \tag{6.14}$$

as showed by Adler[196] and Wiser[197]. Thereby, the limit $q \rightarrow 0$ implies that only vertical transitions are allowed. So, adopting matrix notation for brevities sake, the inverse of Eq. 6.11 in the RPA is given by[117]

$$\varepsilon_{\text{RPA}}^{-1} = 1 + v(1 - \chi^0 v)^{-1} \chi^0.$$ (6.15)

One of the possible approximations carried out during the calculation of χ_0 is the neglection of local-field effects. This corresponds to the so-called independent-particle approximation (IPA), where the polarization of independent particles χ^0 corresponds to the Adler-Wiser expression[117,196,197]

$$\chi^0(\boldsymbol{r}, \boldsymbol{r}'; \omega) = 2 \sum_{i,j} (f_i - f_j) \frac{\varphi_i(\boldsymbol{r}) \varphi_j^*(\boldsymbol{r}) \varphi_i^*(\boldsymbol{r}') \varphi_j(\boldsymbol{r}')}{\epsilon_i - \epsilon_j - \hbar(\omega + i\eta)},$$ (6.16)

with its Fourier transform

$$\chi^0(\boldsymbol{q}; \omega) = 2 \sum_{i,j} (f_i - f_j) \frac{\langle \varphi_j | e^{-i(\boldsymbol{q}+\boldsymbol{G})\cdot\boldsymbol{r}} | \varphi_i \rangle \langle \varphi_i | e^{i(\boldsymbol{q}+\boldsymbol{G}')\cdot\boldsymbol{r}'} | \varphi_j \rangle}{\epsilon_i - \epsilon_i - \hbar(\omega + i\eta)}.$$ (6.17)

In Eqs. 6.16 and 6.17, the summation extends over the quantum numbers of a solid, i. e., i and j indicate the band index (v for a valence band, c for a conduction band) and the corresponding wave vectors $\boldsymbol{k}$ and $\boldsymbol{k}'$. $\eta > 0$ is an infinitesimal number and $f_{i,j}$ indicate the respective occupation numbers. For a semiconductor, f can assume either the values 1 or 0 for valence or conduction bands. In addition, $|\varphi_{i,j}\rangle$ and $\epsilon_{i,j}$ refer to the Kohn-Sham eigenstates and eigenvalues, respectively.

Neglecting local-field effects, only the matrix element for $\boldsymbol{G} = \boldsymbol{G}' = 0$ has to be considered in Eq. 6.14. With these simplifications and indicating the unit-cell volume with V, the macroscopic dielectric function reads[117]

$$\varepsilon_{\text{M}}(\omega) = 1 + 2\frac{4\pi}{V} \lim_{q \rightarrow 0} \frac{1}{q^2} \sum_{k,c,v} \left\{ \frac{|\langle c\boldsymbol{k} + \boldsymbol{q}| e^{i\boldsymbol{q}\cdot\boldsymbol{r}} |v\boldsymbol{k}\rangle|^2}{\epsilon_{c\boldsymbol{k}+\boldsymbol{q}} - \epsilon_{v\boldsymbol{k}} - \hbar(\omega + i\eta)} \right.$$

$$\left. + \frac{|\langle c\boldsymbol{k} - \boldsymbol{q}| e^{-i\boldsymbol{q}\cdot\boldsymbol{r}} |v\boldsymbol{k}\rangle|^2}{\epsilon_{c\boldsymbol{k}-\boldsymbol{q}} - \epsilon_{v\boldsymbol{k}} + \hbar(\omega + i\eta)} \right\}$$ (6.18)

Spectra calculated within the IPA usually do not reproduce experimental absorption spectra accurately: In fact, the IPA does not only suffer from a pronounced redshift due to the systematic underestimation of the fundamental band gap, but it does also neglects excitonic effects, i. e., electrostatic interactions between electrons and holes.[198] In this thesis, we will show that the intrinsic limitations of the IPA can be overcome to some extent by the use of modified hybrid functionals[1]. Thus, a detailed discussion of approaches most established for the computation of realistic optical properties will go beyond the scope of this work. Nevertheless, they shall be shortly introduced in Sec. 6.1.2.

---

[1]The application of hybrid functionals is motivated by strongly localized defect states, which can not be described by (semi-)local functionals. So, using this wrong electronic structure as a starting point for further calculations is expected to lead to unreliable optical properties.

6.1.2 Towards Realistic Absorption Properties

One major problem of the IPA is a drastical underestimation of single-particle excitation energies. As a consequence, IPA spectra usually suffer from a severe red shift compared to experimental data, ensuring only to a qualitative agreement between theory and experiment.[198]

An immediate correction of the absorption onset can be achieved by substituting the Kohn-Sham eigenvalues ϵ_i in Eq. 6.18 with the quasiparticle energies (see Eq. 3.30) as calculated within the GW[121, 198] (DFT+GW), yielding the independent-quasiparticle approximation (IQA).

The quasiparticle energies can, for example, be directly obtained by calculating self-energy corrections within the GW approximation. Another approach to include the GW blueshift was presented by Del Sole and Girlanda in Ref. 199: If the magnitude of the blueshift is known and nonlocality and gauge invariance are taken into account, the IQA dielectric function can also be computed on top of (semi-)local wave functions by the application of a scissor operator Δ. For this, the band-gap width is opened rigidly by Δ and, thus, the absorption onset of the IPA dielectric function $\varepsilon^{\mathrm{IPA}}$ is shifted by $\omega' = \Delta/\hbar$ towards higher energies, as

$$\varepsilon^{\mathrm{IQA,scissor}} = \varepsilon^{\mathrm{IPA}}\left(\omega - \frac{\Delta}{\hbar}\right). \tag{6.19}$$

For the explicit inclusion of local-field effects, on the other hand, the dielectric matrix has to be inverted as required by Eq. 6.14. This computationally very demanding approach can be overcome by introducing the modified polarizability[117]

$$\bar{P}_{GG'}(\boldsymbol{q}, \omega) = P_{GG'}(\boldsymbol{q}, \omega) + \sum_{K,K'} P_{GK}(\boldsymbol{q}, \omega)\bar{\varepsilon}_{KK'}^{-1}(\boldsymbol{q})\bar{v}_{K'}(\boldsymbol{q})\bar{P}_{K'G'}(\boldsymbol{q}, \omega), \tag{6.20}$$

with

$$\bar{\varepsilon}_{G,G'} \equiv \delta_{G,G'} - \bar{v}_G(\boldsymbol{q})P_{G,G'}(\boldsymbol{q}, \omega) \tag{6.21}$$

and neglecting the Coulomb interactions for $\boldsymbol{G} = \boldsymbol{0}$ via

$$\bar{v}_G \equiv \begin{cases} 0 & , \quad \boldsymbol{G} = \boldsymbol{0} \\ v_G & , \quad \boldsymbol{G} \neq \boldsymbol{0} \end{cases}. \tag{6.22}$$

This leads to the following expression for the macroscopic dielectric function

$$\varepsilon_{\mathrm{M}}(\omega) = 1 - \lim_{q \to 0}\left[v_0(\boldsymbol{q})\bar{P}_{00}(\boldsymbol{q}, \omega)\right]. \tag{6.23}$$

For details, the Reader is referred to Ref. 117.

Although the IQA has already been shown to yield optical spectra in closer agreement with the experiment compared to IPA, it still neglects excitonic effects.[198]

The excitonic effects, however, can have a very strong influence on the absorption properties of a material, leading not only to a red-shifted absorption spectrum compared to the IQA, but can also cause the formation of sharp, localized absorption signatures (located at energies lower than the absorption onset), which are caused by the excitonic states themselves.[122]

For the inclusion of excitonic effects, one has to go beyond the GW approximation by further

iterating Hedin's equations. The result of the additional iteration is the Bethe-Salpeter equation (BSE)[117,200]

$$\bar{P} = P_0 + P_0(\bar{v} - W)\bar{P}. \tag{6.24}$$

In Eq. 6.24, $\bar{P}$ is a generalization of the two-point polarizability $P(1, 2)$ into a four-point one and $\bar{v}$ corresponds to the Coulomb potential without the long-range part. For the sake of completeness (details can be again found again in Ref. 117), the macroscopic dielectric function after the solution of the BSE reads[117]

$$\varepsilon_{\mathrm{M}}(\omega) = 1 - 2 \lim_{q} v_0(q) \sum_\lambda \left\{ \left| \sum_{v,c,k} \langle vk| e^{-iq\cdot r} |ck\rangle A_\lambda^{(vck)} \right|^2 \right.$$

$$\left. \times \left(\frac{1}{E_\lambda - (\omega + i\eta)} + \frac{1}{E_\lambda + (\omega + i\eta)} \right) \right\}. \tag{6.25}$$

Here, $A_\lambda^{(vck)}$ and E_λ are the eigenfunctions and the eigenvalues of the BSE Hamiltonian.

The solution of the BSE partially compensates the *GW* blueshift by redistributing the oscillator strengths to lower photon energies.[121,201–203] Thus, a combined application of the *GW*+BSE is most established for the computation of optical properties in quantitatively good agreement with experimental spectra.[204–207]

<div align="right">

7

</div>

Optical Absorption Properties
of Oxygen Vacancies

IN this chapter we will examine the impact of O vacancies on the transmission properties of KTP crystals.

As described in Sec. 2.3, O vacancies located between two Ti atoms are discussed to be instrumental for the formation of gray tracks in KTP crystals. In order to investigate if their presence can directly be connected to this phenomenon, *ab initio* studies have to be conducted. Only within theoretical investigations, in fact, isolated point defects can be modeled and their characteristic optical signatures can be resolved. During the computation, however, the correction of the fundamental-gap width is crucial for the achievement of realistic absorption properties.

The combined application of the *GW*+BSE methodology, which is most-established to overcome the intrinsic band-gap problem of DFT-calculations caused by (semi-)local exchange and correlation functionals, has already provided fruitful results for the calculation of the optical response of stoichiometric KTP[208,209]: It was found that the inclusion of self-energy effects induces a blue shift of about 2 eV, which is then partially compensated by a 1.5-eV red shift caused by excitonic effects[208]. The combined application then leads to spectra in close agreement with experimental data[81].

This procedure, unfortunately, is not directly applicable after the introduction of O_{Ti-Ti} vacancies. In fact, the peculiar nature of Ti $3d$ defect states caused by O(10) vacancies hinders the utilization of the *GW*+BSE methodology: Since the underlying (semi-)local PBEsol functional delocalizes these defect states, the *GW* approximation based on this improper electronic structure would lead to unreliable optical properties.

In the following sections, a different approach for the calculation of high-end optical properties will be presented, combining (i) a realistic prediction of the system's fundamental band gap with (ii) an accurate localization of defect states: The PBE0-10% methodology[1]. The va-

---

[1]Note that the PBE0[143,144] functional is applied, since it provides defect geometries and hyperfine tensors in close agreement with PBEsol+U[111,112,135] structures in Ref. 95, and 10% refers to the fraction α of EXX, which has to be included in the calculation to match the absorption onset of *GW*+BSE optical properties. However, different systems may require the application of different hybrid functionals, e.g., B3LYP[145–147] or HSE[141,142], and/or different fractions of EXX.

lidity of this procedure as an alternative to the *GW*+BSE will be shown in Sec. 7.3. The results presented in this Chapter have already been published and the discussion follows Ref. 210.

7.1 Computational Details

The open-source program package Quantum ESPRESSO (QE)[188,189] is used to determine of the ground-state (defect) geometries within the DFT framework. Throughout this chapter, it is assumed that the defect concentration is low enough to not alter the crystal shape. Thus, the lattice constants are kept at the fixed values of $a = 12.859\,\text{Å}$, $b = 6.432\,\text{Å}$, and $c = 10.599\,\text{Å}$ determined in a previous study[211]. This values deviate less than 0.5 % from experimental data[61].

During the geometry optimization, the Brillouin-zone sampling is restricted to the Baldereschi point[190], and atomic wave functions are expanded into plane waves up to an energy cutoff of 100 Ry. Thereby, the atomic positions are optimized until fluctuations of energy and residual forces are below $10^{-8}\,\text{Ry}$ and $10^{-4}\,\text{Ry/bohr}$, respectively. For the modeling of the electron-ion interactions, norm-conserving pseudopotentials with the Ti $3d^3\,4s^{0.5}$, P $3s^2\,3p^3$, K $4s^1$, and O $2s^2\,2p^4$ states as valence states are used[2].

Electronic exchange and correlation is described within the GGA using the PBEsol[111,112] functional. The vacancy of interest, i.e., $V_{\text{O}(10)}$, features strongly localized occupied defect levels within the one-fold positively charged and the neutral charge state. Under the application of (semi-)local functionals and the Slater-Janak transition state model[139,212], their formation energy suggests that both the neutral $V_{\text{O}(10)}^0$ and the EPR active $V_{\text{O}(10)}^{+1}$ are not energetically favorable, since both the $(+2/+1)$ and the $(+1/0)$ charge transition states are located above the band gap[211]. In order to achieve an accurate description of these defect states, a Hubbard[135] energy correction of $U = 5.1\,\text{eV}$[95] is applied to the Ti $3d$ states. The Hubbard correction has been determined self-consistently[211] via the simplified scheme of Cococcioni and de Gironcoli[135] (also see Sec. 3.5) based on an effective Hubbard U and atomic wave functions for the construction of the projectors on the localized orbitals. This procedure results in KTP bulk[3] and defect geometries, which have been verified by comparing calculated[95] and measured[54] hyperfine tensors.

The optical properties of the PBEsol+U structures are computed utilizing the open-source code Yambo[213,214]. Thereby, calculations are limited to the IPA level of theory. In order to compute realistic absorption spectra, a modification of the hybrid functional PBE0[143,144] (PBE0-10% in the following) is used. Normally, the PBE0 functional describes the electron correlation within the PBE[109], but replaces the PBE exchange with a fraction $\alpha = 25\,\%$ of EXX from Hartree-Fock theory. Here, the α is reduced to 10 % to partially compensate for the quasiparticle energies as well as excitonic effects. To achieve numerically converged spectra, the k-point sampling is increased to a Γ-centered $3 \times 6 \times 3$ mesh, while the energy cutoff is lowered to 90 Ry to reduced the computational effort.

---

[2]The fractional occupation of the orbitals is deprived from any physical meaning and motivated by technical reasons to improve the transferability of the pseudopotentials.

[3]Note that also defects will be modeled within bulk material. In this work, however, the term "bulk" will be used to indicate stoichiometric volume cells.

7.2 Oxygen Vacancies in KTP: Charge States and Spin Configurations

As mentioned in Chap. 2, it is impossible to grow perfect stoichiometric KTP crystals. In fact, every crystal is to some extent deficient in K. These defects can be charge-compensated by a variety of defects, for example (charged) oxygen vacancies.

Due to their coordination, two different types of O vacancies can be identified. Eight atoms (i.e., O(1)-O(8)) are coordinated to both one Ti and one P atom. The remaining two (i.e., O(9) and O(10)) are coordinated to Ti, exclusively. The respective O vacancies will be denoted as $V_{\text{Ti}-\text{P}}$ and $V_{\text{Ti}-\text{Ti}}$, respectively.

Regardless their coordination, O vacancies can release up to two electrons. These electrons can be stabilized by the Ti atoms near the vacancy, thus leading to their reduction, or be extracted from the cell. On the other hand, positively charged O vacancies may also trap unpaired electrons. Thus, the charge states $+2$, $+1$, and 0 are theoretically possible.

Notably, the different coordinations of the O atoms have a strong influence on the nature of the related defect states. As shown in Ref. 211, $V_{\text{Ti}-\text{P}}$ in the charge states $+1$ and 0 give rise to localized mid-gap defect levels already on the DFT level of theory (i.e., using the (semi-)local PBEsol). Nevertheless, their formation energies calculated using the Slater-Janak transition state model[139,212], suggest that these vacancies show a pronounced negative-U behavior[4]. One of the main consequences of the negative-U effect is that, at least in the thermodynamic equilibrium, the vacancies are not expected to be stable within the charge state $+1$. So, being EPR silent in the equilibrium charge states, these vacancies can not be experimentally resolved, but may still strongly impair the properties of KTP[5].[211]

(Semi-)local functionals, on the other hand, fail in the description of the defect states caused by $V_{\text{Ti}-\text{Ti}}$. The application of the PBEsol functional leads to an artificial delocalization of occupied Ti $3d$ defect states so that the charges $q = +1$ and $q = 0$ are erroneously predicted to be metallic (also see Fig. 7.3). Therefore, the PBEsol formation energy would exclude the generation of these two charge states. This clearly contradicts the experimental findings of an EPR and ENDOR study by Setzler et al.[54], who attributed the hyperfine signatures of thermally stable Ti^{3+} centers (which are discussed to be strictly related to the gray-track phenomenon, also see Sec. 2.3) to be caused by $V_{\text{Ti}-\text{Ti}}$.

The inaccurate prediction of the electronic structure of the one-fold positively charged and the neutral vacancy can, however, be overcome by applying a Hubbard energy correction of $U = 5.1\,\text{eV}$ on the Ti $3d$ states[95]. This correction provides a better description of the strongly localized Ti $3d$ orbitals and is thus helpful to model the defect states of interest, here. Subsequent to the application of the Hubbard U, in fact, the defect-related occupied states lower into the band gap[95] (see Fig. 7.3). As a consequence, also the $(+2/+1)$ and the $(+1/0)$ charge transition states are lowered, and also the charge states $+1$ and 0 are predicted to be stable, also see Fig. 7.1.

---

[4]Negative-U behavior can be observed if the defect under consideration traps the second hole (or electron) more strongly than the first[215].

[5]The negative-U behavior is caused by a strong geometry relaxation during the transition from $+1$ to $+2$ due to electrostatic forces: After the removal of the oxygen atom, a dangling bond at the P site forms. This stabilized the main part of the released charge in the one-fold positively charged and the neutral charge state, leading to the formation of an electron cloud between the Ti and the P sites. So, since these atoms hold an effective positive charge, the electron cloud helps to shield the repulsive force acting on the two atoms. In the charge state $+2$, i.e., when the dangling bond is completely emptied, this compensating effect vanishes and the two atoms repel each other. This causes a strong geometry relaxation.[211]
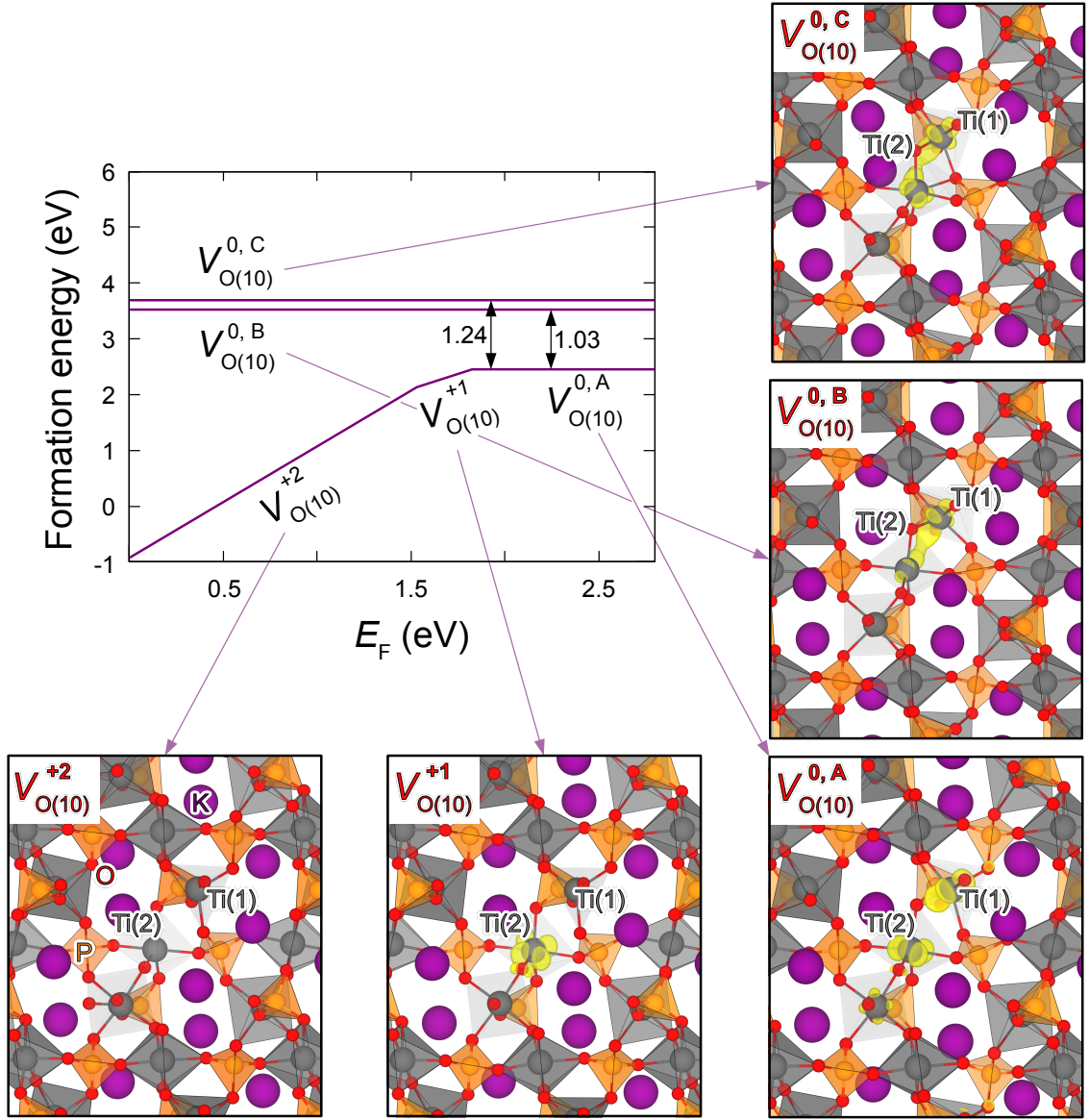
Figure 7.1: (Adapted from Refs. 95 and 210) PBEsol+U defect geometries and formation energy calculated via the Slater-Janak transition state model[139,212] of the vacancy $V_{O(10)}^q$ within the three charge states $q = +2$, $+1$, and 0. E_F indicates the Fermi energy. The yellow isosurfaces correspond to the charge density of the occupied defect levels present in the charge states $+1$ and 0. Note that the charge state $+2$ does not feature any occupied defect level. For the neutral $V_{O(10)}^0$, three different spin configurations can be identified. Thereby, the most stable configuration (A) corresponds to a spin-triplet ($S = 1$), the remaining (B and C) to two nonequivalent spin-singlet ($S = 0$) configurations.

In addition, the one-fold positively charged vacancy $V_{O(10)}^{+1}$ (causing the reduction of the Ti atom at the site Ti(2) near the vacancy, see Fig. 7.1) was thereby found[95] to lead to the best agreement with the experimental Ti^{3+}-related hyperfine tensors by Setzler and co-workers[54].

Regarding the neutral vacancies, on the other hand, a total of three different geometries are possible: The energetically most stable is thereby the spin-triplet ($S = 1$) configuration

($V_{O(10)}^{0,\text{A}}$), which is already predicted under the application of the Hubbard correction[95]. In this case, the electrons released by the O vacancy are localized at the Ti(1) and T(2) atoms adjacent to the vacancy and cause two defect states in the band gap, see Fig. 7.1. $V_{O(10)}^{0,\text{A}}$ might be experimentally resolvable under intentional excitation, and its hyperfine signatures should be distinguishable from those of the $S = \frac{1}{2}$ configuration.

In addition, two neutral spin-singlet configurations ($S = 0$) can be achieved by including 25 % of EXX via the hybrid PBE0 functional during the geometry optimization. As a starting point, the defect geometries of $V_{O(10)}^{0,\text{A}}$ and $V_{O(10)}^{+1}$ are chosen. The so-obtained defect structures are referred to as $V_{O(10)}^{0,\text{B}}$ and $V_{O(10)}^{0,\text{C}}$, respectively, see Fig. 7.1. Note that a subsequent geometry relaxation under the application of the PBEsol$+U$ functional does not change the defect geometries significantly. Since they are diamagnetic, their presence in the crystal cannot be directly measured via EPR spectroscopy. However, they may still form upon charge transition or optical excitation despite being 1.03 eV and 1.24 eV energetically less favorable compared to $V_{O(10)}^{0,\text{A}}$ (see Fig. 7.1). In both diamagnetic configurations, the extra electrons are localized by a hybridization of the Ti(1) and Ti(2) orbitals.

Comparing the three defect geometries of the neutral vacancies with that of $V_{O(10)}^{+1}$, it is notable that the $S = 0$ spin configurations undergo a rather strong geometry relaxation. This holds especially for $V_{O(10)}^{0,\text{C}}$, see Fig. 7.1. After the geometry optimization upon the removal of one electron, however, all the three neutral vacancies relax into the same structure. This defect geometry does not differing significantly from $V_{O(10)}^{+1}$, but the position of the trapped electron is located at the Ti(1) and not at the Ti(2) site near the vacancy. Nevertheless, since there is no experimental evidence of their presence in KTP crystals, this vacancy will not be considered further in this chapter.

7.3 Assessing an Unconventional Approach

Although the PBEsol$+U$ formation energy does indeed predict the formation of the charge state of interest, it still fails in widening the fundamental band gap, i. e., $E_g^{\text{PBEsol}+U} = 2.8\,\text{eV}$ vs. $E_g^{\text{opt.}} = 3.2 - 3.8\,\text{eV}$[81–84] derived from optical measurements, resulting in a severe red shift of the imaginary part of the dielectric function ε, see Figs. 7.2.

As discussed in Chap. 6, in order to compute realistic spectra, the combined application of the GW approximation and the solution of the Bethe-Salpeter equation (BSE) is most established. Thereby, the former corrects the electronic self-interaction as well as many-body effects and the latter includes excitonic effects. Unfortunately, the strongly localized defect states discussed in this work prevent us from applying of this methodology. Most probably, a self-consistent GW on top on the PBEsol$+U$ electronic structure could result in reliable electronic properties. However, this method would lead to unaffordable computational costs, caused by the system's size and the presence of symmetry-lowering defects.

Nevertheless, in the literature many examples can be found, in which the single-particle excitation energies have been corrected by the inclusion of a fraction α of EXX from Hartree-Fock theory via hybrid functionals. The magnitude of the α can be adapted to fit the experimental band gap and hybrid functionals simultaneously provide an accurate description of localized defect states, too.[216–223]

First, however, we will have to investigate if this unconventional approach does lead to

reliable spectra. For this, we start by comparing the optical absorption of stoichiometric KTP calculated (i) on the IQA level of theory (see Sec. 6.1.2) and (ii) on the IPA level of theory (see Sec. 6.1.1) on top of the PBE0 electronic structure.

Applying the standard fraction[143] $\alpha = 25\%$ of EXX included in the PBE0 functional widens the fundamental gap from $E_{\text{gap}}^{\text{PBEsol+U}} = 2.8\,\text{eV}$ to $E_{\text{gap}}^{\text{PBE0}} = 5.33\,\text{eV}$. Although this value strongly overestimates the absorption onset of KTP[81–84], it is in good agreement with the one obtained by Neufeld *et al.*[208] after the inclusion of quasiparticle effects via the *GW* approximation (i. e., $E_{\text{gap}}^{GW} = 5.23\,\text{eV}$). Due to the larger fundamental band-gap width, also the onset of the imaginary part of the IPA dielectric function is blue-shifted by more than 2.5 eV compared to the PBEsol+*U* spectra, resulting in an onset comparable to the IQA spectra by Neufeld *et al.*[208]. In the second step, exploiting the error compensation between electron-hole interactions and self-energy effects[201–203, 224, 225], we tune the fraction of EXX in order to emulate the red shift induced by the inclusion of excitonic effects via the solution of the BSE. More precisely, we find that the fraction $\alpha = 10\%$ red-shifts the absorption onset by over 1.5 eV, leading to a good agreement with both experimental data[81] and previous *GW*+BSE studies[208, 209], see Fig. 7.2.

Thus, since this modified hybrid functional does also describe the position and the shape of the main absorption peak correctly, we conclude that IPA spectra computed on top on the PBE0-10% electronic structure provide a realistic description of the optical properties of stoichiometric KTP.

Nevertheless, is the PBE0-10% still sufficiently accurate in the description of defect-related mid-gap levels, and thus also suitable for the computation of the optical signatures caused by
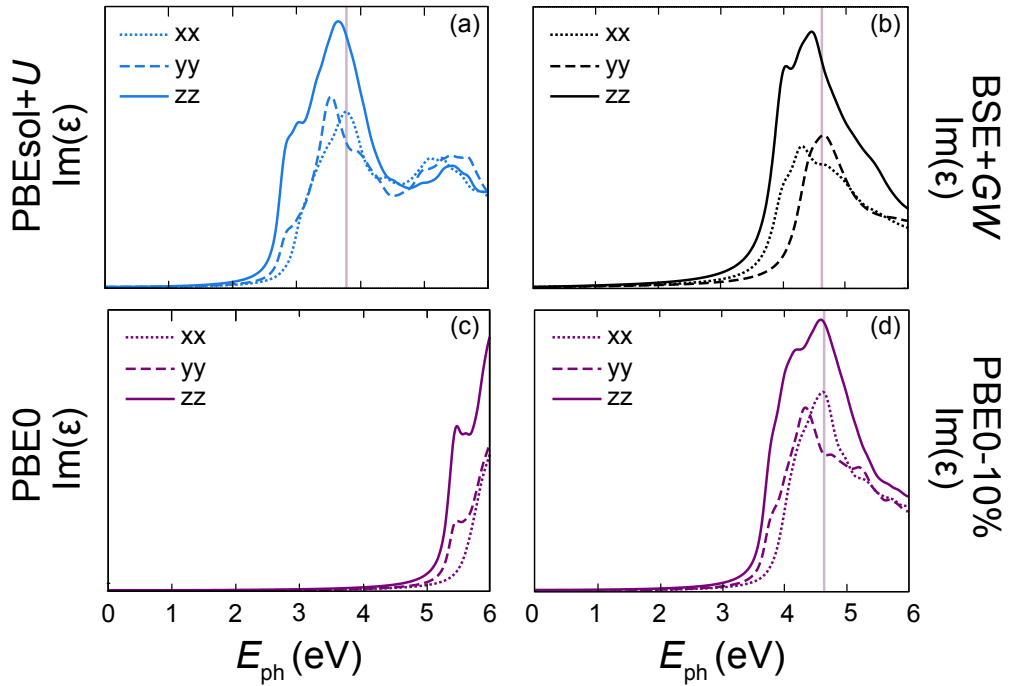

Figure 7.2: (Adapted from Ref. 210) Diagonal components of the imaginary part of the dielectric function ε calculated for a stoichiometric KTP unit cell under the application of (a) the PBEsol functional together with a Hubbard correction of $U = 5.1\,\text{eV}$, (b) the BSE+*GW* methodology[208], (c) the standard PBE0 functional (including 25 % of EXX), and (d) the PBE0+10% formalism.

these strongly bound excitonic states?

To answer the first part of this question, we compute the electronic density of states (DOS) of the vacancy $V_{O(10)}^{+1}$ under the application of different functionals. The results are depicted in Fig. 7.3. The standard PBE0 functional (i.e., $\alpha = 25\%$) locates the defect level caused by the vacancy at about 2.4 eV above the valence band maximum (VBM). It is clearly visible that the position of this level remains nearly unchanged also under the application of the modified PBE0-10%. Thus, the energetic positioning of occupied defect levels is not significantly affected by the reduction of the α. At this point, however, we have to point out that the energetic position of the mid-gap level within the PBEsol+U framework does not match with those previously discussed. The reason for this finding is that the magnitude of the U parameter influences the positioning of the state in the gap.

However, the reduction of the α strongly influences the positioning of unoccupied defect states as well es conduction states: These bands, in fact, are lowered in energy by about 1.5 eV. Notably, this energy difference matches the excitonic BSE shift computed in Ref. 208. So, we conclude that the red shift obtained by including a smaller fraction of EXX in our calculations is comparable to that obtained via the inclusion of excitonic effects. This illustrates the good agreement between the main absorption peak of previous GW+BSE[208,209] studies and ours.

In order to quantify the error bars of the PBE0-10% methodology, adequate reference data have to be identified. Unfortunately, we are not aware of any suitable experimental data. In
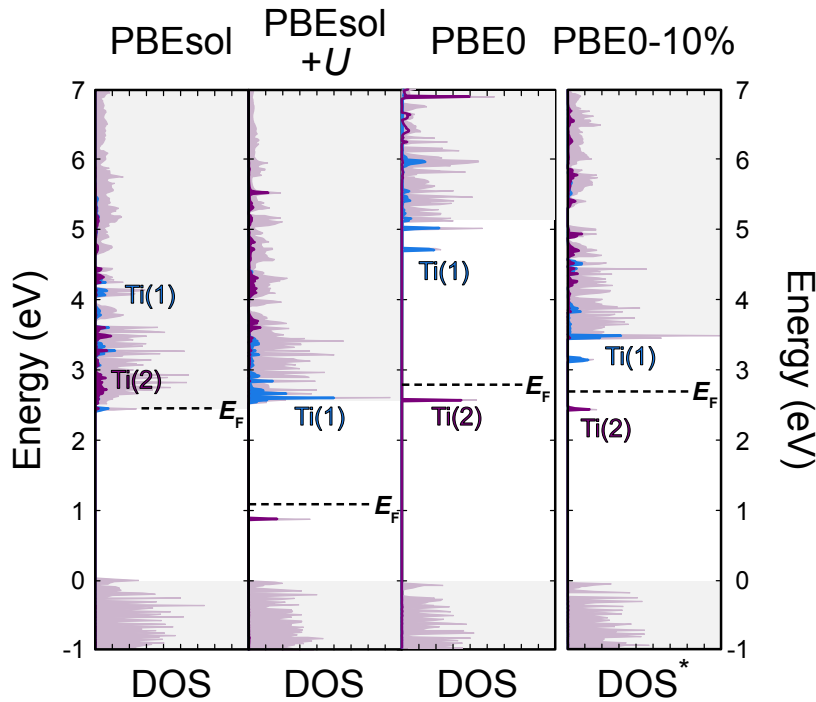

Figure 7.3: (Adapted from Ref. 210) (Renormalized) Density of states (DOS$^{(*)}$) of the vacancy $V_{O(10)}^{+1}$ under the application of different levels of theory. Under the application of the PBEsol functional, the defect-related mid-gap level can not be described. Note that for the PBE0 and the PBE0-10% calculations, we use the PBEsol+U geometry. The highlighted Ti states correspond to the Ti $3d$ states of the atoms Ti(1) and Ti(2) adjacent the O vacancy, see Fig. 7.1.
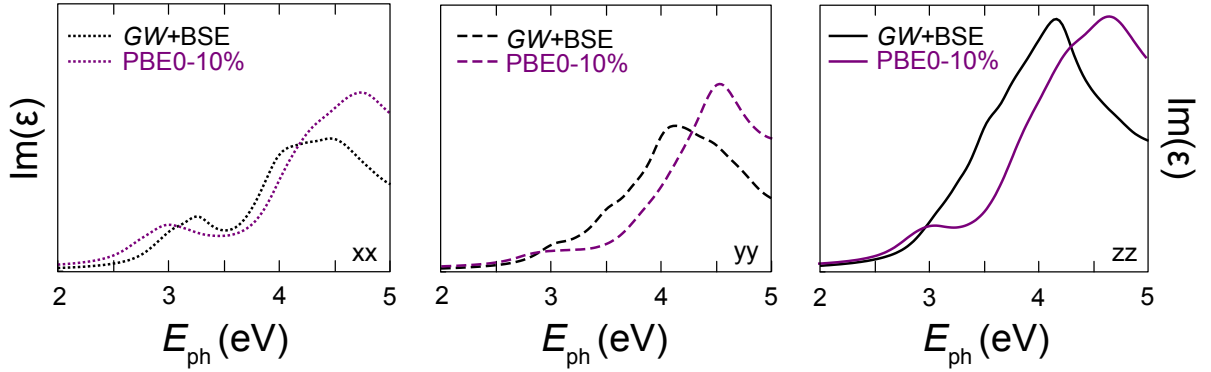
Figure 7.4: (Adapted from Ref.210) Diagonal components of the imaginary part of the dielectric function ε of the vacancy $V_{O(1)}^0$ under the application of GW+BSE (black lines), and PBE0-10% (purple lines).

fact, it is nearly impossible to experimentally resolve the absorption signatures of isolated point defects. Nevertheless, KTP features an additional O-vacancy type which shows localized defect levels already on the DFT level of theory: The vacancies V_{Ti-P}^0. Thus, the optical properties for this vacancy type can be calculated via both GW+BSE and PBE0-10%, and a comparison of both spectra would yield the required error bars. For the sake of simplicity we restrict our calculation on one non-symmetry-equivalent site (i.e., $V_{O(1)}^0$). The remaining are expected to behave similarly.

The so-calculated spectra are depicted in Fig. 7.4. In order to reduce the computational effort, the Brillouin-zone sampling for the GW+BSE spectra is reduced to a $1 \times 2 \times 1$-Γ-centered k-point mesh. This unfortunately causes a reduced resolution of the defect-related absorption. For example, the defect signatures in the zz blend into the main absorption peak. Though, some quantitative differences have to be pointed out, too. While PBE-10% overestimates the position of the main absorption peak by up to 0.5 eV with respect to the GW+BSE one, the defect signatures are red-shifted by up to 0.2 eV. Thereby, the main deviations are found for the zz component of the dielectric function. Thus, error bars expected upon the application of the PBE0-10% method are estimated by the maximum difference in peak position, i.e., up to 0.5 eV.

Still, the qualitatively good agreement suggests that PBE-10% is a valid alternative for the calculation of defect-related optical absorptions.

7.4 Absorption Properties of Oxygen Vacancies

We apply the above described PBE0-10% methodology for the computation of the optical-response properties of O vacancies featuring different charge states and spin configurations. Note that all the defect geometries have been relaxed on the PBEsol+U level of theory. The diagonal components of the so-calculated IPA spectra are depicted in Fig. 7.5. In order to better illustrate the electronic transitions upon optical excitation, the renormalized DOS* is also shown next to the corresponding spectra.

It is clearly visible that the O vacancy induces a redistribution of the oscillator strength of the main absorption peak located at about 4.5 eV. In all charge states, electronic transitions from the upper valence band into empty defect levels contribute to the forming of a shoulder located

at the low-energy side of the main absorption peak at photon energies between 3 and 4 eV. Its intensity decreases upon the formation of occupied defect levels, which cause absorption peaks for mid-gap energies: The neutral and the one-fold positively charged vacancy are characterized by absorption signatures covering the near ultraviolet and the whole visible spectrum. The vacancy $V_{O(10)}^{+2}$, on the other hand, does not feature any occupied defect level, and the Ti^{3+} generate resonances in the conduction band, so the related mid-gap absorption is missing here.

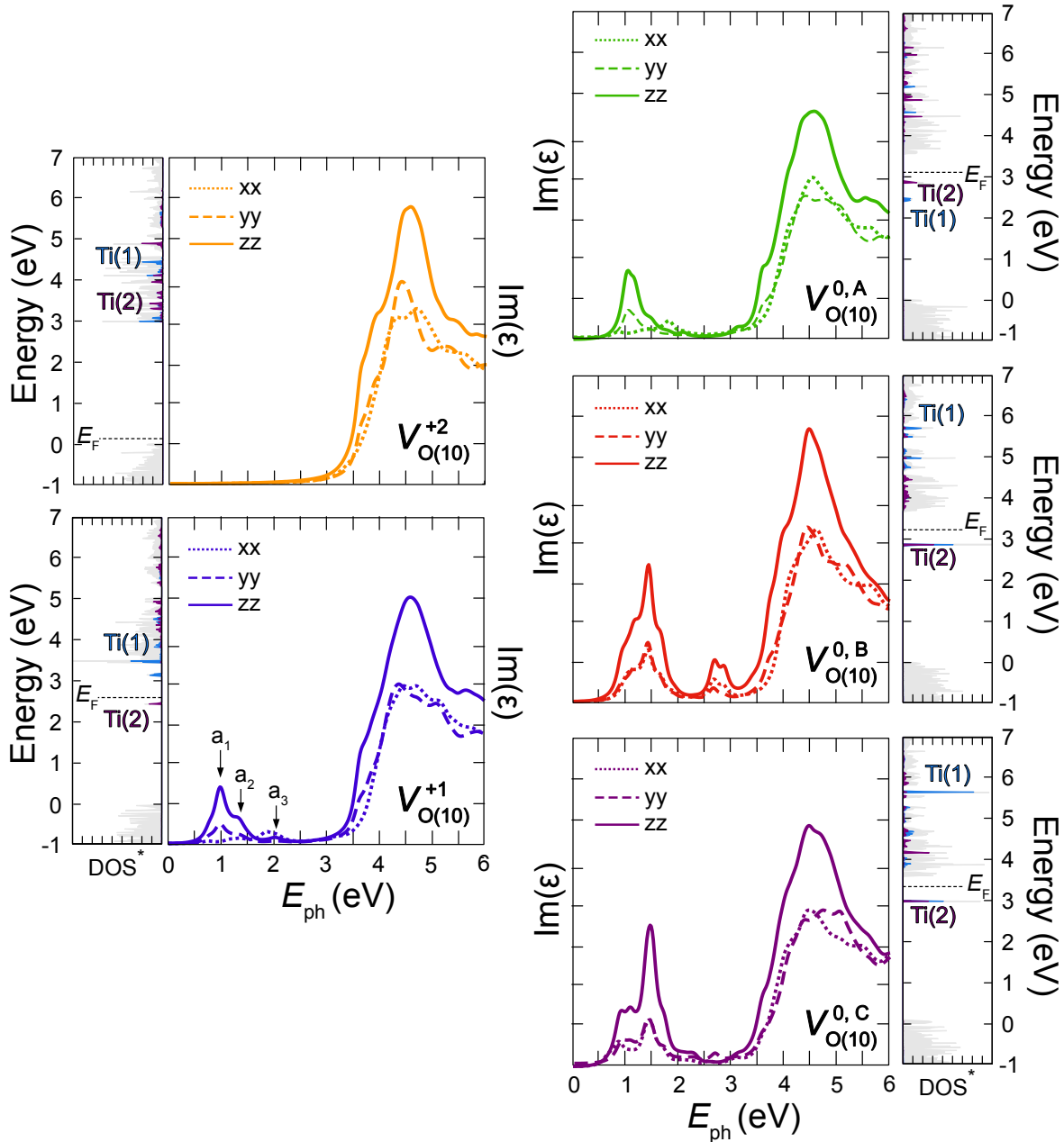Notably, the intensities of the mid-gap absorptions are strongly polarization dependent: It

Figure 7.5: (Adapted from Ref. 210) Diagonal components of $Im(\varepsilon)$ for the vacancy $V_{O(10)}$ in three different charge states (+2, +1, 0) and spin configurations. In addition, also the renormalized DOS* is shown. Within the charge states +1 and 0, the vacancy features occupied mid-gap levels, causing additional mid-gap absorption peaks.

is highest for the zz component, and it steadily decreases for yy and xx. For this reason and because the resistance against gray tracking is the poorest for laser light at 532 nm polarized along the z axis[41–43], we will discuss this polarization in more detail. Thereby, the focus will lay on the neutral and the one-fold positively charged states.

The occupied defect level of the EPR-active $V_{O(10)}^{+1}$ gives rise to an absorption band in the energy range $0.5 - 2.5$ eV. Here, three relative maxima ($a_{1,2,3}$) can be distinguished. a_1 and a_2 are generated by transitions from the occupied mid-gap level into unoccupied Ti^{3+}-related defect levels, which are located underneath the conduction band, and a_3 by transitions into the lowest conduction band.

Interestingly, the impact of the neutral vacancy strongly depends on its spin configuration. The $S = 1$ spin-triplet configuration shows similar absorption features to the charge state $+1$. This phenomenon can be explained by the relative positioning of the highest occupied defect level with respect to the conduction band. In fact, in both cases it is situated at about 0.7 eV below the conduction band and it can be attributed to the Ti(2) site near the vacancy. Thus, it could be stated that occupied Ti(1)$^{3+}$ states have a smaller impact on the KTP optical properties than the Ti(2)$^{3+}$ states. On the other hand, the two $S = 0$ spin-singlet defect geometries show even more pronounced absorption characteristics: Not only are their absorption signatures broader and higher in intensity, but they also feature additional bands in the ranges $2.4 - 3.2$ eV and $2.0 - 2.3$ eV, respectively. Their origin can be traced back to transitions from the mid-gap levels into Ti(1) $3d$ states located at about 5.6 eV (B) and 5.0 eV (C).

7.5 About the Possible Role in Gray Track Formation

In the previous section, a detailed description of the impact of $V_{O(10)}$ in different charge states has been provided. Now, these results shall be compared to experimental observations with the aim at finding some evidence for the link between the formation of O vacancy and the gray-tracking phenomenon.

First of all, it was experimentally observed that the gray-tracking affinity of KTP crystals is not isotropic along each crystal axis. Actually, its resistance is the lowest for laser beams whose polarization is parallel to the z axis.[41–43] This situation is also reflected by our data, since the impact of O(10) vacancies is the highest for the zz component of the imaginary part of the dielectric function, irrespective of the assumed charge state.

In addition, beside the anisotropic behavior, the vacancies' charge state seems to play a major role during the gray track formation. In fact, although every KTP crystal naturally features O vacancies to charge compensate for K vacancies, some crystals are less affected by gray tracking. For example, crystals with a high K-vacancy concentration are very prone to gray tracking[53,55], while those doped with Pb show a higher resistance[73,226]. The charge state assumed by the vacancy can be influenced to some extent by the Fermi-level lowering (or rising) effect of dopants. As a matter of fact, a p-type doping (e. g., Pb^{2+} substitutional cations) will result in a lowered, while an n-type doping (e. g., K vacancies) in a raised position of the Fermi level. According to Ref. 95, the charge state $+2$ (which shows nearly no mid-gap absorption) is assumed for lower Fermi-energy positions. On the other hand, the charge states causing new absorption peaks in the near infrared and visible spectrum (i. e., the one-fold positively charged and the neutral vacancy) are more likely to be assumed for Fermi levels higher than 1.5 eV. Thus, our results suggest that the resistance against gray tracking is directly connected
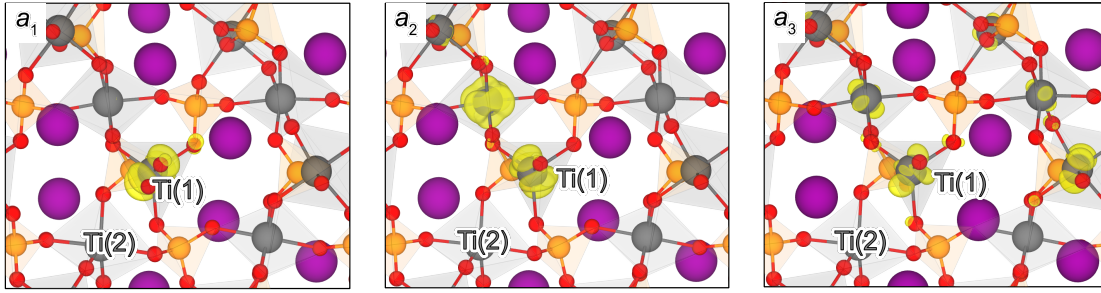
Figure 7.6: (Adapted from Ref. 210) Charge density of conduction states of the vacancy $V_{O(10)}^{+1}$. The mid-gap absorption peaks of the vacancy $V_{O(10)}^{+1}$ (i.e., $a_{1,2,3}$ in Fig. 7.5) are caused by transitions from the occupied defect level into these states.

to the presence of occupied defect levels which arise for the charges +1 and 0.

Moreover, the spectra calculated here do also allow for a more quantitative comparison with experimental data. Before the damage creation, KTP crystals are transparent for visible and near-ultraviolet light, not showing any relevant absorption during optical applications. In the initial state of gray tracking, however, it was observed that the absorption at 1064-nm (i.e., 1.17-eV) light increases[46, 227]. In the second stage of gray tracking, also the absorption of the second harmonic at 532 nm (i.e., 2.3-eV) increases[46]. Although the accuracy of PBE0-10% is to some extent restricted and the present calculations neglect thermal broadening and the motional relaxation of selection rules, our results still reflect the experimental measurements and reinforce the hypothesis that gray tracking could be related to a successive charge transition of O vacancies: Before the darkening, most $V_{O(10)}$ would assume the charge state +2. After, e.g., the creation of electron-hole pairs or the detachment of self-trapped electrons at temperatures higher 140 K[54], some of the Ti atoms near oxygen vacancies will reduce, leading to EPR-active $V_{O(10)}^{+1}$. This charge state shows characteristic absorption signatures in the range 0.8-1.3 eV, clearly matching those of the initial stage of gray tracking[46]. If the concentration of electrons is high enough, however, the oxygen vacancy may stabilize a second electron and will assume the neutral charge state. Thereby, if the spin-singlet ($S = 0$) configurations B and C are assumed, the absorption is shifted to higher energy positions (with maxima at 2.3 eV and 3.0 eV), corresponding to the absorption maxima in the energy ranges $380 - 440$ nm and $500 - 600$ nm (i.e., $2.82 - 3.26$ eV and $2.07 - 2.48$ eV, respectively), caused by the presence of laser-induced color centers[89].

The present results also fortify the hypothesis that the additional absorptions related to the gray tracking could be caused by a charge transfer in Ti^{3+}-Ti^{4+} pairs[41, 42]. In fact, the wave functions of final states of the $a_{1,2,3}$ peaks (see Fig. 7.6) visualize that optical transitions correspond to a charge transfer from Ti(2)- into Ti(1)-related states.

In addition, the relaxation of excited defect states back into their ground state could justify the presence of a luminescence band in the range between 1-1.8 eV observed by Deepthy *et al.*[228] after irradiating KTP crystals with an argon laser at 514.5 nm (i.e., 2.4 eV).

Finally, gray tracks can be cured and the transmission restored by thermal and O treatments.[43, 45, 93] Due to the thermal treatment the recombination of electron-hole pairs could be facilitated, promoting the non-absorbent charge state +2. Thus, charged O-vacancy could really be related to this early stage of photochromic damage.

7.6 Conclusions and Outlook

The optical absorption properties of charged O vacancies in KTP have been calculated. Due to the peculiar nature of strongly localized defect states, the most-established combined application of the *GW* approximation, to overcome the band-gap problem of standard DFT, and the solution of the BSE, for the inclusion of excitonic effects, is not applicable here.

Nevertheless, we show that a modification of the hybrid PBE0 functional (more precisely we reduce the fraction of EXX to 10 %) allows for emulating the effects of the *GW*+BSE method, and does lead to a good agreement with previous BSE[208,209] and experimental[81] spectra already at the IPA level of theory.

So, since the PBE0-10% does also provide a reliable description of the energetic position of defect-related mid-gap levels, it could be used to calculate the absorption properties of O vacancies at a relatively moderate computational cost.

We find that the absorption characteristics of O vacancies depend on the light polarization: Despite the charge state of the vacancy, the strongest impact is found for light polarized along the *z* axis, reflecting the experimental finding that the gray-track resistivity is the lowest for this polarization[41–43]. Moreover, also the vacancy's charge has a strong impact on the transmission properties of KTP. The weakest absorption was calculated for the charge state +2 not featuring any occupied defect level. In the one-fold positively charged state and the neutral charge states, the vacancy features occupied defect levels, whose excitation induces additional mid-gap absorptions. These are concentrated at about 1.1 eV in the case of $V_{O(10)}^{+1}$ and the neutral spin-triplet configuration $V_{O(10)}^{0,A}$. This matched the absorption characteristics of the initial stage of gray tracking[46]. For the diamagnetic neutral vacancies $V_{O(10)}^{0,B}$ and $V_{O(10)}^{0,C}$, on the other hand, also absorptions at higher photon energies are predicted, in agreement with the experimentally resolved absorption maxima induced by color centers after laser irradiation[89]. Thus, our data support the hypothesis that a consequent charging of O vacancies could be responsible for the gray track formation, i. e., the characteristic photochromic damage of KTP. The decharging of the vacancy, on the other hand, could explain, why gray tracks (at least in an early stage) are completely curable and the transparency can be restored via annealing.[43,45,93]

Nevertheless, the gray track formation in KTP crystals could involve more complex mechanisms. Despite the matching absorption characteristics, the O-vacancy model does not explain why gray tracks look like needles growing from one electrode into the crystal[45]. In fact, we would expect, at least for smaller crystals, a rather homogeneous distribution of O vacancies, and thus also of the gray color. More concretely, the role of the K sub-lattice as well as the beneficial effects of a Rb-doping during gray tracking must be further investigated and understood. For this in Chap. 8, we will investigate O vacancies in different chemical environments.

8

Gray Tracks in KTP:
New Insights into a Dark Phenomenon

Dᵁᴱ to their similar absorption features, oxygen vacancies and related related Ti^{3+} centers seem to be directly connected with the gray track formation in KTP. Nevertheless, gray track formation is complex and depends on many aspects.

In fact, a Ti^{3+} center caused by O vacancies has also been detected in RTP crystals[96], even though Rb-doped KTP crystals (RKTP) are more resistant against gray tracking[56]. So, the presence of O vacancies and associated Ti^{3+} centers alone does not provide a satisfactory explanation for gray track formation in KTP crystals and some, more complicated mechanisms are still to be investigated.

In addition, even though it provides a good agreement with former GW+BSE studies[208,209], the methodology to compute the absorption properties discussed in Chap. 7 is, to some extent, subjected to additional internal error sources. It benefits, however, from error cancellation, but the absorption properties of O vacancies could in reality differ from the absorption signatures of gray tracks.

Lastly, to the best of our knowledge, the influence of the chemical environment as well as the localization of Ti^{3+} on different Ti atoms near the vacancy has never been considered.

Thus, in this Chapter, we aim at investigating the influence of O vacancies in defect complexes. More precisely, the combination of O_{Ti-Ti} vacancies with Rb substitutional atoms and K vacancies. Thereby, we will limit ourselves to the discussion of EPR-active vacancies V_O^{+1}, so experimentally resolved hyperfine tensors[54] can be used to validate our models. In addition to the hyperfine signatures, we will also examine the energetic stability of different Ti^{3+} centers and the energy position of defect-related mid-gap levels. By this, at the end of this chapter, we will be able to formulate a revised hypothesis on the formation mechanisms of gray tracks in KTP.

8.1 Computational Details

Calculations are performed within the framework of DFT using the open-source program package QUANTUM ESPRESSO[188, 189].

EPR-active vacancies and defect complexes will be modeled within a KTP single unit cell under periodic boundary conditions. We are aware of the fact that this supercell choice could lead to unrealistically high defect concentrations (especially in the case of defect clusters[1]), but a larger supercell would result in significantly higher computational cost, and thus go beyond the scope of this study.

Experimental lattice constants $a = 12.814$ Å, $b = 6.404$ Å, and $c = 10.616$ Å[61] are used and kept fixed throughout the simulations, allowing for the simulation of quasi-non-interacting and isolated point defects. The atomic positions, on the other hand, are relaxed until variations of the total energy and residual forces are lower than 10^{-8} Ry and 10^{-4} Ry/bohr, respectively.

In Chap. 7, norm-conserving pseudopotentials treating the Ti $3d^3 4s^{0.5}$, P $3s^2 3p^3$, K $4s^1$, and O $2s^2 2p^4$ states as valence states were applied. Although these pseudopotentials lead to defect geometries, whose hyperfine signatures are in accordance with experimental data[54, 95], their application yield a fundamental band gap of only $E_{\text{Gap}} = 2.73$ eV, which strongly underestimates other DFT studies on KTP[208, 209].

Taking advantage of the work by Neufeld et al.[208], who found that the band gap of KTP can already be slightly enlarged by increasing the number of valence states attributed to the Ti atoms, we exchanged the above-mentioned Ti pseudopotential with one featuring more valence states, i. e., the Ti $3d^2 3s^2 3p^6$ states, leaving the remaining parameters unchanged. And, indeed, this procedure leads to a larger fundamental band gap of $E_{\text{Gap}}^{\text{PBEsol}} = 3.27$ eV already at the GGA level of theory.

Again, for the modeling of the O vacancies, a formalism suitable for the description of localized Ti $3d$ states is required. To avoid larger computational costs related to hybrid functionals, we will apply the Hubbard correction on top of the PBEsol[111, 112] functional during the geometry optimization and the computation of hyperfine structures. Ground-state energies as well as the energetic position of defect-related mid-gap levels will be recalculated using the PBE0[143, 144] functional with the standard fraction $\alpha = 25\%$ of EXX.

Following the methodology described in Sec. 3.5.1 for the self-consistent determination of the U parameter, we obtain the values of $U_1 = 5.91$ eV and $U_2 = 5.87$ eV for the sites Ti(1) and Ti(2), respectively. Thus, for the sake of simplicity, we will treat all the Ti equally and apply the average value $U = 5.9$ eV to all the Ti sites in the cell.

Under the application of the Hubbard correction, the band gap is further increased to $E_{\text{Gap}}^{+U} = 3.61$ eV, matching extremely well with the gap obtained with the PBE0-10% method. The increase of the band-gap width upon the application of the Hubbard correction is not surprising, since other studies have already shown that the magnitude of the Hubbard U can be tuned to match the experimental or the GW gap.[136–138]

The Brillouin-zone sampling, on the other hand, is again restricted to the Baldereschi point[190].

Other than in Chap. 7, in the following we will also investigate, how the properties of positively charged $O_{\text{Ti–Ti}}$ vacancies are influenced by the chemical environment. To this end, in ad-

---

[1]Here, we will simulate either O vacancies alone or in combination with either a K vacancy or a Rb substitutional atom. Referring the defect concentration on the number of atoms in the unit cell, this will lead to rather high defect concentrations of 1:64 or 1:32.

dition to stoichiometric KTP, we choose to simulate Rb-doped KTP (i. e., RKTP) and K-deficient KTP. Both of these are relevant for applications since KTP crystals are commonly doped with Rb to enhance their resistance against gray tracking[56], and since undoped KTP crystals are always deficient in K[70].

Since Rb substitutional atoms are far more likely to assume the lattice site K(2)[77], characterized by a larger cage volume[67], we will substitute one K(2) site with one Rb atom for the modeling of RKTP. For the K-deficient KTP, on the other hand, we will introduce one negatively charged K vacancy in the KTP unit cell, considering both nonequivalent lattice sites, i. e., $V_{K(1)}^{-1}$ and $V_{K(2)}^{-1}$. In fact, due to the high diffusion coefficients in KTP[68], both vacancy sites could be assumed. We will refer to the host materials featuring either the vacancy $V_{K(1)}^{-1}$ or $V_{K(2)}^{-1}$ as KTP-K1 and KTP-K2, respectively. Note that in the following each of these cells will be treated as if they were stoichiometric bulk cells unless they feature O vacancies.

The geometries of the four host materials are depicted in Fig. 8.1. It has to be mentioned that there is no noticeable difference between KTP and RKTP, while $V_{K(2)}^{-1}$ leads to a stronger reordering of the remaining K ions than $V_{K(1)}^{-1}$ does.

Being energetically nearly degenerate under PBEsol+U, for a comprehensive study, we will investigate both O(9) and O(10) vacancies in the four host materials just mentioned. To further validate the defect geometries, however, we will refer to the hyperfine signatures measured
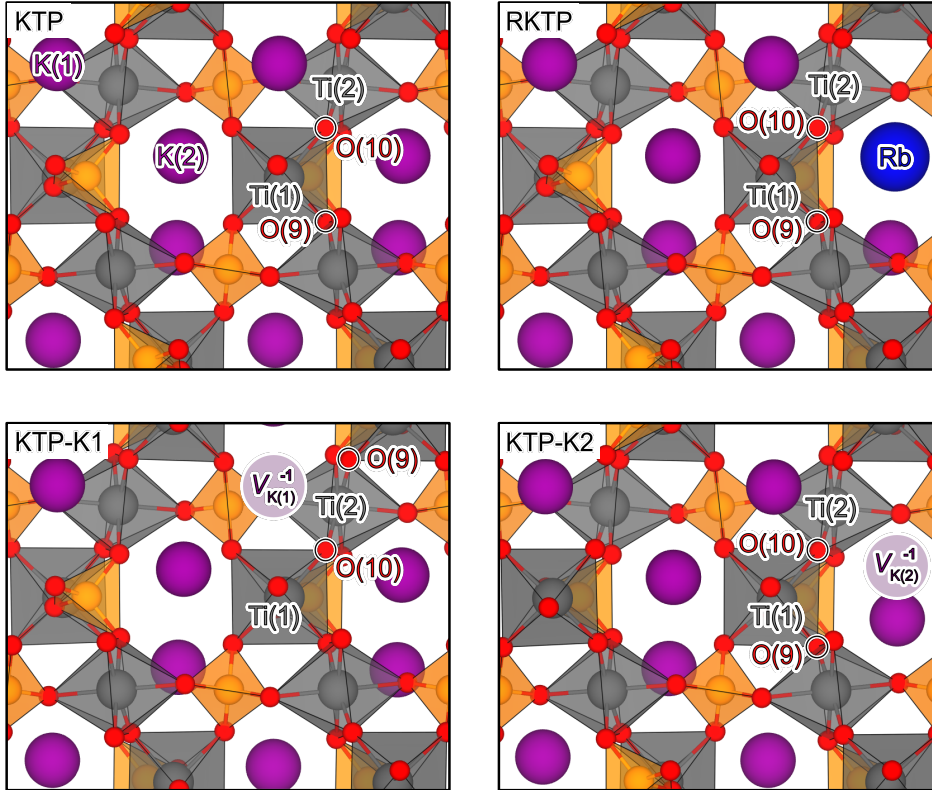

Figure 8.1: Geometries of the four host materials, i. e., stoichiometric KTP, Rb-doped KTP (RKTP), and KTP featuring the K vacancies $V_{K(1)}^{-1}$ as well as $V_{K(2)}^{-1}$ (KTP-K1 and KTP-K2, respectively). The position of the nearest atoms O(9) and O(10), which will be removed to simulate the O vacancies, are marked in each material.

by Setzler *et al.* in Ref. 54, concentrating on the thermally stable Ti^{3+} center, which has been assigned to the Ti(2) site near one O_{Ti-Ti} vacancy.

Originally, the hypothesis that reduced Ti^{3+} centers are crucial for the gray track formation was formulated due to similarities with the absorption properties of these centers in titanium-oxide-doped phosphate glasses.[43]

In this context, some considerations regarding the localization of the Ti^{3+} centers in titania have to be done. In fact, Albuquerque *et al.*[229] showed that the spacial positioning of the reduced Ti atoms upon the formation of O vacancies is not restricted to the Ti sites directly adjacent the O vacancy: Especially in fully and partially localized spin-triplet configurations, electrons are found to be energetically more stable if they are not trapped directly at the under-coordinated Ti sites adjacent the vacancy.

Thus, the investigation of effects arising from different localization sites of the defect-related Ti^{3+} center in KTP is unavoidable. In order to specifically reduce the Ti atoms surrounding the O vacancy, a two-step procedure is required: First, we will apply the Hubbard correction exclusively to the Ti atom which we want to reduce and optimize the defect geometry. Second, we will relax the structure again, applying the energy correction on all the Ti sites in the lattice. The starting points for the relaxation are thereby either the two-fold positively charged O vacancy or the bulk cell itself.

8.2　Introduction of a New Defect Model

An earlier DFT study on the hyperfine splittings of various Ti^{3+} centers in KTP crystals[95] has already showed a great agreement with the experimental tensors by Setzler and co-workers[54]. Nevertheless, some differences have to be pointed out: The DFT hyperfine structure of the nucleus $^{31}P(1)$ slightly overestimates the corresponding experimental values while $^{31}P(2)$ and $^{31}P(3)$ clearly underestimate the respective experimental data. One possible explanation for the discrepancy could be given by the presence of other (point) defects in real crystals, which have not been considered during the former theoretical investigation.

In this section, we aim at achieving a deeper understanding of the Ti^{3+} formation mechanisms in KTP crystals by investigating the influence of the chemical environment on the O vacancy formation, but also that of the localization site of the Ti^{3+} center itself. The experimental hyperfine tensors by Setzler *et al.*[54] are used again to validate our models.

The introduction of an oxygen vacancy at the sites O(9) or O(10) obviously leads to a geometry relaxation of the TiO_5 polyhedra, but also the position of the K^+ sub-lattice is affected to different extents. Interestingly, in the case of KTP and RKTP, the vacancy $V_{O(10)}^{+1}$ leads to a stronger repositioning of the K^+ ions near the vacancy than the vacancy $V_{O(9)}^{+1}$ does. In fact, the positions of the K ions vary up to 1.2 Å and less than 0.5 Å, respectively, compared to their position in the pristine (R)KTP cell.

In combination with K vacancies, on the other hand, no clear trend can be observed: The strongest repositioning is visible for the cluster composed of $V_{O(9)}^{+1}$ and $V_{K(1)}^{-1}$, the weakest for that composed of $V_{O(10)}^{+1}$ and $V_{K(1)}^{-1}$. In combination with the vacancy $V_{K(2)}^{-1}$, on the other hand, both O vacancies lead to an intermediate repositioning of the K^+ ions.

To investigate the effects arising from the site occupied by the Ti^{3+} center, we will use the Hubbard correction to selectively reduce the Ti(2) sites in the cell using the above described
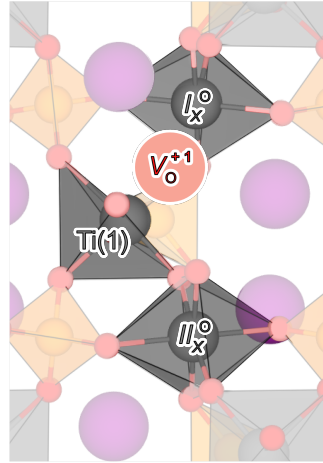
Figure 8.2: Schematic representation of the position of the two investigated $Ti(2)^{3+}$ centers, i.e., I_X^O and II_X^O, with respect to the O vacancy before geometry relaxation. I_X^O refers to the center adjacent the O vacancy, II_X^O to the next-nearest center, with X indicating the host material as defined in the text. The oxygen vacancy, on the other hand, can be located either at the site O(9) or O(10).

two-step procedure. Considering exclusively Ti^{3+} centers located at Ti(2) sites seems restrictive at the first sight. However, this choice is enforced by two main reasons: The first is that the Ti^{3+} caused by the O vacancy has been attributed unequivocally to the lattice site Ti(2) by experimental studies[54]. The second reason arises from a comparison with the behavior of another KTP isomorph, i.e., $KTiPO_4F$ studied in Ref.33: The crystal structure of $KTiPO_4F$ (KTPF) crystals corresponds to that of KTP except for the substitution of O_{Ti-Ti} atoms with fluorine (F). So, these crystals feature eight additional electrons compared to KTP due to the F substitution. Each of these extra electrons is trapped by one Ti atom in a ferromagnetic spin configuration (i.e., $S = 4$). The deintercalation of neutral K atoms from KTPF leads to the oxidation of the Ti atoms, changing their oxidation number from +3 to +4. It was found that the Ti(2) atoms do not change their oxidation state until all the Ti(1) sites have completely oxidized.[33] Consequently, upon the intercalation of K atoms in a K-deficient KTPF host, the Ti(2) sites should reduce first. Note that a similar trend was also observed in Chap. 5 for the reduction upon the intercalation of K atoms in the KTA anode material.

As already mentioned, O vacancies in KTP crystals can assume three different charge states by trapping (or, depending on the point of view, releasing) up to two electrons. In the absence of other electron traps, these electrons will be stabilized by Ti sites in the cell. Thus, in analogy with KTPF crystals, if we consider a modest quantity of electrons in KTP featuring O vacancies, we would expect them to be trapped more likely at Ti(2) sites. It has to be mentioned, however, that Setzler and co-workers[54] attributed other defect-related Ti^{3+} hyperfine signatures to Ti(1) sites. Nevertheless, since they were found to be thermally unstable[54], these findings should not contradict our assumption. Theoretically, the reduction of all Ti(2) present in the cell featuring one O vacancy should be investigated to analyze how the distance of the O vacancy from the reduced Ti atom influences the stability and the energetic positioning of the defect-related mid-gap level. However, some attempts in obtaining fully localized states with the electron localized in the TiO_6 spiral not featuring the O vacancy were not successful.
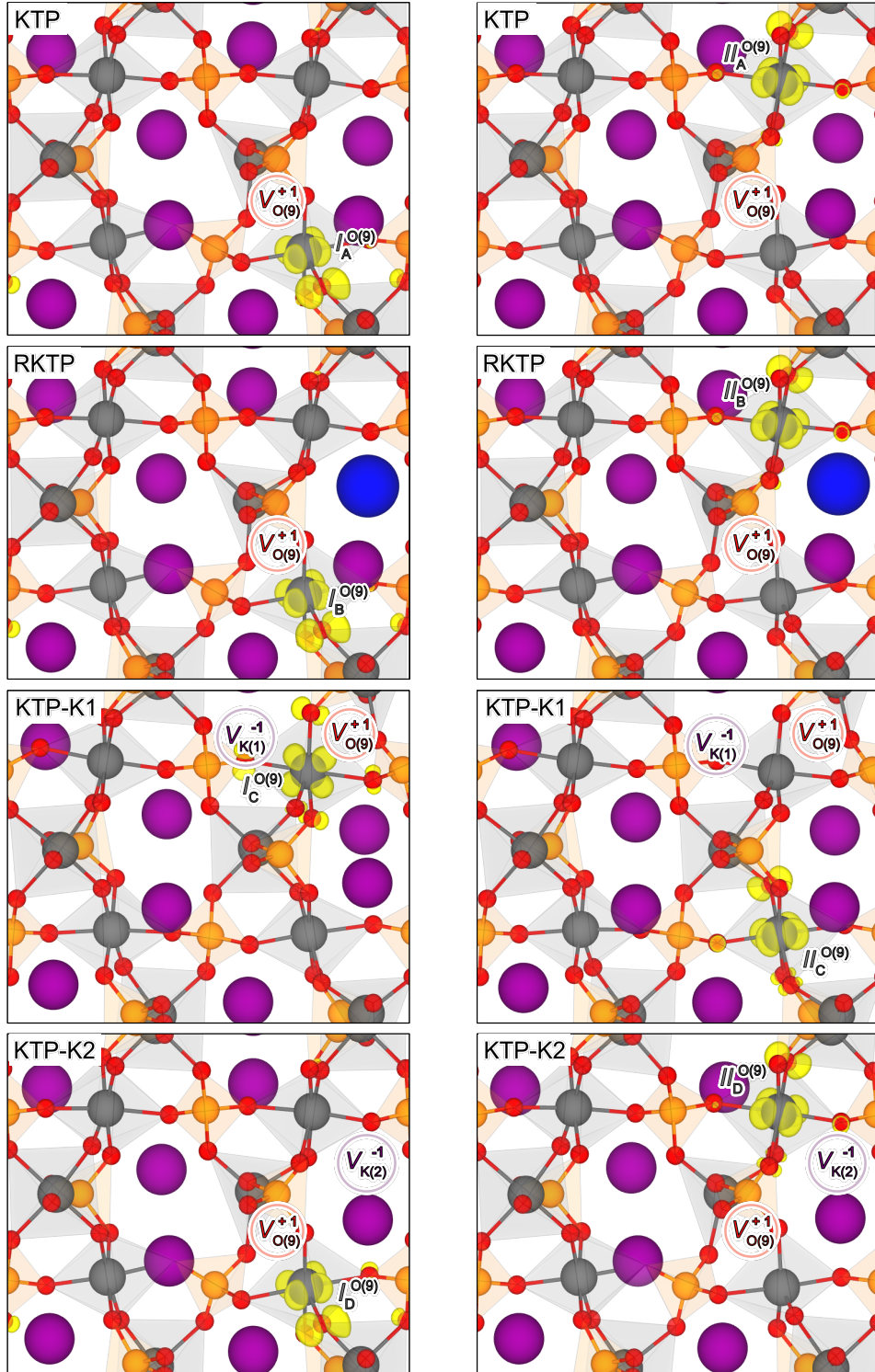
Figure 8.3: The geometries of the centers $I_X^{O(9)}$ adjacent to the O(9) vacancy are depicted on the left, the next-nearest centers $II_X^{O(9)}$ on the right. The yellow isosurfaces correspond to the charge density of the occupied defect levels. Note that due to the different positioning of the O(9) vacancy in KTP-K1, the positions of $I_C^{O(9)}$ and $II_C^{O(9)}$ deviate compared to the remaining cells.
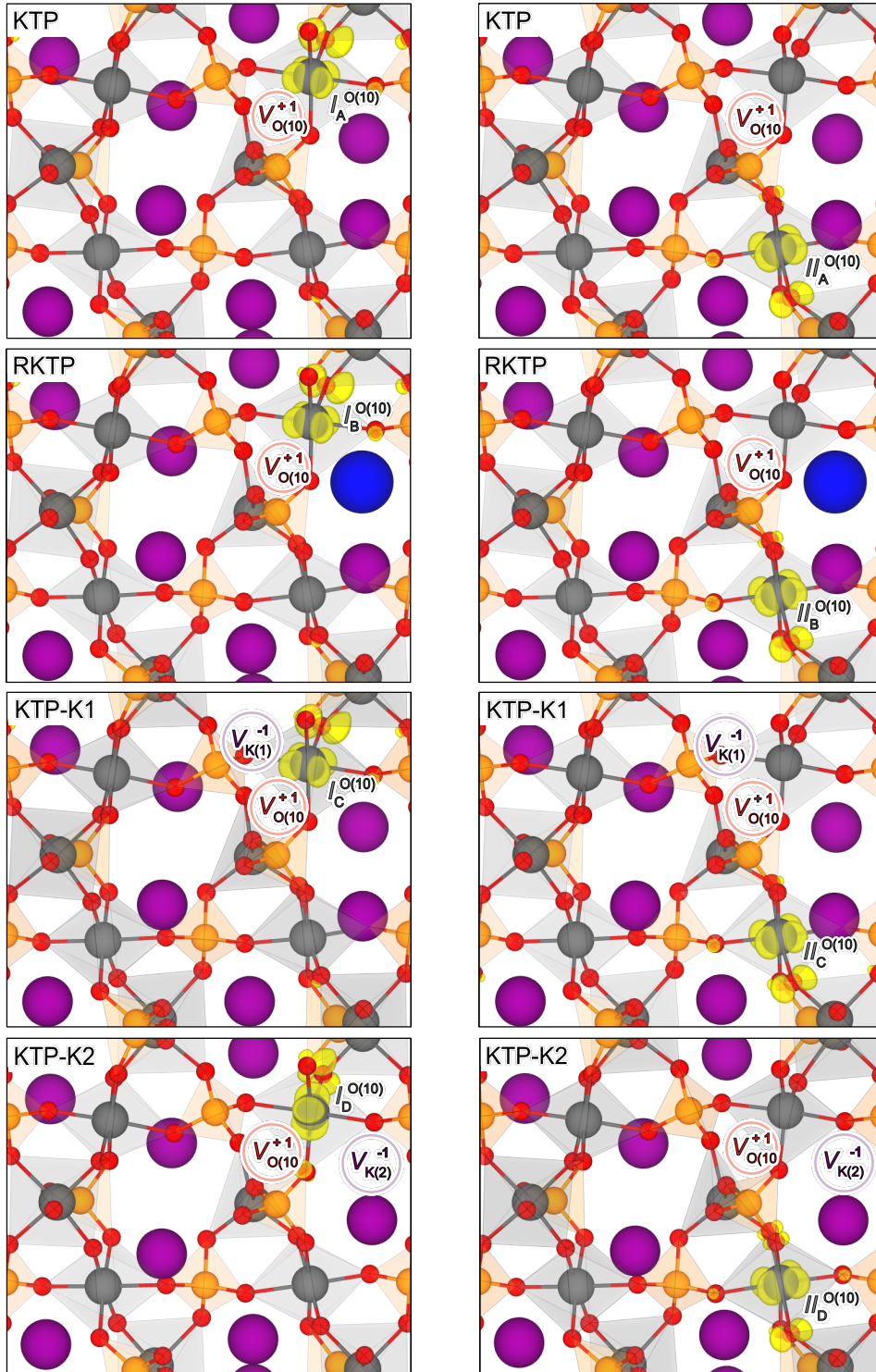
Figure 8.4: The geometries of the centers $I_X^{O(10)}$ adjacent to the O(10) vacancy are depicted on the left, the next-nearest centers $II_X^{O(10)}$ on the right. The yellow isosurfaces correspond to the charge density of the occupied defect levels.

We expect that the modeling of Ti^{3+} centers located far from O vacancies requires either hybrid functionals or a larger supercell corresponding to a KTP unit cell doubled along the c axis. However, this would lead to higher computational costs and therefore go beyond the scope of this work. Thus, we will limit ourselves to the investigation of the Ti^{3+} centers located at the Ti(2) directly adjacent the O_{Ti-Ti} vacancy and the next-nearest Ti(2) in a KTP unit cell. In the following, these centers will be referred to as I_X^O and II_X^O, respectively, where the index $X \in \{A, B, C, D\}$ indicates the host material with A = KTP, B = RKTP, C = KTP-K1 and D = KTP-K2. The O indicates the position of the O vacancy, i.e., either O(9) or O(10), see Fig. 8.2.

A schematic representation of all studied $V_{O(9)}^{+1}$ and $V_{O(10)}^{+1}$ geometries can be found in Figs. 8.3 and 8.4, respectively. The yellow isosurfaces correspond to the charge density of the occupied defect level and thus indicates the position of the Ti^{3+} center.

The hyperfine tensors calculated for all the above described defect configurations are compiled in Tab. 8.1. Note that only centers with significant splittings are shown and that the $^{31}P(i)$ nuclei do not necessarily correspond to the same P atom in each cell.

We will first discuss the centers modeled in stoichiometric KTP, starting with the center caused by the vacancy at the site O(10), which has already been proposed[95] to be responsible for the formation of thermally stable Ti^{3+} centers, i.e., $I_A^{O(10)}$.

The here calculated hyperfine tensors of the center $I_A^{O(10)}$ are in good agreement with those reported in Ref. 95, but show some qualitative differences:

(i) The splittings of the nucleus $^{31}P(2)$ are clearly higher than those previously calculated, and therefore closer to the experiment[54];

(ii) Also, the splittings of the nucleus $^{31}P(3)$ are slightly higher, but still underestimate the experimental findings;

(iii) The splittings of the nucleus $^{31}P(4)$, on the other hand, are found to deviate stronger from the experimental data.

Interestingly, however, the hyperfine signatures of the center $II_A^{O(10)}$ located at the next-nearest Ti(2) atom is even closer to the experimental data[54]. This holds especially for the splittings of the nuclei $^{31}P(3)$ and $^{31}P(4)$, both showing overall larger components and thus a better agreement with the experiment[54].

Regarding the centers caused by the vacancy at the site O(9) in KTP, it is evident that only the center $II_A^{O(9)}$ provides comparable values to the experiment, although the second-largest interactions with the ^{31}P are slightly underestimated and only qualitatively in good agreement. In a first attempt, the different behavior of the centers $I_A^{O(9)}$ and $I_A^{O(10)}$ could be explained by differences in the distance between each Ti^{3+} center and the interacting ^{31}P nuclei.

The Rb substitution does not show a strong influence on the hyperfine signatures of the O-vacancy-related Ti^{3+} centers. In fact, each center identified in KTP can also be found in RKTP. This is not surprising, since there is experimental evidence that the same O-vacancy-related Ti^{3+} center in KTP is also present in RTP crystals, see Ref. 96.

Finally, some considerations about the vacancy clusters will follow: First, again the centers $II_{C,D}^{O(9,10)}$ lead to a better agreement with the experimental study by Setzler and co-workers[54] than the centers $I_{C,D}^{O(9,10)}$ do. This is most evident for the the nuclei $^{31}P(3)$ and $^{31}P(4)$. Second,

Table 8.1: Absolute values of the hyperfine tensors (in MHz) of the Ti^{3+} centers of positively charged O(9) and O(10) vacancies in different host materials. The indices A, B, C and D refer to KTP, RKTP, KTP-K1 and KTP-K2, respectively. For a better comparison, the experimental values of the O-vacancy-related Ti^{3+} center in KTP[54] are reported, too. Note that the experimental tensors are sorted in descending order, the DFT values of A_1, A_2, and A_3 correspond to their exact attribution.

$V^{+1}_{O(9)}$	KTP Expt.[54]	KTP		RKTP		KTP-K1		KTP-K2	
		$I_A^{O(9)}$	$II_A^{O(9)}$	$I_B^{O(9)}$	$II_B^{O(9)}$	$I_C^{O(9)}$	$II_C^{O(9)}$	$I_D^{O(9)}$	$II_D^{O(9)}$
^{31}P(1):									
A_1	16.58	31.342	18.850	32.059	18.903	25.394	22.030	26.822	21.103
A_2	16.75	30.620	18.384	31.328	18.472	24.312	21.623	26.151	20.658
A_3	23.36	35.627	24.669	36.395	24.859	32.107	28.222	31.180	27.199
^{31}P(2):									
A_1	14.28	12.476	12.789	11.508	12.422	19.642	7.867	12.937	9.714
A_2	14.68	12.048	12.250	11.066	11.911	18.428	7.433	12.449	9.252
A_3	21.37	17.592	18.650	16.529	18.265	27.195	13.271	18.428	15.258
^{31}P(3):									
A_1	3.74	1.585	5.548	1.063	6.514	0.146	7.080	1.579	5.342
A_2	4.24	0.179	4.489	0.331	5.453	1.364	5.892	0.265	4.266
A_3	7.23	3.399	8.357	2.793	9.449	2.141	10.035	3.466	8.102
^{31}P(4):									
A_1	0.84	0.108	2.806	0.257	2.964	0.815	2.599	0.782	1.149
A_2	1.40	1.205	1.682	1.336	1.837	0.484	1.340	1.819	0.052
A_3	3.94	1.453	5.406	1.294	5.626	2.678	5.219	0.777	3.540

$V^{+1}_{O(10)}$	KTP Expt.[54]	KTP		RKTP		KTP-K1		KTP-K2	
		$I_A^{O(10)}$	$II_A^{O(10)}$	$I_B^{O(10)}$	$II_B^{O(10)}$	$I_C^{O(10)}$	$II_C^{O(10)}$	$I_D^{O(10)}$	$II_D^{O(10)}$
^{31}P(1):									
A_1	16.58	21.290	19.475	21.698	18.438	23.033	26.348	19.980	19.910
A_2	16.75	20.831	19.165	21.245	18.172	22.372	25.974	18.815	19.762
A_3	23.36	26.161	25.742	26.588	24.713	27.495	33.086	27.583	26.368
^{31}P(2):									
A_1	14.28	17.692	16.751	17.307	17.271	14.945	13.689	15.423	11.303
A_2	14.68	17.224	16.510	16.884	17.046	14.474	13.515	14.057	11.054
A_3	21.37	23.489	23.104	23.198	23.725	20.273	19.562	20.248	16.748
^{31}P(3):									
A_1	3.74	2.983	5.493	3.190	5.581	2.372	4.447	0.048	7.225
A_2	4.24	1.549	4.399	1.722	4.461	0.859	3.231	1.357	6.036
A_3	7.23	5.123	8.317	5.336	8.417	4.466	7.173	2.128	10.243
^{31}P(4):									
A_1	0.84	1.603	1.883	1.722	2.290	1.654	2.526	0.631	2.769
A_2	1.40	2.760	0.698	2.865	1.089	2.860	1.194	0.912	1.512
A_3	3.94	0.168	4.116	0.292	4.578	0.368	4.660	2.486	5.404

the hyperfine structures caused by the combination of a K vacancy with an O vacancy are all qualitatively similar.

However, comparing the hyperfine splittings of the ^{31}P nuclei with the largest splittings, it is visible that the values of ^{31}P(1) overestimate and those of ^{31}P(2) underestimate the respective experimental data to different degrees in all the examined cases. This finding, however, could be related to the chosen supercell size and the consequent unreasonably high defect concentration. To exclude this scenario, a larger supercell is required. This would also allow for the investigation of effects related to the distance between the K and the O vacancies.

A comparison of the defect geometries suggests that the differences in the hyperfine structures of the defect complexes can not be explained only with the different distances between the relevant ^{31}P atoms and the Ti^{3+} center: The centers $II_C^{O(10)}$, and $II_D^{O(10)}$, for example, differ with respect to their hyperfine signatures, but correspond to the exact same Ti site. In addition, also the geometries of the vacancy $V_{O(10)}^{+1}$ in KTP-K1 ($II_C^{O(10)}$) and KTP-K2 ($II_D^{O(10)}$) are very similar except for the position of one K$^+$ ion near the O vacancy. In fact, as already mentioned, the repositioning of the K$^+$ ions is weaker for $V_{O(10)}^{+1}$ in KTP-K1 than in the case of $V_{O(10)}^{+1}$ in KTP-K2. So, the hyperfine structure is also influenced by the K sub-lattice.

To sum up, despite different chemical environments, all the investigated O vacancies lead to a good agreement with experimental hyperfine tensors, but our data suggest that the previous defect model, which consists of a Ti^{3+} adjacent a O$_{Ti-Ti}$ vacancy[54,95,96], has to be partially revised by shifting the reduced Ti atom to the next-nearest Ti(2).

Due to the quantitatively better agreement with the experiment, however, we are still more prone to attribute the thermally stable Ti^{3+} center to the vacancy $V_{O(10)}^{+1}$ rather than the vacancy $V_{O(9)}^{+1}$. Nevertheless, we note that the center resolved by the experiment could also be attributable to defect clusters composed of one O$_{Ti-Ti}$ and one K vacancy. The Ti^{3+} centers, however, are expected again to be localized at the next-nearest Ti(2) rather than at the under-coordinated Ti(2) adjacent the O vacancy.

8.3 Discussion and Outlook

In the previous section, it has been shown that the agreement of O-vacancy-related hyperfine splittings can be enhanced by shifting the Ti^{3+} center from the Ti(2) site adjacent the vacancy to the next-nearest Ti(2) atom. However, is this modified defect model also energetically more favorable compared to the previous model?

We will see that this is in fact true, but before we have to stress on the following points. First of all, it has to be pointed out that the DFT+U formalism is largely applied during the geometry optimization and it does indeed lead to realistic defect models, but the energy position of defect-related mid-gap levels strongly depends on the value attributed to the Hubbard correction. We expect the application of hybrid functionals to be beneficial in solving this issue, since these functionals provide a reliable description of the position of defect states[221–223].

In addition, one could suppose that, as shown in Chap. 7, a partial compensation of excitonic and local-field effects could be achieved by a customized fraction of EXX, leading to the computation of realistic optical properties. However, due to the larger DFT band gap (caused by the additional Ti valence states), the PBE0-α methodology is not applicable here: The application of the PBE0 functional with the standard fraction of $\alpha = 25\%$ leads to a fundamental

Table 8.2: Differences of the PBE0 ground-state energy of the centers I_X^O and II_X^O caused by the same O vacancy in each host material X.

Host	KTP (A)		RKTP (B)		KTP-K1 (C)		KTP-K2 (D)	
O vacancy	$V_{O(9)}^{+1}$	$V_{O(10)}^{+1}$	$V_{O(9)}^{+1}$	$V_{O(10)}^{+1}$	$V_{O(9)}^{+1}$	$V_{O(10)}^{+1}$	$V_{O(9)}^{+1}$	$V_{O(10)}^{+1}$
ΔE [meV]	+241	+164	+223	+166	+291	+146	+247	+188

band gap width of $E_{KTP}^{PBE0} = 5.39\,eV$, overestimating by about $160\,meV$ the *GW* band gap of Neufeld *et al.*[208]. In order to emulate the excitonic red shift, the fraction of EXX has to be reduced to about 6%. Unfortunately, this small fraction of EXX does not shift the defect level's position of each defect cell in the same way and their relative position (with respect to the valence band maximum) deviates from those obtained via the standard PBE0. So, since we are not able to judge, if the position of the defect levels after the reduction of the fraction of EXX is reliable or not, the solution discussed in Chap. 7 has to be discarded in this case.

The second consideration involves the calculation of the formation energy of O vacancies themselves. Normally, during the investigation of charged point defects, two approaches are established to level out effects attributable to different charge states. One is the application of energy corrections (see for example Ref. 230) to align the energy of the stoichiometric cell to that of the cell featuring defects, being therefore subjected to additional error sources. Another one, holding the advantage of not requiring any energy correction, is the Slater-Janak transition state model[139,212]. This, however, would require the computation of all possible charge states of the vacancy, leading unfortunately to several additional simulations because of the neutral vacancy. In fact, we would have to revise the geometries at least of its paramagnetic spin configurations discussed in the Chap. 7, and first determine, at which Ti site the second electron would be trapped.

Nevertheless, it is still possible to judge the stability of one configuration by comparing the ground-state energies of cells of the same stoichiometry: The lower the value, the more favorable the configuration is to be assumed[2]. For a better comparability between structures of different stoichiometries, however, we will not discuss directly the PBE0 ground-state energy of different structures, but the energy differences between cells featuring the same number of atoms of the same species. More precisely, we will (i) determine, which of the centers I_X^O and II_X^O are the most favorable to be assumed for each studied case and (ii) discuss how the O-vacancy site and the chemical environment influences the energy position of related mid-gap defect levels.

The energy differences are calculated as

$$\Delta E = E_I - E_{II}, \tag{8.1}$$

where E_I and E_{II} correspond to the PBE0 ground-state energy of the cells featuring the centers I_X^O and II_X^O, respectively. The so-calculated values are reported in Tab. 8.2.

Notably, all the energy differences ΔE happen to be positive. This means, that in all exam-

---

[2]Note that the ground-state energies of stable systems are always negative

ined cases the center II_X^O (i.e., the center located at the next-nearest Ti(2) and in better agreement with the hyperfine signatures by Setzler *et al.*[54]) is in fact energetically more favorable than the center I_X^O directly adjacent the O vacancy. This trend is most pronounced if the O vacancy is located at the site O(9).

As we have already mentioned before, the K^+ sub-lattice seems to influence the hyperfine structure of the Ti^{3+} centers. So, we tried to figure out, if there is some relation between the centers I_X^O and II_X^O and the surrounding K^+ suitable to explain, why II_X^O is always energetically more stable than I_X^O. We found that (apart from the different coordination number) the two Ti sites differ with respect to their distance to the next K^+ ion $\left(\overline{KTi^{3+}}\right)$. More precisely, the center II_X^O is located by an average of 0.19 Å closer to a K^+ ion than the I_X^O modeled in the same cell, see Tab. 8.3. So, the Ti^{3+} centers seem to be stabilized by electrostatic forces between the positively charged K^+ ion and the trapped electron.

Having a closer look on the entries in Tab. 8.3, it is notable that in the case of $V_{O(10)}^{+1}$ in KTP-K1 also the center $I_C^{O(10)}$ is characterized by a rather small distance to the next K^+ ion, while for the same vacancy in KTP-K2 the difference is not as pronounced. Interestingly, $V_{O(10)}^{+1}$ also generates the energetically most stable Ti^{3+} center caused by defect complexes, i.e., $II_C^{O(10)}$.

The energetic position of each defect level with respect to the lowest unoccupied state of the centers II_X^O are compiled in Tab. 8.4. For a better discussion, this value has been determined not only within the PBEsol+U formalisms, but also using the PBE0 hybrid functional. Due to the problematics discussed above, we will refrain from a detailed quantitative discussion of defect-level induced absorption peaks. Still, some qualitative trends shall be pointed out.

First of all, the values of $E_{\text{Def.}}^{\text{PBEsol}+U}$ and $E_{\text{Def.}}^{\text{PBE0}}$ deviate less than 0.3 eV from each other. We note that in the case of the I_X^O-related defect levels, the deviation between PBEsol+U and PBE0 is even smaller, both yielding energy differences in close agreement with the PBE0 values reported in Tab. 8.4.

Second, the Rb doping only shows a minor impact on the energy position of the defect level, while the K vacancy slightly shifts them towards higher energies.

In Chap. 7, we have drawn a possible link between gray tracking and the absorption signatures of O vacancies. The energetic positions of the defect levels with respect to the lowest unoccupied state calculated here seem, however, too large to support this hypothesis. In fact,

Table 8.3: Distances between the Ti^{3+} centers I_X^O and II_X^O and the nearest K^+ ion.

	KTP		RKTP		KTP-K1		KTP-K2	
	$I_A^{O(9)}$	$II_A^{O(9)}$	$I_B^{O(9)}$	$II_B^{O(9)}$	$I_C^{O(9)}$	$II_C^{O(9)}$	$I_D^{O(9)}$	$II_D^{O(9)}$
$\overline{KTi^{3+}}$ [Å]	3.75	3.63	3.75	3.61	3.87	3.55	3.82	3.57
	$I_A^{O(10)}$	$II_A^{O(10)}$	$I_B^{O(10)}$	$II_B^{O(10)}$	$I_C^{O(10)}$	$II_C^{O(10)}$	$I_D^{O(10)}$	$II_D^{O(10)}$
$\overline{KTi^{3+}}$ [Å]	3.87	3.63	3.86	3.63	3.66	3.55	3.88	3.74

Table 8.4: Energy position of the occupied defect level with respect to from the lowest unoccupied state using both the PBEsol+U and the PBE0 functional.

	KTP		RKTP		KTP-K1		KTP-K2	
	$II_A^{O(9)}$	$II_A^{O(10)}$	$II_B^{O(9)}$	$II_B^{O(10)}$	$II_C^{O(9)}$	$II_C^{O(10)}$	$II_D^{O(9)}$	$II_D^{O(10)}$
$E_{\text{Def.}}^{\text{PBEsol}+U}$ [eV]	3.17	3.10	3.14	3.09	3.04	2.96	3.09	3.01
$E_{\text{Def.}}^{\text{PBE0}}$ [eV]	2.98	2.92	2.97	2.88	2.77	2.85	2.84	2.79

considering that the PBEsol+U band gap calculated here already matches the PBE0-10% band gap discussed in Chap. 7, the energetic position of the defect level (i. e., about 3 eV below the lowest unoccupied defect level irrespective of the used functional) could be a reasonable (first) estimation for the first excitation energy. In addition, this level might also not be directly excited by the second harmonic radiation of 2.3 eV (i. e., 532 nm).

Nevertheless, we still expect O vacancies to be essential for the early stage of gray tracking, since they provide a stabilizing force for photo-electrons causing thermally stable Ti^{3+} centers. More precisely, the band-gap edge of KTP is located at about 350 nm (i. e., about 3.54 eV). So, two-photon processes involving the fundamental and the second-harmonic radiation (which have already been found to cause the formation of color centers in KTP[42]) can lead to the formation of electron-hole pairs, which are then stabilized by defects, i. e., O and K vacancies, respectively. However, and this is the eventually the most important result of our investigation, our data suggest that the formation of thermally stable Ti^{3+} centers is the product of a two-step process: First, the formation of an O_{Ti-Ti} vacancy leads to a displacement of surrounding K^+ ions. Second, electrons released either by the O vacancy itself or by other processes are trapped by Ti(2) sites and stabilized by electrostatic forces caused by a nearby K^+, forming a bound polaron. Thereby, the electron trap is not located at the undercoordinated Ti(2) next to the oxygen vacancy, but rather at the next-nearest Ti(2) atom.

However, we propose that the formation of O-vacancy-related Ti^{3+} centers alone does not provide a valid and satisfactory explanation of the gray track formation in KTP. In fact, since the O-vacancy-related hyperfine signatures have also been detected in RTP crystals[96] and although irradiated RTP crystals also assume a light gray coloration[96], a small Rb doping is beneficial to enhance the gray-track resistance of KTP crystals[45,56].

In addition, we believe that the trapped electron could follow the migration of the K^+ along the c axis, which is promoted for example by the application of dc electric fields or laser irradiation (see Sec. 2.3), thus leading to areas with an unusually high concentration of these bound polarons. We propose that gray tracks could correspond to exactly these areas showing a surplus of K^+ ions which, together with their accompanying Ti^{3+} electron trap, cause additional mid-gap absorptions and thus the characteristic coloration, see Fig. 8.5. For an easy test, we model one neutral K interstitial in the KTP unit cell. The valence electron is trapped by the closest Ti(2) atom, leading to a reduced Ti^{3+} center and its related mid-gap defect level. The energy position of this level is located at 2.68 eV and 2.50 eV under the application of PBEsol+U and PBE0, respectively. They are thus located closer to the conduction band compared to the

O-vacancy-related defect states. Therefore, we expect that they could be directly excited by the second harmonic at 2.3 eV.

Our model can, thus, be seen as an amplification of the one by Mürk *et al.*[48]: In their model, gray tracking is characterized by two stages of coloration. The first corresponds to the recharging of (not-further specified) preradiational defects and the second to the creation of new defects caused by the radiation itself. The origin of the crystal coloration was thereby attributed to electron-hole pairs stabilized by K_i^+ causing Ti^{3+} and O atoms acting as hole traps, respectively. In addition, they found a thermal treatment enhancing the rigidity of the K sublattice to be beneficial in preserving the transparency of KTP crystals upon the irradiation with X rays.

Moreover, Mu and Ding in Ref. 57 have already discussed the displacement of K^+ ions along [001], or rather the separation of K^+ and V_K^-, in the context of gray tracking. Contrary to other authors[41–43], who indicated the highest gray-track susceptibility for light polarized along [001], however, Mu and Ding found that gray tracks showing their characteristic colorations can only form upon the irradiation with laser light (at 514.5 nm) perpendicular to [001]. For light polarized parallel to [001], on the other hand, only invisible damage was resolved. The visible damage, i. e., orange dots and dark traces, was explained by the formation of Fe^{3+} ions acting as hole traps and reduced Ti^{3+} centers, respectively. The invisible damage was attributed to a displacement of K^+ ions along [001], thereby indicating the photogalvanic effect as the origin of both types of damage. The photogalvanic effect was also already proposed by Alexandrovski *et al.*[46] to explain the gray track formation, in analogy with the photorefractive damage in lithium niobate ($LiNbO_3$).

In Ref. 45, gray tracks caused by the application of high-voltage pulses along the *c* axis were described as needles which form at one electrode and grow into the crystal towards the opposite electrode. In addition, it was found that gray-tracked areas show a reduced ionic
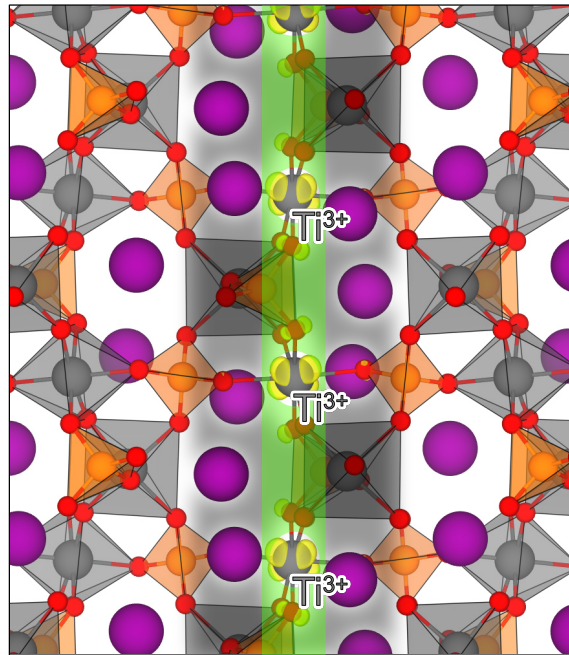

Figure 8.5: Schematic representation of the gray track formation upon laser irradiation.

conductivity. In our model, the needles could be explained by overpopulated K-ion migration channels (see Fig. 8.5), which hinder the migration of the K via vacancy hopping mechanisms, thus reducing the ionic conductivity.

On the other hand, it has also been shown that thermal annealing in nitrogen atmospheres leads to a thermal decomposition of the surface, which corresponds to the loss of K[62, 231] and P[231]. Notably, the deterioration of the surface expressed itself as a translucent layer, whose removal upon cooling results in a transparent crystal[62]. In addition, it was stated that the loss of K and P promotes the annealing of bulk defects in the crystal, thus restoring their transparency[231].

Finally, our model may also explain why KTA is less affected by gray tracking[58] than KTP and why a Rb-doping is beneficial to prevent the gray tracks to form in KTP: Due to the larger volume of the AsO_4 tetrahedra, the K intercalation sites in KTA are located at different positions than in KTP (see Chap. 5), which might reduce the stabilizing forces of the Ti^{3+} centers. Regarding the Rb doping, the higher activation energies for the Rb migration[45] simply prevent the accumulation of bound polarons.

We expect that our work is instrumental to clarify the formation mechanisms of gray tracks and paves the way for further experimental and theoretical investigation. In fact, at this point it appears to be unavoidable to:

1. Verify (for example by concentration measurements), if gray tracked areas really show an enrichment in K.

2. Further deepen the knowledge on the interplay of delocalized K^+ and Ti^{3+}, especially with regard to the migration mechanisms of the K^+. More precisely, it is still to be investigated if the O-vacancy-related Ti^{3+} follows the migration of the displaced K^+ ion (i. e., a bound polaron), or if the position of the O-vacancy-related Ti^{3+} is not affected by the ion migration. Nevertheless, in the latter scenario the so-forming K_i^+ could cause additional Ti^{3+} centers far away from the V_O^{+1}-V_K^{-1} complexes.

9

Concluding Remarks

$\mathbf{I}$N this thesis, various properties of KTP-type crystals have been investigated in the framework of density functional theory. A major focus was laid on the investigation of the effects caused by defects in the crystal lattice, aiming at further clarifying the complex phenomenon of gray track formation in KTP. In addition, the electrochemical performance of KTA crystals has been studied. A series of conclusions can be drawn from our results.

Towards KTA electrodes and beyond   To investigate the electrochemical properties of KTA, we simulated the charging of a K-ion battery. Thereby, K-intercalation and K-deintercalation mechanisms in the anode and cathode material were achieved by modeling $KTiOAsO_4K_x$ and $K_{1-x}TiOAsO_4$, respectively.

To evaluate the performance of KTA electrodes, we determined (i) the average voltages upon different concentrations of (de)intercalated K, (ii) the corresponding lattice deformations, and (iii) the energy barriers for the K ion (K vacancy) migration. Thereby, the Hubbard correction was applied to achieve an accurate description of redox potentials.

Our results are promising, since they suggest that KTA batteries could be characterized by high average voltages, modest volume deformations and relatively low activation energies for the alkali-ion (alkali-vacancy) migration. However, it has to be pointed out that the suitability of KTA for electrochemistry is not superior (apart from slightly higher average voltages) compared to KTP. In addition, KTA holds the disadvantage of containing the toxic element arsenic.

At the beginning of the thesis, we motivated this part of our investigation by the fact that KTA shows a higher resistivity of KTA compared to KTP against the gray track formation. This phenomenon is in fact related to stable trapped electrons and could thus also be detrimental for electrochemical applications. Nevertheless, referring to our revised gray-track model, we expect that trapped electrons (i.e., Ti^{3+} centers) will follow the migration of K^+ ions and the electronic flux should (at least in theory) not be affected.

Are our results therefore deprived from any relevance? The answer is certainly no. In fact, we showed that the electrochemical performance of KTP-type crystals is not significantly influenced by the group-V element included in the XO_4 tetrahedra. This allows for further modifications and optimizations of the crystal structure by substituting the X sites. More precisely, the substitution of As with, e.g., silicon (Si) could be promising, as this element is non-toxic and

largely available in the Earth's crust. Due to the similar atomic radii, the replacement should theoretically be possible, but might require a fluorine (F) doping to compensate for the missing valence electron.

Absorption features of oxygen vacancies in KTP   The computation of realistic absorption properties of oxygen vacancies and related Ti^{3+} centers required an unconventional approach to (partially) compensate for quasiparticle as well es excitonic effects. O vacancies provide the stabilizing force for up to two electrons, which are trapped by Ti atoms surrounding the vacancies. This leads to the formation of Ti^{3+} centers and related mid-gap defect states. Since these states are strongly localized, they cannot be described in the framework of (semi-)local DFT. In fact, under the application of GGA functionals, the system was erroneously predicted to be metallic. Consequently, the application of the *GW*+BSE on top of an erroneous electronic structure would result in an inaccurate description of optical properties. We expect that the use of a self-consistent *GW* scheme could be helpful to overcome this problem. Unfortunately, however, due to the complexity of the system this would provoke unfeasible computational costs.

To overcome this limitation, modified hybrid functionals were applied. We showed that by reducing the fraction of exact exchange (EXX) included in the calculations, we were able to (i) achieve similar absorption properties as compared to the *GW*+BSE already on the IPA level of theory, and (ii) to also accurately describe the energetic position of defect-related states. So to our knowledge, this methodology allowed us to realistically describe the absorption properties of charged O vacancies and to relate them to those of gray tracks for the first time.

We found that the absorption signatures of O vacancies are strongly influenced by both their charge state and the light polarization. More precisely, the strongest impact was calculated for light polarized parallel to [001]. In addition, the charge state +2 (corresponding to completely emptied defect levels) does not cause additional mid-gap absorptions. The charge state +1, whose EPR signatures have already been experimentally resolved, as well the neutral vacancy in the spin configuration $S = 1$, show absorption maxima for photon energies of about $1\,\text{eV}$. These match the absorption characteristics of gray tracks in an early stage.

Neutral vacancies featuring a diamagnetic spin configuration, on the other hand, show overall higher absorptions and additional peaks located at higher photon energies. The latter are in good agreement with the absorption maxima of gray tracks.

So, because of the similar absorption characteristics, our data support the scenario that gray tracking could be the result of successive charging of O vacancies.

Understanding gray track formation   The gray tracking phenomenon, however, could involve more complex mechanisms, which have not been considered, yet, and there are still open questions. In particular, why a small rubidium doping (less than 1%) is beneficial in preventing the formation of gray tracks, despite O-vacancy-related Ti^{3+} centers also being present in RTP crystals, is yet unknown. In addition, also the influence of K vacancies on the properties of these Ti^{3+} centers has never been systematically investigated before. These aspects were addressed in the last part of this thesis.

To this end, we modeled O vacancies in different chemical environments, which are relevant for optical applications, i. e., stoichiometric KTP, Rb-doped KTP (RKTP), and K-deficient KTP. For the modeling, we used the Hubbard correction to specifically reduce one Ti atom in the

cell. More precisely, in each case we simulated two different Ti^{3+} centers. The first corresponds to the Ti(2) atom directly adjacent the vacancy, the second to the next-nearest Ti(2) atom. We did not simulated any $Ti(1)^{3+}$ center, because (i) the relevant Ti^{3+} center has been attributed to the Ti(2) by experiment, and (ii) in analogy to $KTiPO_4F$ crystals, electrons are expected to be trapped first by Ti(2) sites.

Our calculations suggest that the defect model commonly attributed to the gray track formation has to be partially revised: We still think that the formation of O vacancies is necessary, since they enable the reduction of the Ti atoms in the cell. However, we would shift the position of the Ti^{3+} from the undercoordinated Ti(2) site near the vacancy to the next-nearest Ti(2). This, in fact, leads to far better agreement with experimental hyperfine tensors. In addition, this attribution is also energetically more stable compared to the former. Notably, this holds for every investigated defect complex. Nevertheless, we doubt that O-vacancy-related defect states can be directly excited by either the first or the second harmonic of KTP. Two-photon processes, however, might still possible. In fact, upon the inclusion of additional Ti valence states, the position of the Ti^{3+}-related defect states was shifted towards the valence band, so higher photon energies could be required for their excitation.

Energetically more stable Ti^{3+} centers are characterized by a nearby K^+ ion, which we expect to stabilize the trapped electron via electrostatic forces, i. e., a bound polaron. We believe that the Ti^{3+} center could follow the migration of the K^+ ion through the lattice. This could lead to overpopulated K channels, which, together with their neighboring Ti^{3+} center, might correspond to gray tracks. To conclude, our findings are crucial to further deepen the knowledge on the gray track formation in KTP. Our hypothesis, in fact, requires additional theoretical and experimental investigations to (i) confirm (falsify) that gray tracks show an excess of K and (ii) better understand the migration mechanisms of bound polarons through the lattice.

Bibliography

[1] J. J. Yoo, S. S. Shin and J. Seo, Toward Efficient Perovskite Solar Cells: Progress, Strategies, and Perspectives, ACS Energy Letters **7**, 2084 (2022).

[2] Y. Zou, H.-Y. Wang, Y. Qin, C. Mu, Q. Li, D. Xu and J.-P. Zhang, Reduced Defects of MAPbI$_3$ Thin Films Treated by FAI for High-Performance Planar Perovskite Solar Cells, Advanced Functional Materials **29**, 1805810 (2019).

[3] L. K. Ono, S. F. Liu and Y. Qi, Reducing Detrimental Defects for High-Performance Metal Halide Perovskite Solar Cells, Angewandte Chemie International Edition **59**, 6676 (2020).

[4] X. A. Cao, J. A. Teetsov, F. Shahedipour-Sandvik and S. D. Arthur, Microstructural origin of leakage current in GaN/InGaN light-emitting diodes, Journal of Crystal Growth **264**, 172 (2004).

[5] D. J. Di Maria and E. Cartier, Mechanism for stress-induced leakage currents in thin silicon dioxide films, Journal of Applied Physics **78**, 3883 (1995).

[6] J. Jiménez, Laser diode reliability: crystal defects and degradation modes, Comptes Rendus Physique **4**, 663 (2003).

[7] E. C. Madhava-Menon, P. M. Petroff and R. G. Waters, Degradation kinetics of GaAs quantum well lasers, Applied Physics Letters **54**, 2683 (1989).

[8] H. Pick, Festkörperphysik, Naturwissenschaften **41**, 346 (1954).

[9] H. Tholl, Bauelemente der Halbleiterelektronik (Vieweg+Teubner Verlag Wiesbaden, 1976).

[10] S. Kück, Laser-related spectroscopy of ion-doped crystals for tunable solid-state lasers, Applied Physics B **72**, 515 (2001).

[11] X. Lin *et al.*, Superconductivity induced by La doping in $Sr_{1-x}La_xFBiS_2$, Physical Review B **87**, 020504 (2013).

[12] C. W. Thiel, Y. Sun, R. M. Macfarlane, T. Böttger and R. L. Cone, Rare-earth-doped LiNbO$_3$ and KTiOPO$_4$ (KTP) for waveguide quantum memories, Journal of Physics B: Atomic, Molecular and Optical Physics **45**, 124013 (2012).

[13] S. Pezzagna and J. Meijer, Quantum computer based on color centers in diamond, Applied Physics Reviews **8**, 011308 (2021).

[14] C. Liu, Z. G. Neale and G. Cao, Understanding electrochemical potentials of cathode materials in rechargeable batteries, Materials Today **19**, 109 (2016).

[15] A. Van der Ven, Z. Deng, S. Banerjee and S. P. Ong, Rechargeable Alkali-Ion Battery Materials: Theory and Computation, Chemical Reviews **120**, 6977 (2020), and references within.

[16] L. Ouvrard and M. Troost, Rechearches sur les phosphates doubles de titane, d'étain et de cuivre, Comptes Rendus **111**, 177 (1890).

[17] J. D. Bierlein and H. Vanherzeele, Potassium titanyl phosphate: properties and new applications, Journal of the Optical Society of America B: Optical Physics **6**, 622 (1989).

[18] J. D. Bierlein, A. Ferretti, L. H. Brixner and W. Y. Hsu, Fabrication and characterization of optical waveguides in KTiOPO$_4$, Applied Physics Letters **50**, 1216 (1987).

[19] C. A. Ebbers and S. P. Velsko, High average power KTiOPO$_4$ electro-optic Q-switch, Applied Physics Letters **67**, 593 (1995).

[20] A. Arie, G. Rosenman, V. Mahal, A. Skliar, M. Oron, M. Katz and D. Eger, Green and ultraviolet quasi-phase-matched second harmonic generation in bulk periodically-poled KTiOPO$_4$, Optics Communications **142**, 265 (1997).

[21] C. Canalias, J. Hirohashi, V. Pasiskevicius and F. Laurell, Polarization-switching characteristics of flux-grown KTiOPO$_4$ and RbTiOPO$_4$ at room temperature, Journal of Applied Physics **97**, 124105 (2005).

[22] G. Qiu, H. Huang, B. Zhang, J. He, J. Yang and J. Xu, Highly efficient intracavity frequency doubling 532-nm laser based on the gray tracking resistance KTP crystal, Laser physics **20**, 777 (2010).

[23] M. Peltz, U. Bäder, A. Borsutzky, R. Wallenstein, J. Hellström, H. Karlsson, V. Pasiskevicius and F. Laurell, Optical parametric oscillators for high pulse energy and high average power operation based on large aperture periodically poled KTP and RTA, Applied Physics B **73**, 663 (2001).

[24] J. D. Bierlein and C. B. Arweiler, Electro-optic and dielectric properties of KTiOPO$_4$, Applied Physics Letters **49**, 917 (1986).

[25] X. D. Wang, P. Basseras, R. J. D. Miller and H. Vanherzeele, Investigation of KTiOPO$_4$ as an electro-optic amplitude modulator, Applied physics letters **59**, 519 (1991).

[26] I. Savatinova, I. Savova, E. Liarokapis, C. C. Ziling, V. V. Atuchin, M. N. Armenise and V. M. N. Passaro, A comparative analysis of Rb:KTP and Cs:KTP optical waveguides, Journal of Physics D: Applied Physics **31**, 1667 (1998).

[27] C. Eigner, L. Padberg, M. Santandrea, H. Herrmann, B. Brecht and C. Silberhorn, Spatially single mode photon pair source at 800 nm in periodically poled Rubidium exchanged KTP waveguides, Opt. Express **28**, 32925 (2020).

[28] J. Huang, X. Cai, H. Yin, Y. Li, W. Lin, S. Huang and Y. Zhang, A new candidate in polyanionic compounds for a potassium-ion battery cathode: KTiOPO$_4$, The Journal of Physical Chemistry Letters **12**, 2721 (2021).

[29] J. Huang, X. Cai, Y. Li, Z. Fang, Y. Li, W. Lin, S. Huang and Y. Zhang, DFT investigations of KTiOPO$_4$M$_x$ (M= K, Na, and Li) anodes for alkali-ion battery, The Journal of Chemical Physics **156**, 204702 (2022).

[30] S. S. Fedotov, N. R. Khasanova, A. S. Samarin, O. A. Drozhzhin, D. Batuk, O. M. Karakulina, J. Hadermann, A. M. Abakumov and E. V. Antipov, AVPO$_4$F (A= Li, K): A 4 V Cathode Material for High-Power Rechargeable Batteries, Chemistry of Materials **28**, 411 (2016).

[31] S. S. Fedotov *et al.*, Reversible facile Rb$^+$ and K$^+$ ions de/insertion in a KTiOPO$_4$-type RbVPO$_4$F cathode material, Journal of Materials Chemistry A **6**, 14420 (2018).

[32] S. S. Fedotov, A. S. Samarin and E. V. Antipov, KTiOPO$_4$-structured electrode materials for metal-ion batteries: A review, Journal of Power Sources **480**, 228840 (2020).

[33] S. S. Fedotov *et al.*, Titanium-based potassium-ion battery positive electrode with extraordinarily high redox potential, Nature communications **11**, 1484 (2020).

[34] N. S. Katorova, S. S. Fedotov, D. P. Rupasov, N. D. Luchinin, B. Delattre, Y.-M. Chiang, A. M. Abakumov and K. J. Stevenson, Effect of Concentrated Diglyme-Based Electrolytes on the Electrochemical Performance of Potassium-Ion Batteries, ACS Applied Energy Materials **2**, 6051 (2019).

[35] H. Tan, X. Du, J.-Q. Huang and B. Zhang, KVPO$_4$F as a novel insertion-type anode for potassium ion batteries, Chemical Communications **55**, 11311 (2019).

[36] K. Chihara, A. Katogi, K. Kubota and S. Komaba, KVPO$_4$F and KVOPO$_4$ toward 4 volt-class potassium-ion batteries, Chemical Communications **53**, 5208 (2017).

[37] L. Mu, L. Ben, Y.-S. Hu, H. Li, L. Chen and X. Huang, Novel 1.5 V anode materials, ATiOPO$_4$ (A= NH$_4$, K, Na), for room-temperature sodium-ion batteries, Journal of Materials Chemistry A **4**, 7141 (2016).

[38] M. Galceran, J. Rikarte, M. Zarrabeitia, M. C. Pujol, M. Aguiló and M. Casas-Cabanas, Investigation of NaTiOPO$_4$ as Anode for Sodium-Ion Batteries: A Solid Electrolyte Interphase Free Material?, ACS Applied Energy Materials **2**, 1923 (2019).

[39] S. Liu, L. Shao, X. Zhang, M. Zhou, Z. Tao and J. Chen, KTiOPO$_4$ as a novel anode material for sodium-ion batteries, Journal of Alloys and Compounds **754**, 147 (2018).

[40] J. Ding *et al.*, KVOPO$_4$: A New High Capacity Multielectron Na-Ion Battery Cathode, Advanced Energy Materials **8**, 1800221 (2018).

[41] B. Boulanger, I. Rousseau, J. Fève, M. Maglione, B. Menaert and G. Marnier, Optical studies of laser-induced gray-tracking in KTP, IEEE Journal of Quantum Electronics **35**, 281 (1999).

[42] V. A. Maslov, V. A. Mikhailov, O. P. Shaunin and I. A. Shcherbakov, Nonlinear absorption in KTP crystals, Quantum Electronics **27**, 356 (1997).

[43] G. M. Loiacono, D. N. Loiacono, T. McGee and M. Babb, Laser damage formation in KTiOPO$_4$ and KTiOAsO$_4$ crystals: Grey tracks, Journal of Applied Physics **72**, 2705 (1992).

[44] B. Boulanger, M. M. Fejer, R. Blachman and P. F. Bordui, Study of KTiOPO$_4$ gray-tracking at 1064, 532, and 355 nm, Applied Physics Letters **65**, 2401 (1994).

[45] L. Padberg, V. Quiring, A. Bocchini, M. Santandrea, U. Gerstmann, W. G. Schmidt, C. Silberhorn and C. Eigner, DC Ionic Conductivity in KTP and Its Isomorphs: Properties, Methods for Suppression, and Its Connection to Gray Tracking, Crystals **12**, 1359 (2022).

[46] A. Alexandrovski, M. Fejer and G. Mitchell, CW gray-track formation in KTP, in Technical Digest. Summaries of papers presented at the Conference on Lasers and Electro-Optics. Postconference Edition. CLEO '99. Conference on Lasers and Electro-Optics (IEEE Cat. No.99CH37013), Pages 531–532, 1999.

[47] M. G. Roelofs, Identification of Ti^{3+} in potassium titanyl phosphate and its possible role in laser damage, Journal of Applied Physics **65**, 4976 (1989).

[48] V. Mürk, V. Denks, A. Dudelzak, P.-P. Proulx and V. Vassiltsenko, Gray tracks in KTiOPO$_4$: Mechanism of creation and bleaching, Nuclear Instruments and Methods in Physics Research Section B: Beam Interactions with Materials and Atoms **141**, 472 (1998).

[49] M. P. Scripsick, G. J. Edwards, L. E. Halliburton, R. F. Belt and G. M. Loiacono, Effect of crystal growth on Ti^{3+} centers in KTiOPO$_4$, Journal of Applied Physics **76**, 773 (1994).

[50] L. E. Halliburton and M. P. Scripsick, Mechanisms and point defects responsible for the formation of gray tracks in KTP, in Solid State Lasers and Nonlinear Crystals Vol. 2379, Pages 235–244, SPIE, 1995.

[51] M. P. Scripsick, G. J. Edwards, L. E. Halliburton, R. F. Belt and L. A. Kappers, Point defects in KTP and their possible role in laser damage, in Inorganic Crystals for Optics, Electro-Optics, and Frequency Conversion Vol. 1561, Pages 93–103, SPIE, 1991.

[52] M. P. Scripsick, D. N. Loiacono, J. Rottenberg, S. H. Goellner, L. E. Halliburton and F. K. Hopkins, Defects responsible for gray tracks in flux-grown KTiOPO$_4$, Applied physics letters **66**, 3428 (1995).

[53] Y. Zhang, J. Li, X. Cao, J. Yang, J. Wang and H. Jiang, A study of vacancy defects related to gray tracks in KTiOPO$_4$ (KTP) using positron annihilation, AIP Advances **4**, 127103 (2014).

[54] S. D. Setzler, K. T. Stevens, N. C. Fernelius, M. P. Scripsick, G. J. Edwards and L. E. Halliburton, Electron paramagnetic resonance and electro-nuclear double-resonance study of Ti^{3+} centres in KTiOPO$_4$, Journal of Physics: Condensed Matter **15**, 3969 (2003).

[55] M. Roth, Stoichiometry and Domain Structure of KTP-Type Nonlinear Optical Crystals, in Springer Handbook of Crystal Growth, edited by G. Dhanaraj, K. Byrappa, V. Prasad and M. Dudley, Chap. 20, Pages 691–723, Springer Berlin Heidelberg, Berlin, Heidelberg, 2010, and references within.

[56] A. Zukauskas, V. Pasiskevicius and C. Canalias, Second-harmonic generation in periodically poled bulk Rb-doped KTiOPO$_4$ below 400 nm at high peak-intensities, Optics express **21**, 1395 (2013).

[57] X. Mu and Y. J. Ding, Investigation of damage mechanisms of $KTiOPO_4$ crystals by use of a continuous-wave argon laser, Applied Optics **39**, 3099 (2000).

[58] G. Bhar, P. Kumbhakar, A. Chaudhary and U. Chatterjee, Tunable infrared generation in KTA and applications, Pramana **53**, 321 (1999).

[59] P. Morris, A. Ferretti, J. Bierlein and G. Loiacono, Reduction of the ionic conductivity of flux grown $KTiOPO_4$ crystals, Journal of Crystal Growth **109**, 367 (1991).

[60] R. Masse and J.-C. Grenier, Étude des monophosphates du type $M^I TiOPO_4$ avec $M^I = K$, Rb et Tl, Bulletin de Minéralogie **94**, 437 (1971).

[61] P. I. Tordjman, E. Masse and J. C. Guitel, Structure cristalline du monophosphate $KTiPO_5$, Zeitschrift für Kristallographie **139**, 103 (1974).

[62] N. Angert, M. Tseitlin, E. Yashchin and M. Roth, Ferroelectric phase transition temperatures of $KTiOPO_4$ crystals grown from self-fluxes, Applied Physics Letters **67**, 1941 (1995).

[63] W. T. Harrison, T. E. Gier, G. D. Stucky and A. J. Schultz, Structural study of the ferroelectric to paraelectric phase transition in $TlTiOPO_4$, Materials Research Bulletin **30**, 1341 (1995).

[64] S. C. Mayo, P. A. Thomas, S. J. Teat, G. M. Loiacono and D. N. Loiacono, Structure and non-linear optical properties of $KTiOAsO_4$, Acta Crystallographica Section B **50**, 655 (1994).

[65] P. Delarue, C. Lecomte, M. Jannin, G. Marnier and B. Menaert, Evolution towards centrosymmetry of the nonlinear-optical material $RbTiOPO_4$ in the temperature range 293–973 K: Alkaline displacements and titanyl deformations, Physical Review B **58**, 5287 (1998).

[66] K. Momma and F. Izumi, *VESTA3* for three-dimensional visualization of crystal, volumetric and morphology data, Journal of Applied Crystallography **44**, 1272 (2011).

[67] D. R. Allan, J. S. Loveday, R. J. Nelmes and P. A. Thomas, A high-pressure structural study of potassium titanyl phosphate (KTP) up to 5 GPa, Journal of Physics: Condensed Matter **4**, 2747 (1992).

[68] S.-i. Furusawa, H. Hayasi, Y. Ishibashi, A. Miyamoto and T. Sasaki, Ionic Conductivity of Quasi-One-Dimensional Superionic Conductor $KTiOPO_4$ (KTP) Single Crystal, Journal of the Physical Society of Japan **62**, 183 (1993).

[69] B. Mohamadou, G. E. Kugel, F. Brehat, B. Wyncke, G. Marnier and P. Simon, High-temperature vibrational spectra, relaxation and ionic conductivity effects in $KTiOPO_4$, Journal of Physics: Condensed Matter **3**, 9489 (1991).

[70] M. R. J. Gandhi, B. Vijayalakshmi and P. Sureshkumar, Growth of Pure and Mo Doped Potassium Titanyl Phosphate (KTP) Crystals: Influence of KTP/Flux Ratios on the Growth Morphology, Journal of Minerals and Material Characterization and Engineering **10**, 683 (2011).

[71] P. Bordui and J. Jacco, Viscosity and density of solutions used in high-temperature solution growth of $KTiOPO_4$ (KTP), Journal of Crystal Growth **82**, 351 (1987).

[72] V. D. Kugel, G. Rosenman, N. Angert, E. Yaschin and M. Roth, Domain inversion in KTiOPO$_4$ crystal near the Curie point, Journal of Applied Physics **76**, 4823 (1994).

[73] K. Stevens, L. Halliburton, M. Roth, N. Angert and M. Tseitlin, Identification of a Pb-related Ti^{3+} center in flux-grown KTiOPO$_4$, Journal of Applied Physics **88**, 6239 (2000).

[74] G. J. Edwards, M. P. Scripsick, L. E. Halliburton and R. F. Belt, Identification of a radiation-induced hole center in KTiOPO$_4$, Physical Review B **48**, 6884 (1993).

[75] A. Miyamoto, Y. Mori, Y. Okada, T. Sasaki and S. Nakai, Refractive index and lattice constant variations in flux grown KTP crystals, Journal of Crystal Growth **156**, 303 (1995).

[76] G. Rosenman, A. Skliar, D. Eger, M. Oron and M. Katz, Low temperature periodic electrical poling of flux-grown KTiOPO$_4$ and isomorphic crystals, Applied Physics Letters **73**, 3650 (1998).

[77] P. A. Thomas, R. Duhlev and S. J. Teat, A comparative structural study of a flux-grown crystal of K$_{0.86}$Rb$_{0.14}$TiOPO$_4$ and an ion-exchanged crystal of K$_{0.84}$Rb$_{0.16}$TiOPO$_4$, Acta Crystallographica Section B **50**, 538 (1994).

[78] C. Eigner, Periodically poled waveguides in potassium titanyl phosphate: from technology development to applications, PhD Thesis, Universität Paderborn, Paderborn, 2019.

[79] F. C. Zumsteg, J. D. Bierlein and T. E. Gier, K$_x$Rb$_{1-x}$TiOPO$_4$: A new nonlinear optical material, Journal of Applied Physics **47**, 4980 (1976).

[80] D. Xue and S. Zhang, The origin of nonlinearity in KTiOPO$_4$, Applied Physics Letters **70**, 943 (1997).

[81] A. H. Reshak, I. V. Kityk and S. Auluck, Investigation of the Linear and Nonlinear Optical Susceptibilities of KTiOPO$_4$ Single Crystals: Theory and Experiment, The Journal of Physical Chemistry B **114**, 16705 (2010), PMID: 21126037.

[82] H. Li, C. Kam, Y. Lam and W. Ji, Femtosecond Z-scan measurements of nonlinear refraction in nonlinear optical crystals, Optical Materials **15**, 237 (2001).

[83] M. Sheik-Bahae, D. Hutchings, D. Hagan and E. Van Stryland, Dispersion of bound electron nonlinear refraction in solids, IEEE Journal of Quantum Electronics **27**, 1296 (1991).

[84] A. Dudelzak, P.-P. Proulx, V. Denks, V. Mürk and V. Nagirnyi, Anisotropic fundamental absorption edge of KTiOPO$_4$ crystals, Journal of Applied Physics **87**, 2110 (2000).

[85] L. K. Cheng and J. D. Bierlein, KTP and isomorphs - recent progress in device and material development, Ferroelectrics **142**, 209 (1993).

[86] R. A. Stolzenberger and M. P. Scripsick, Recent advancements in the periodic poling and characterization of RTA and its isomorphs, in Laser Material Crystal Growth and Nonlinear Materials and Devices, edited by K. I. Schaffers and L. E. Myers Vol. 3610, Pages 23 – 35, International Society for Optics and Photonics, SPIE, 1999.

[87] J. D. Bierlein and F. Ahmed, Observation and poling of ferroelectric domains in KTiOPO$_4$, Applied Physics Letters **51**, 1322 (1987).

[88] Y. Zhang, Y. Leng, J. Liu, N. Ji, X. Duan, J. Li, X. Zhao, J. Wang and H. Jiang, Mechanism of hydrogen treatment in KTiOPO$_4$ crystals at high temperature: experimental and first-principles studies, CrystEngComm **17**, 3793 (2015).

[89] N. B. Angert, V. M. Garmash, N. I. Pavlova and A. V. Tarasov, Influence of color centers on the optical properties of KTP crystals and on the efficiency of the laser radiation frequency conversion in these crystals, Soviet Journal of Quantum Electronics **21**, 426 (1991).

[90] Q. Zhang, G. Feng, J. Han, B. Li, Q. Zhu and X. Xie, High repetition rate laser pulse induced damage in KTP crystal: Gray-tracking and catastrophic damage, Optik **122**, 1313 (2011).

[91] H. Zhou, X. He, W. Wu, J. Tong, J. Wang, Y. Zuo, Y. Wu, C. Zhang and Z. Hu, Hydrothermal growth of KTiOPO$_4$ crystal for electro-optical application, Light: Science & Applications **12**, 1 (2023).

[92] F. R. Wagner, G. Duchateau, J.-Y. Natoli, H. Akhouayri and M. Commandré, Catastrophic nanosecond laser induced damage in the bulk of potassium titanyl phosphate crystals, Journal of Applied Physics **115**, 243102 (2014).

[93] K. Terashima, M. T. M. Takena and M. K. M. Kawachi, Transparency Improvement of Potassium Titanyl Phosphate (KTP) Crystals by Annealing under Oxygen Atmosphere, Japanese Journal of Applied Physics **30**, L497 (1991).

[94] L. Bausá, J. García Solé, A. Durán and J. Fernández Navarro, Characterization of titanium induced optical absorption bands in phosphate glasses, Journal of Non-Crystalline Solids **127**, 267 (1991).

[95] A. Bocchini, C. Eigner, C. Silberhorn, W. G. Schmidt and U. Gerstmann, Understanding gray track formation in KTP: Ti^{3+} centers studied from first principles, Physical Review Materials **4**, 124402 (2020).

[96] Y. Jiang, L. Halliburton, M. Roth, M. Tseitlin and N. Angert, EPR and ENDOR study of an oxygen-vacancy-associated Ti^{3+} center in RbTiOPO$_4$ crystals, Physica B: Condensed Matter **400**, 190 (2007).

[97] R. M. Dreizler and E. Engel, Density Functional Theory: An Advanced Course (Berlin, Heidelberg: Springer-Verlag Berlin Heidelberg, 2011), and references within.

[98] M. Born and R. Oppenheimer, Zur Quantentheorie der Molekeln, Annalen der Physik **389**, 457 (1927).

[99] D. R. Hartree, The Wave Mechanics of an Atom with a Non-Coulomb Central Field. Part I. Theory and Methods, Mathematical Proceedings of the Cambridge Philosophical Society **24**, 89–110 (1928).

[100] J. C. Slater, Note on Hartree's Method, Physical Review **35**, 210 (1930).

[101] V. Fock, Näherungsmethode zur Lösung des quantenmechanischen Mehrkörperproblems, Zeitschrift für Physik **61**, 126 (1930).

[102] P. Hohenberg and W. Kohn, Inhomogeneous Electron Gas, Physical Review **136**, B864 (1964).

[103] W. Kohn and L. J. Sham, Self-Consistent Equations Including Exchange and Correlation Effects, Physical Review **140**, A1133 (1965).

[104] W. Ritz, Über eine neue Methode zur Lösung gewisser Variationsprobleme der mathematischen Physik., Journal für die reine und angewandte Mathematik (Crelles Journal) **1909**, 1 (1909).

[105] G. Czycholl, Theoretische Festkörperphysik: Von den klassischen Modellen zu modernen Forschungsthemen Springer-Lehrbuch, 2nd Edition (Berlin, Heidelberg: Springer Berlin Heidelberg, 2004).

[106] D. M. Ceperley and B. J. Alder, Ground State of the Electron Gas by a Stochastic Method, Physical Review Letters **45**, 566 (1980).

[107] J. P. Perdew and A. Zunger, Self-interaction correction to density-functional approximations for many-electron systems, Physical Review B **23**, 5048 (1981).

[108] W. Kohn, Nobel Lecture: Electronic structure of matter-wave functions and density functionals, Review Modern Physics **71**, 1253 (1999).

[109] J. P. Perdew, K. Burke and M. Ernzerhof, Generalized Gradient Approximation Made Simple, Physical Review Letters **77**, 3865 (1996).

[110] J. P. Perdew and Y. Wang, Accurate and simple analytic representation of the electron-gas correlation energy, Physical Review B **45**, 13244 (1992).

[111] J. P. Perdew, A. Ruzsinszky, G. I. Csonka, O. A. Vydrov, G. E. Scuseria, L. A. Constantin, X. Zhou and K. Burke, Restoring the Density-Gradient Expansion for Exchange in Solids and Surfaces, Physical Review Letters **100**, 136406 (2008).

[112] J. P. Perdew, A. Ruzsinszky, G. I. Csonka, O. A. Vydrov, G. E. Scuseria, L. A. Constantin, X. Zhou and K. Burke, Erratum: Restoring the Density-Gradient Expansion for Exchange in Solids and Surfaces [Phys. Rev. Lett. 100, 136406 (2008)], Physical Review Letters **102**, 039902 (2009).

[113] P. J. Hasnip, K. Refson, M. I. J. Probert, J. R. Yates, S. J. Clark and C. J. Pickard, Density functional theory in the solid state, Philosophical Transactions of the Royal Society A: Mathematical, Physical and Engineering Sciences **372**, 20130270 (2014).

[114] L. J. Sham and M. Schlüter, Density-Functional Theory of the Energy Gap, Physical Review Letters **51**, 1888 (1983).

[115] J. P. Perdew and M. Levy, Physical Content of the Exact Kohn-Sham Orbital Energies: Band Gaps and Derivative Discontinuities, Physical Review Letters **51**, 1884 (1983).

[116] C. Friedrich and A. Schindlmayr, Many-body perturbation theory: The GW approximation, NIC Series Vol. 31 (John von Neumann Institute for Computing, 2006), Page 335–355.

[117] S. Albrecht, Optical absorption spectra of semiconductors and insulators: ab initio calcula-
tion of many-body effects, PhD Thesis, Ècole polytechnique, Gif-sur-Yvette, 1999, and
references within.

[118] G. C. Wick, The Evaluation of the Collision Matrix, Physical Review **80**, 268 (1950).

[119] L. Hedin, New Method for Calculating the One-Particle Green's Function with Application to
the Electron-Gas Problem, Physical Review **139**, A796 (1965).

[120] L. T. Hedin and S. O. Lundqvist, Effects of Electron-Electron and Electron-Phonon Interac-
tions on the One-Electron States of Solids, Journal of Physics C: Solid State Physics **23**, 1
(1969).

[121] F. Bechstedt Many-body approach to electronic excitations Vol. 181 (Springer Berlin, Hei-
delberg, 2015).

[122] C. Rödl, Elektronische und exzitonische Anregungen in magnetischen Isolatoren, PhD Thesis,
Friedrich-Schiller-Universität Jena, Jena, 2009.

[123] F. Fuchs, J. Furthmüller, F. Bechstedt, M. Shishkin and G. Kresse, Quasiparticle band struc-
ture based on a generalized Kohn-Sham scheme, Physical Review B **76**, 115109 (2007).

[124] B. Himmetoglu, A. Floris, S. De Gironcoli and M. Cococcioni, Hubbard-corrected DFT
energy functionals: The LDA+U description of correlated systems, International Journal of
Quantum Chemistry **114**, 14 (2014).

[125] I. Austin and N. Mott, Metallic and Nonmetallic Behavior in Transition Metal Oxides: Electron
correlation effects in narrow d bands and polarons are discussed., Science **168**, 71 (1970).

[126] V. I. Anisimov, J. Zaanen and O. K. Andersen, Band theory and Mott insulators: Hubbard
U instead of Stoner I, Physical Review B **44**, 943 (1991).

[127] V. I. Anisimov, I. V. Solovyev, M. A. Korotin, M. T. Czyżyk and G. A. Sawatzky, Density-
functional theory and NiO photoemission spectra, Physical Review B **48**, 16929 (1993).

[128] I. V. Solovyev, P. H. Dederichs and V. I. Anisimov, Corrected atomic limit in the local-density
approximation and the electronic structure of d impurities in Rb, Physical Review B **50**, 16861
(1994).

[129] J. Hubbard, Electron correlations in narrow energy bands, Proceedings of the Royal Society
of London. Series A. Mathematical and Physical Sciences **276**, 238 (1963).

[130] J. Hubbard, Electron correlations in narrow energy bands II. The degenerate band case, Pro-
ceedings of the Royal Society of London. Series A. Mathematical and Physical Sciences
277, 237 (1964).

[131] J. Hubbard, Electron correlations in narrow energy bands III. An improved solution, Proceed-
ings of the Royal Society of London. Series A. Mathematical and Physical Sciences **281**,
401 (1964).

[132] J. Hubbard, Electron correlations in narrow energy bands IV. The atomic representation, Proceedings of the Royal Society of London. Series A. Mathematical and Physical Sciences **285**, 542 (1965).

[133] J. Hubbard, Electron correlations in narrow energy bands V. A perturbation expansion about the atomic limit, Proceedings of the Royal Society of London. Series A. Mathematical and Physical Sciences **296**, 82 (1967).

[134] J. Hubbard, Electron correlations in narrow energy bands VI. The connexion with many-body perturbation theory, Proceedings of the Royal Society of London. Series A. Mathematical and Physical Sciences **296**, 100 (1967).

[135] M. Cococcioni and S. de Gironcoli, Linear response approach to the calculation of the effective interaction parameters in the $LDA + U$ method, Physical Review B **71**, 035105 (2005).

[136] T. R. Paudel and W. R. L. Lambrecht, First-principles calculation of the O vacancy in ZnO: A self-consistent gap-corrected approach, Physical Review B **77**, 205202 (2008).

[137] O. K. Orhan and D. D. O'Regan, First-principles Hubbard U and Hund's J corrected approximate density functional theory predicts an accurate fundamental gap in rutile and anatase TiO_2, Physical Review B **101**, 245137 (2020).

[138] C. E. Patrick and F. Giustino, GW quasiparticle bandgaps of anatase TiO_2 starting from DFT+U, Journal of Physics: Condensed Matter **24**, 202201 (2012).

[139] J. F. Janak, Proof that $\frac{\partial E}{\partial n_i} = \epsilon$ in density-functional theory, Physical Review B **18**, 7165 (1978).

[140] A. D. Becke, A new mixing of Hartree-Fock and local density-functional theories, The Journal of chemical physics **98**, 1372 (1993).

[141] J. Heyd, G. E. Scuseria and M. Ernzerhof, Hybrid functionals based on a screened Coulomb potential, The Journal of Chemical Physics **118**, 8207 (2003).

[142] J. Heyd, G. E. Scuseria and M. Ernzerhof, Erratum: "Hybrid functionals based on a screened Coulomb potential" [J. Chem. Phys. 118, 8207 (2003)], The Journal of Chemical Physics **124**, 219906 (2006).

[143] J. P. Perdew, M. Ernzerhof and K. Burke, Rationale for mixing exact exchange with density functional approximations, The Journal of Chemical Physics **105**, 9982 (1996).

[144] C. Adamo and V. Barone, Toward reliable density functional methods without adjustable parameters: The PBE0 model, The Journal of Chemical Physics **110**, 6158 (1999).

[145] A. D. Becke, Density-functional thermochemistry. III. The role of exact exchange, The Journal of Chemical Physics **98**, 5648 (1993).

[146] C. Lee, W. Yang and R. G. Parr, Development of the Colle-Salvetti correlation-energy formula into a functional of the electron density, Physical Review B **37**, 785 (1988).

[147] P. J. Stephens, F. J. Devlin, C. F. Chabalowski and M. J. Frisch, Ab Initio Calculation of Vibrational Absorption and Circular Dichroism Spectra Using Density Functional Force Fields, The Journal of Physical Chemistry **98**, 11623 (1994).

[148] J. B. Goodenough and K.-S. Park, The Li-Ion Rechargeable Battery: A Perspective, Journal of the American Chemical Society **135**, 1167 (2013), PMID: 23294028.

[149] B. Dunn, H. Kamath and J.-M. Tarascon, Electrical Energy Storage for the Grid: A Battery of Choices, Science **334**, 928 (2011).

[150] M. Li, J. Lu, Z. Chen and K. Amine, 30 Years of Lithium-Ion Batteries, Advanced Materials **30**, 1800561 (2018).

[151] J. E. Harlow *et al.*, A Wide Range of Testing Results on an Excellent Lithium-Ion Cell Chemistry to be used as Benchmarks for New Battery Technologies, Journal of The Electrochemical Society **166**, A3031 (2019).

[152] M. Fichtner, Recent Research and Progress in Batteries for Electric Vehicles, Batteries & Supercaps **5**, e202100224 (2022).

[153] W. M. Haynes, editor, CRC Handbook of Chemistry and Physics, 97 Edition (CRC press: Boca Raton, FL, Boca Raton, 2016).

[154] A. V, B. John and M. TD, Potassium-Ion Batteries: Key to Future Large-Scale Energy Storage?, ACS Applied Energy Materials **3**, 9478 (2020).

[155] Y. Zhao and J. Guo, Development of flexible Li-ion batteries for flexible electronics, InfoMat **2**, 866 (2020).

[156] K. Kubota, M. Dahbi, T. Hosaka, S. Kumakura and S. Komaba, Towards K-Ion and Na-Ion Batteries as "Beyond Li-Ion", The Chemical Record **18**, 459 (2018).

[157] J. Hao, K. Xiong, J. Zhou, A. M. Rao, X. Wang, H. Liu and B. Lu, Yolk–Shell P3-Type $K_{0.5}[Mn_{0.85}Ni_{0.1}Co_{0.05}]O_2$: A Low-Cost Cathode for Potassium-Ion Batteries, ENERGY & ENVIRONMENTAL MATERIALS **5**, 261 (2022).

[158] H. Ding, J. Zhou, A. M. Rao and B. Lu, Cell-like-carbon-micro-spheres for robust potassium anode, National Science Review **8** (2020).

[159] D. Su, A. McDonagh, S.-Z. Qiao and G. Wang, High-capacity aqueous potassium-ion batteries for large-scale energy storage, Advanced Materials **29**, 1604007 (2017).

[160] W. Luo, F. Shen, C. Bommier, H. Zhu, X. Ji and L. Hu, Na-Ion Battery Anodes: Materials and Electrochemistry, Accounts of Chemical Research **49**, 231 (2016), PMID: 26783764.

[161] V. Kapoor, B. Singh, G. Sai Gautam, A. K. Cheetham and P. Canepa, Rational Design of Mixed Polyanion Electrodes $Na_xV_2P_{3-i}(Si/S)_iO_{12}$ for Sodium Batteries, Chemistry of Materials **34**, 3373 (2022).

[162] B. Singh *et al.*, A chemical map of NaSICON electrode materials for sodium-ion batteries, J. Mater. Chem. A **9**, 281 (2021).

[163] Z. Xu, L. Gao, Y. Liu and L. Li, Review—Recent Developments in the Doped LiFePO$_4$ Cathode Materials for Power Lithium Ion Batteries, Journal of The Electrochemical Society **163**, A2600 (2016).

[164] H. Zhang, Y. Yang, D. Ren, L. Wang and X. He, Graphite as anode materials: Fundamental mechanism, recent progress and advances, Energy Storage Materials **36**, 147 (2021).

[165] H. Liu, X.-B. Cheng, J.-Q. Huang, S. Kaskel, S. Chou, H. S. Park and Q. Zhang, Alloy Anodes for Rechargeable Alkali-Metal Batteries: Progress and Challenge, ACS Materials Letters **1**, 217 (2019), https://doi.org/10.1021/acsmaterialslett.9b00118.

[166] K. Xu, Nonaqueous Liquid Electrolytes for Lithium-Based Rechargeable Batteries, Chemical Reviews **104**, 4303 (2004), PMID: 15669157.

[167] A. Hayashi, K. Noi, A. Sakuda and M. Tatsumisago, Superionic glass-ceramic electrolytes for room-temperature rechargeable sodium batteries, Nature Communications **3**, 856 (2012).

[168] Y. Kato, S. Hori, T. Saito, K. Suzuki, M. Hirayama, A. Mitsui, M. Yonemura, H. Iba and R. Kanno, High-power all-solid-state batteries using sulfide superionic conductors, Nature Energy **1**, 16030 (2016).

[169] G. Ceder, M. Aydinol and A. Kohan, Application of first-principles calculations to the design of rechargeable Li-batteries, Computational Materials Science **8**, 161 (1997), Proceedings of the joint NSF/CNRS Workshop on Alloy Theory.

[170] A. Urban, D.-H. Seo and G. Ceder, Computational understanding of Li-ion batteries, npj Computational Materials **2**, 16002 (2016).

[171] A. Ghosh, S. Pal and P. Sarkar, Rational Design of Two-Dimensional Porous Boron Phosphide as Efficient Cathode Material for Li and Na Ion Batteries: A First-Principles Study, The Journal of Physical Chemistry C **126**, 5092 (2022).

[172] V. Krishnamurthy and V. Viswanathan, Beyond Transition Metal Oxide Cathodes for Electric Aviation: The Case of Rechargeable CF$_x$, ACS Energy Letters **5**, 3330 (2020).

[173] X. Lv, F. Li, J. Gong, J. Gu, S. Lin and Z. Chen, Metallic FeSe monolayer as an anode material for Li and non-Li ion batteries: a DFT study, Physical Chemistry Chemical Physics **22**, 8902 (2020).

[174] G. Yoon, D.-H. Kim, I. Park, D. Chang, B. Kim, B. Lee, K. Oh and K. Kang, Using First-Principles Calculations for the Advancement of Materials for Rechargeable Batteries, Advanced Functional Materials **27**, 1702887 (2017).

[175] D. Adekoya, S. Zhang and M. Hankel, 1D/2D C3N4/Graphene Composite as a Preferred Anode Material for Lithium Ion Batteries: Importance of Heterostructure Design via DFT Computation, ACS Applied Materials & Interfaces **12**, 25875 (2020), PMID: 32421309.

[176] F. Zhou, M. Cococcioni, C. A. Marianetti, D. Morgan and G. Ceder, First-principles prediction of redox potentials in transition-metal compounds with $LDA + U$, Physical Review B **70**, 235121 (2004).

[177] E. B. Isaacs, S. Patel and C. Wolverton, Prediction of Li intercalation voltages in rechargeable battery cathode materials: Effects of exchange-correlation functional, van der Waals interactions, and Hubbard U, Physical Review Materials **4**, 065405 (2020).

[178] L. Wang, T. Maxisch and G. Ceder, Oxidation energies of transition metal oxides within the GGA + U framework, Physical Review B **73**, 195107 (2006).

[179] N. Luo, L. Feng, H. Yin, A. Stein, S. Huang, Z. Hou and D. G. Truhlar, Li_8MnO_6: A Novel Cathode Material with Only Anionic Redox, ACS Applied Materials & Interfaces **14**, 29832 (2022).

[180] V. L. Chevrier, S. P. Ong, R. Armiento, M. K. Y. Chan and G. Ceder, Hybrid density functional calculations of redox potentials and formation energies of transition metal compounds, Physical Review B **82**, 075122 (2010).

[181] M. Cococcioni and N. Marzari, Energetics and cathode voltages of $LiMPO_4$ olivines ($M =$ Fe, Mn) from extended Hubbard functionals, Physical Review Materials **3**, 033801 (2019).

[182] M. E. Arroyo y de Dompablo, A. Van der Ven and G. Ceder, First-principles calculations of lithium ordering and phase stability on Li_xNiO_2, Physical Review B **66**, 064112 (2002).

[183] G. Henkelman, B. P. Uberuaga and H. Jónsson, A climbing image nudged elastic band method for finding saddle points and minimum energy paths, The Journal of Chemical Physics **113**, 9901 (2000).

[184] W. P. Risk and G. M. Loiacono, Fabrication and characterization of ion-exchanged waveguides in potassium titanyl arsenate, Applied Physics Letters **69**, 4157 (1996).

[185] S. Neufeld, A. Schindlmayr and W. G. Schmidt, Quasiparticle energies and optical response of $RbTiOPO_4$ and $KTiOAsO_4$, Journal of Physics: Materials **5**, 015002 (2021).

[186] N. Voronina, J. H. Jo, A. Konarov, J. Kim and S.-T. Myung, $KTi_2(PO_4)_3$ Electrode with a Long Cycling Stability for Potassium-Ion Batteries, Small. **16**, 2001090 (2020).

[187] A. Bocchini, U. Gerstmann, T. Bartley, H.-G. Steinrück, G. Henkel and W. G. Schmidt, Electrochemical performance of $KTiOAsO_4$ (KTA) in potassium-ion batteries from density-functional theory, Physical Review Materials **6**, 105401 (2022).

[188] P. Giannozzi *et al.*, QUANTUM ESPRESSO: a modular and open-source software project for quantum simulations of materials, Journal of Physics: Condensed Matter **21**, 395502 (2009).

[189] P. Giannozzi *et al.*, Advanced capabilities for materials modelling with Quantum ESPRESSO, Journal of Physics: Condensed Matter **29**, 465901 (2017).

[190] A. Baldereschi, Mean-Value Point in the Brillouin Zone, Physical Review B **7**, 5212 (1973).

[191] G. M. Loiacono, D. N. Loiacono, J. J. Zola, R. A. Stolzenberger, T. McGee and R. G. Norwood, Optical properties and ionic conductivity of $KTiOAsO_4$ crystals, Applied Physics Letters **61**, 895 (1992).

[192] W. Zhang, W. Shao, B. Zhao and K. Dai, Review—Research Progress of Li_2FeSiO_4 Cathode Materials for Lithium-Ion Batteries, Journal of The Electrochemical Society **169**, 070526 (2022).

[193] S.-i. Nishimura, S. Hayase, R. Kanno, M. Yashima, N. Nakayama and A. Yamada, Structure of Li_2FeSiO_4, Journal of the American Chemical Society **130**, 13212 (2008).

[194] N. E. Novikova, I. A. Verin, N. I. Sorokina, O. A. Alekseeva, M. Tseitlin and M. Roth, Structure of $KTiOAsO_4$ single crystals at 293 and 30 K, Crystallography Reports **55**, 412 (2010).

[195] J. N. Hodgson, Optical Absorption and Dispersion in Solids, 1 Edition (Springer New York, NY, 1970).

[196] S. L. Adler, Quantum Theory of the Dielectric Constant in Real Solids, Physical Review **126**, 413 (1962).

[197] N. Wiser, Dielectric Constant with Local Field Effects Included, Physical Review **129**, 62 (1963).

[198] W. G. Schmidt, Calculation of reflectance anisotropy for semiconductor surface exploration, physica status solidi (b) **242**, 2751 (2005).

[199] R. Del Sole and R. Girlanda, Optical properties of semiconductors within the independent-quasiparticle approximation, Physical Review B **48**, 11789 (1993).

[200] E. E. Salpeter and H. A. Bethe, A Relativistic Equation for Bound-State Problems, Physical Review **84**, 1232 (1951).

[201] M. Rohlfing and S. G. Louie, Electron-Hole Excitations in Semiconductors and Insulators, Physical Review Letters **81**, 2312 (1998).

[202] G. Onida, L. Reining and A. Rubio, Electronic excitations: density-functional versus many-body Green's-function approaches, Reviews of Modern Physics **74**, 601 (2002).

[203] W. G. Schmidt, S. Glutsch, P. H. Hahn and F. Bechstedt, Efficient $\mathcal{O}(N^2)$ method to solve the Bethe-Salpeter equation, Physical Review B **67**, 085307 (2003).

[204] M. Landmann, E. Rauls and W. G. Schmidt, The electronic structure and optical response of rutile, anatase and brookite TiO2, Journal of Physics: Condensed Matter **24**, 195503 (2012).

[205] M. L. Tiago and J. R. Chelikowsky, First-principles GW-BSE excitations in organic molecules, Solid state communications **136**, 333 (2005).

[206] A. Thatribud, Electronic and optical properties of TiO_2 by first-principle calculation (DFT-GW and BSE), Materials Research Express **6**, 095021 (2019).

[207] J. C. Grossman, M. Rohlfing, L. Mitas, S. G. Louie and M. L. Cohen, High Accuracy Many-Body Calculational Approaches for Excitations in Molecules, Physical Review Letters **86**, 472 (2001).

[208] S. Neufeld, A. Bocchini, U. Gerstmann, A. Schindlmayr and W. G. Schmidt, Potassium titanyl phosphate (KTP) quasiparticle energies and optical response, Journal of Physics: Materials **2**, 045003 (2019).

[209] M. Ghoohestani, S. J. Hashemifar and A. Arab, Linear and nonlinear optical properties of $RbTiOPO_4$–$KTiOPO_4$ alloys studied from first principles, Journal of Applied Physics **128**, 125707 (2020).

[210] A. Bocchini, U. Gerstmann and W. G. Schmidt, Oxygen vacancies in $KTiOPO_4$: Optical absorption from hybrid DFT, Physical Review B **105**, 205118 (2022).

[211] A. Bocchini, S. Neufeld, U. Gerstmann and W. G. Schmidt, Oxygen and potassium vacancies in KTP calculated from first principles, Journal of Physics: Condensed Matter **31**, 385401 (2019).

[212] S. Sanna, T. Frauenheim and U. Gerstmann, Validity of the Slater-Janak transition-state model within the $LDA + U$ approach, Physical Review B **78**, 085201 (2008).

[213] A. Marini, C. Hogan, M. Grüning and D. Varsano, Yambo: An ab initio tool for excited state calculations, Computer Physics Communications **180**, 1392 (2009).

[214] D. Sangalli *et al.*, Many-body perturbation theory calculations using the yambo code, Journal of Physics: Condensed Matter **31**, 325902 (2019).

[215] G. D. Watkins, Negative-U properties for defects in solids, in Advances in Solid State Physics, edited by P. Grosse Vol. 24, Pages 163–189, Springer Berlin Heidelberg, Berlin, Heidelberg, 1984.

[216] J. Jaramillo, G. E. Scuseria and M. Ernzerhof, Local hybrid functionals, The Journal of Chemical Physics **118**, 1068 (2003).

[217] J. Muscat, A. Wander and N. M. Harrison, On the prediction of band gaps from hybrid functional theory, Chemical Physics Letters **342**, 397 (2001).

[218] M. Marsman, J. Paier, A. Stroppa and G. Kresse, Hybrid functionals applied to extended systems, Journal of Physics: Condensed Matter **20**, 064201 (2008).

[219] C. Franchini, V. Bayer, R. Podloucky, J. Paier and G. Kresse, Density functional theory study of MnO by a hybrid functional approach, Physical Review B **72**, 045132 (2005).

[220] A. M. Navarrete-López, M. Rivera-Almazo, J. Garza and R. Vargas, Importance of one-parameter hybrid exchange-correlation functionals in band gaps of transition metal and metalloid oxides, Theoretical Chemistry Accounts **137**, 36 (2018).

[221] A. Janotti, J. B. Varley, P. Rinke, N. Umezawa, G. Kresse and C. G. Van de Walle, Hybrid functional studies of the oxygen vacancy in TiO_2, Physical Review B **81**, 085212 (2010).

[222] H.-P. Komsa, P. Broqvist and A. Pasquarello, Alignment of defect levels and band edges through hybrid functionals: Effect of screening in the exchange term, Physical Review B **81**, 205118 (2010).

[223] P. Deák, M. Lorke, B. Aradi and T. Frauenheim, Optimized hybrid functionals for defect calculations in semiconductors, Journal of Applied Physics **126**, 130901 (2019).

[224] S. Albrecht, L. Reining, R. Del Sole and G. Onida, Ab Initio Calculation of Excitonic Effects in the Optical Spectra of Semiconductors, Physical Review Letters **80**, 4510 (1998).

[225] L. X. Benedict, E. L. Shirley and R. B. Bohn, Optical Absorption of Insulators and the Electron-Hole Interaction: An Ab Initio Calculation, Physical Review Letters **80**, 4514 (1998).

[226] Y. Zhang, H. Wang, C. Ma, Y. Jia, J. Li, J. Wang, R. Boughton and H. Jiang, Growth and optical properties of gray-track-resistant $KTiOPO_4$ single crystals, Journal of Crystal Growth **412**, 67 (2015).

[227] M. Roth, N. Angert, M. Tseitlin and A. Alexandrovski, On the optical quality of KTP crystals for nonlinear optical and electro-optic applications, Optical Materials **16**, 131 (2001), Proceedings of the fourth French–Israeli Workshop: Optical Properties.

[228] A. Deepthy, K. S. R. K. Rao, H. L. Bhat, R. Kumar and K. Asokan, Gray track formation in $KTiOPO_4$ by swift ion irradiation, Journal of Applied Physics **89**, 6560 (2001).

[229] A. R. Albuquerque, A. Bruix, I. M. G. dos Santos, J. R. Sambrano and F. Illas, DFT Study on Ce-Doped Anatase TiO_2: Nature of Ce^{3+} and Ti^{3+} Centers Triggered by Oxygen Vacancy Formation, The Journal of Physical Chemistry C **118**, 9677 (2014).

[230] C. G. Van de Walle and J. Neugebauer, First-principles calculations for defects and impurities: Applications to III-nitrides, Journal of Applied Physics **95**, 3851 (2004).

[231] M. J. Martín, D. Bravo, R. Solé, F. Díaz, F. J. López and C. Zaldo, Thermal reduction of $KTiOPO_4$ single crystals, Journal of Applied Physics **76**, 7510 (1994).

List of Publications

Articles in Scientific Journals

Part of the results discussed in this thesis have already been published.

A. Bocchini, S. Neufeld, U. Gerstmann, and W. G. Schmidt
Oxygen and potassium vacancies in KTP calculated from first principles
Journal of Physics: Condensed Matter **31**, 385401 (2019)

S. Neufeld, A. Bocchini, U. Gerstmann, A. Schindlmayr, and W. G. Schmidt
Potassium titanyl phosphate (KTP) quasiparticle energies and optical response
Journal of Physics: Materials **2**, 045003 (2019)

A. Bocchini, C. Eigner, C. Silberhorn, W. G. Schmidt, and U. Gerstmann
Understanding gray track formation in KTP: Ti^{3+} centers studied from first principles
Physical Review Materials **4**, 124402 (2020)

S. Neufeld, A. Bocchini, and W. G. Schmidt
Potassium titanyl phosphate Z- and Y-cut surfaces from density-functional theory
Physical Review Materials **5**, 064407 (2021)

A. Bocchini, U. Gerstmann, and W. G. Schmidt
Oxygen vacancies in $KTiOPO_4$: Optical absorption from hybrid DFT
Physical Review B **105**, 205118 (2022)

A. Bocchini, U. Gerstmann, T. Bartley, H.-G. Steinrück, G. Henkel, and W. G. Schmidt
Electrochemical performance of $KTiOAsO_4$ (KTA) in potassium-ion batteries from density-functional theory
Physical Review Materials **6**, 105401 (2022)

L. Padberg, V. Quiring, A. Bocchini, M. Santandrea, U. Gerstmann, W. G. Schmidt, C. Silberhorn, and C. Eigner
DC Ionic Conductivity in KTP and Its Isomorphs: Properties, Methods for Suppression, and Its Connection to Gray Tracking
Crystals **12**, 1359 (2022)

S. V. Badalov, A. Bocchini, A. L. Kozub, R. Wilhelm, U. Gerstmann, and W. G. Schmidt,
Rutile, anatase, brookite and titania thin film from Hubbard corrected and hybrid DFT
(submitted)

Other Scientific Publications

M. Krenz, <u>A. Bocchini</u>, T. Biktagirov, A. Kozub, S. Badalov, S. Neufeld, I. A. Ruiz Alvarado, U. Gerstmann, and W. G. Schmidt
Polaron formation dynamics in lithium niobate from massively parallel ab-initio simulations
High Performance Computing in Science and Engineering '22, Springer Nature Switzerland AG (in press)

Conference Contributions

<u>A. Bocchini</u>, S. Neufeld, U. Gerstmann, A. Schindlmayr, and W. G. Schmidt
KTP bulk and surface properties from first-principles calculations
ICFSI17, Shanghai 2019 (poster)

<u>A. Bocchini</u>, U. Gerstmann, and W. G. Schmidt
Ti^{3+} centers in KTP studied from first principles
MAX/CECAM "Virtual school on electronic excitations in solids and nanostructures using the Yambo code", online 2021 (poster)

<u>A. Bocchini</u>, U. Gerstmann, and W. G. Schmidt
Oxygen vacancies in KTP: Optical absorption from hybrid DFT
WPO22, Goslar 2022 (poster)

<u>A. Bocchini</u>, U. Gerstmann, T. Bartley, H.-G. Steinrück, G. Henkel, and W. G. Schmidt
Electrochemical performance of $KTiOAsO_4$ (KTA) in potassium-ion batteries from density-functional theory
DPG Spring Meeting, Dresden 2023 (poster)

Danksagung

Nun bin ich auch schon am Ende angelangt und voller Erleichterung schreibe ich die letzten Zeilen dieser Dissertation. Diese möchte ich all denjenigen widmen, die mich in den letzten Jahren beiseite standen.

An erster Stelle möchte ich hier Prof. Dr. Wolf Gero Schmidt, nennen. Vielen Dank, dass Du seit der Bachelorarbeit vertrauen in meine Fähigkeiten hattest und mich auf meinen akademische Werdegang bis hin zur Promotion mit Expertise, Unterstützung, und Motivation begleitet hast. Nicht weniger sei an dieser Stelle Prof. Dr. Uwe Gerstmann gedankt. Auch Dir vielen Dank für die interessanten Diskussionen, die Zeit die Du in mich investiert hast, und die wertvollen Tipps und Anregungen, welche mir dabei geholfen haben, meine Forschungsergebnisse deutlich zu verbessern.

Auch möchte ich mich bei meiner Promotionskommission bedanken.

Ein großes Dankeschön gilt auch all denen, die ich durch meine Zeit auf N3 kennenlernen durfte. Hier möchte ich vor allem meine Bürokollegen Yannick Freitag und Marvin Krenz für das angenehme Arbeitsklima, sowie Dr. Christian Braun und Maximilian Kulke für die lustigen Gespräche während der Mittagspausen danken. Und natürlich soll hier Simone Lange nicht vergessen werden. Danke einfach für Alles und nicht zuletzt für deine Herzlichkeit.

Mein Dank gilt auch Dr. Christof Eigner, für die hilfreichen Diskussionen übers *Gray Tracking* und fürs Korrekturlesen.

Außerdem möchte ich mich auch bei meinen Kommilitonen aus den Physikstudium, meiner, Familie und Freunden bedanken. Ein großes Danke geht vor allem an dich, Tanja, dass du immer ein offenes Ohr und ein liebes Wort für mich hattest.

Auch danke ich meiner Mutter Daniela und meinem Vater Vincenzino, der leider viele wichtige Momente nicht miterleben durfte, für ihre Unterstützung und dafür mir ermöglicht haben den Weg des Physikstudiums einzuschlagen.

Und nun fehlt nur noch eine Person, die mir immer zur Seite stand und mich in den letzten Monaten des Schreibens mit Humor aus so manchem Motivationsloch geholt hat, mein Freund Sergej. Danke dafür, dass du einfach du bist und ich bei dir einfach ich sein darf.